

AMERICAN UNIVERSITY OF BEIRUT

MEASUREMENT OF PHONON
ANHARMONICITY IN ZINC OXIDE USING
TEMPERATURE DEPENDENT RAMAN
SPECTROSCOPY

by

IBRAHIM HAMZAH NOUR AL DEEN

A thesis
submitted in partial fulfillment of the requirements
for the degree of Master of Physics
to the Department of Physics
of the Faculty of Arts and Sciences
at the American University of Beirut

Beirut, Lebanon
January 2021

AMERICAN UNIVERSITY OF BEIRUT

MEASUREMENT OF PHONON
ANHARMONICITY IN ZINC OXIDE USING
TEMPERATURE DEPENDENT RAMAN
SPECTROSCOPY

by

IBRAHIM HAMZAH NOUR AL DEEN

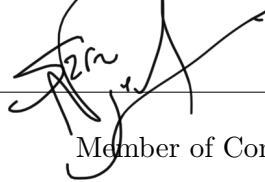
Approved by:



Dr. Michel Kazan, Associate Professor

Advisor

Physics



Dr. Sara Najem, Assistant Professor

Member of Committee

Physics



Dr. Digambara Patra, Professor

Member of Committee

Chemistry

Date of thesis defense: January 28, 2021

AMERICAN UNIVERSITY OF BEIRUT

THESIS, DISSERTATION, PROJECT RELEASE FORM

Student Name: Nour aldeen Ibrahim Hamzah
Last First Middle

Master's Thesis Master's Project Doctoral Dissertation

I authorize the American University of Beirut to: (a) reproduce hard or electronic copies of my thesis, dissertation, or project; (b) include such copies in the archives and digital repositories of the University; and (c) make freely available such copies to third parties for research or educational purposes.

I authorize the American University of Beirut, to: (a) reproduce hard or electronic copies of it; (b) include such copies in the archives and digital repositories of the University; and (c) make freely available such copies to third parties for research or educational purposes after: **One year from the date of submission of my thesis, dissertation or project.**
Two ___ years from the date of submission of my thesis , dissertation or project.
Three ___ years from the date of submission of my thesis , dissertation or project.


Signature

07/02/2021
Date

This form is signed when submitting the thesis, dissertation, or project to the University Libraries

Acknowledgements

This work was done under the supervision of Prof. Kazan. My regards to him does not concern only his academic work with me, but also for him being gentle, generous with his ideas and contributions, and helpful with me alongside being my supervisor. I would like to thank him also for his open door, that is the safe spot for his students whenever we are in trouble.

Besides my advisor, I would like to thank my thesis committee: Prof. Patra Digambara and Dr. Sara Najem for their encouragement and support in terms of communication and availability.

This work was not only about academic support. From here I would like to thank my friends for standing by me during the time of this work. To start with my friend, *Hasan Taki*, and recently graduated to be a Doctor; *Sobhi Hamieh*, not forgetting *Marwa Dakik* my friend from the previous university, which means that we had alot of tough times together, also thanks for *Carmen Al Masri*, *Ashod Khederalian*, *Kafa Alameh* and *Ghina Al Atat* for the fun times in the graduate room. A final thanks to *Zainab Hrajli* for being a good friend and for helping me in the CORE lab, and *Riham* for preparing the samples.

Most importantly, none of this could have happened without my family. I want to thank my mother and father for their guidance and endless love, and my sisters for their encouragement. Finally I mention the person I consider my brother *Mohamamd Nader* for giving me the hope and being always by my side.

An Abstract of the Thesis of

IBRAHIM HAMZAH NOUR AL DEEN for Master of Physics
Major: Physics

Title: Measurement of Phonon Anharmonicity in Zinc Oxide Using Temperature-Dependent Raman Spectroscopy

The aim of this thesis is to use temperature-dependent Raman spectroscopy to study the effect of defects on the anharmonicity of optical phonons in Wurtzite zinc oxide (ZnO) nanoparticles, which is unexplained by existing theories.

Due to its high piezoelectric properties and exciton binding energy, wurtzite zinc oxide (ZnO) has long been regarded as a material of choice for piezoelectric transducers and ultraviolet emitters at 300 K. Nevertheless, native defects in ZnO often lead to undesirable defect levels in the electronic bandgap and phonon bands, which hinder the commercial applications of ZnO. Therefore, the origin of the native defects in ZnO has been the subject of much discussion, and many conclusions about their nature and physical properties have been drawn. Nevertheless, the effect of defects on phonon dynamics, which have a crucial role in determining the efficiency of piezoelectricity and even the emission of the material, is not yet understood. In this thesis, we tackle this issue by using temperature-dependent Raman spectroscopy. Room temperature measurements are used to determine first-order and second-order Raman modes. Temperature-dependent Raman spectroscopy carried out on heated and cooled samples are used to investigate the anharmonicity of optical phonon of the center of the Brillouin zone. Raman line-shape measured in the temperature range 300-1000 K is fitted to a theoretical model derived on the basis of perturbation theory to retrieve the two-phonon density of states. The results show that upon heating, the defect complexes change their configuration in an irreversible process, resulting in a strong effect on the two-phonon density of states.

Contents

Acknowledgements	v
Abstract	vi
1 Introduction	1
2 Literature Review	4
2.1 ZnO Nanoparticles Study	4
2.1.1 Introduction to Nano-technology	4
2.1.2 ZnO Structure	5
2.1.3 Synthesis Methods of ZnO NanoParticles	6
2.1.4 Applications Of ZnO Nanoparticles	10
2.2 Raman Spectroscopy	12
2.2.1 The Basics	12
2.2.2 Theoretical Basis	14
2.2.3 Building The Raman System: Lasers	16
2.2.4 Raman Sensitivity to Polarization	17
2.2.5 Raman Instrumentation	18
2.2.6 Raman Opto-thermal Technique	19
2.2.7 Raman Study of ZnO Crystal	20
2.2.8 First-Order Raman Spectrum of ZnO	21
2.2.9 Second Order Raman Spectrum of ZnO	23
2.3 Anharmonicity	28
2.3.1 Introduction	28
2.3.2 Model of Vibrational Diatomic Lattice	28
2.3.3 Hamiltonian Of 3d Crystal	31
2.3.4 Effects Of Anharmonicity On Phonon States	38
2.3.5 Anharmonicity effects on Phonon Self Energy, Responsible For The Frequency and Lifetime Change	41
2.3.6 Fermi Golden Rule of Three and Four Phonon Processes	44
2.3.7 Thermal Expansion Effect	47
2.3.8 Life-time of Optical Phonons	48
2.3.9 Temperature Dependence of The E_2^{high} Mode	53

2.3.10	Temperature Dependence of $A_1(LO)$ and $E_1(LO)$ Modes Using The Ridley channel model	54
2.4	Phonon Confinement Model In Raman Spectroscopy For Nano- Materials	55
3	Results and Discussion	66
3.1	Experiment	66
3.2	First Order Raman Spectrum	67
3.3	Second order Raman Spectrum	69
3.4	Asymmetry of E_2^{high} Mode	73
3.5	Temperature dependence of the E_2^{high} mode	76
3.6	Temperature dependence of the A_1 mode at $333cm^{-1}$ and $E_1(LO)$ mode at $582cm^{-1}$	81
3.7	Conclusion	83
A	Abbreviations	85

List of Figures

2.1	The Wurtzite-structure of ZnO. The big white spheres are Oxygen atoms, and the small brown spheres are Zn atoms	6
2.2	TEM micrographs of ZnO nano-structures. (a) ZnO nanorods grown under standard conditions. (b) The result of slow oxidation process (2 weeks) in THF which gave ZnO nanodisks.(c) Standard condition reaction, but with using DDA instead of HDA, also for ZnO nanodisks.(d) Standard condition reaction by using OA instead of HDA.[1]	8
2.3	XRD measurements of ZnO nano-structures. (a) Triangles, (b) Spherical nanoparticles, (c) Nanorods. [2]	9
2.4	SEM micrographs of ZnO nanoparticles, synthesized by solvothermal process. (a) 1,3-propanediol, (b) 1,4-butanediol, (c) 1,5-pentanediol, and (d) 1,6-hexanediol.[3]	9
2.5	The first image is the high-resolution transmission electron microscopy (HRTEM) image of the ZnO polymer core-shell nanoparticles. The second image is the aqueous solution of ZnO-1 and ZnO-2 under UV light. the middle part is the DIC picture and the fluorescent image of the human hepatoma cells labeled by ZnO-1; and the lower part is the DIC picture and the fluorescent image of the hepatoma cells labeled by ZnO-2. Copyright 2008 American Chemical Society.	11
2.6	Vibrational States of Molecule Excitation	13
2.7	Fluorescence	14
2.8	(a) Energy level diagram for Raman scattering and fluorescence emission; (b) temporal variation of excitation, Raman scattering and fluorescence emission.	16
2.9	Raman Instrumentation	18
2.10	First order Raman study of the $A_1 + E_2 + E_1$ scattering geometries at room temperature.	23
2.11	First and second order Raman spectra of ZnO and their symmetries, compared to ref [4], the symmetries in parenthesis represents lower intensities of the dominant symmetry configuration.	24
2.12	Temperature dependence of second order Raman peaks in ZnO.	25

2.13	Second order peak of ZnO obtained for different scattering geometries. From bottom to top, $x(z y)\bar{x}$, $z(x y)\bar{z}$, $x(z z)\bar{x}$, and $z(x x)\bar{z}$.	26
2.14	Intensity of the second order peak at 33cm^{-1} normalized to its value at room temperature. The dashed line represents the calculation for the difference mode $E_2^{high} - E_2^{low}$, while the dotted line is for TA overtones around point M	27
2.15	Diatomic Linear Chain	29
2.16	Dispersion Curve	30
2.17	(a) N-Process (b) U-process.[5]	41
2.18	Temperature dependence of the linewidth (squares), left axis and frequency (triangles), right axis of the E2 high mode. The dashed line is a fit of the model discussed in the text to the linewidth data. The dot-dashed line corresponds to the temperature dependence of the frequency given by the model for the same set of parameters.	54
2.19	Relation between the frequency shift and line-width in Raman line	57
2.20	Measured and calculated Raman line for $\mu\text{c-Si}$ sample. The solid line is calculated Raman intensity, while the dotted line is for measured intensity	58
2.21	Raman line-width versus temperature of 3 $\mu\text{c-Si}$ samples and 1 c-Si sample. The solid lines are the fitted results	59
2.22	The obtained line-width from fitting the temperature dependence line-width of 4 Si samples	59
2.23	The calculated frequency shift and broadening for the micro-crystal structures using I. exponential II. Sinc III. Gaussian. The dots are from the work of Iqbal <i>et al</i> , the (X) are from the work of Richter <i>et al</i> , and the hollow rhombus is from the authors' work	62
2.24	The three micro-crystals shapes. Length L_2 of the column is considered to be infinite.	63
2.25	This graph displays the relation between the calculated frequency shift, broadening and crystal size of the three various shapes: I.Sphere II. Column III. Thin film. The experimental points are the same as figure (2.23) with the addition from the measurements of Murphy <i>et al</i> . displayed by hollow circles.	64
2.26	Experimental and theoretical spectra of 40 Angstroms thin film.	64
3.1	Raman Spectrum of E_2^{high} mode	67
3.2	Raman Spectrum of $E_1(TO)$ mode	68
3.3	Raman Spectrum of $A_1(TO)$ mode	68
3.4	Raman Spectrum of $A_1(LO)$ and $E_1(LO)$ modes	69
3.5	Raman Spectrum of 1060,1102 and 1160 cm^{-1} peaks	70
3.6	Raman Spectrum of 333cm^{-1}	71
3.7	Raman Spectrum of 197cm^{-1} and 277cm^{-1} modes	71
3.8	Raman Spectrum of $654,666\text{cm}^{-1}$	72

3.9	Thermal expansion coefficients along parallel (black squares) and perpendicular (red circles) directions of the lattice axis.	74
3.10	Two phonon sum DOS	75
3.11	The spectrum of E_2^{high} mode of ZnO at room temperature. The noisy black line represents our experimental results, where the solid red line is calculated using equation 3.6.	76
3.12	This figure shows the spectrum of E_2^{high} mode of ZnO at various temperatures. The left side shows the heating process, while the right side illustrates the cooling process. On both sides, the noisy lines with different colors represent our measurement of the Raman spectra of the E_2^{high} mode at different temperatures. The solid black lines are the fitted theoretical lines from the fitting intensity equation (3.6) concluded from the model mentioned above. The dashed line follows the position of the defect (dip-like shape) as temperature increases, also the arrow points at another doublet defect at the heating process, before its transformation to a singlet during the cooling process	77
3.13	The first figure shows the strength of the third anharmonic coefficient of the phonon sum as a function of temperature during the heating and the cooling process. While in its inset, we see the graph of the two phonon sum DOS as function to the wavenumber. The second figure shows the $ V_3^- ^2$ as a function of temperature. In both figures, the red circles are associated to the heating process, while the blue circles demonstrates the cooling process.	80
3.14	The first figure shows the temperature dependence of the line-width of the A_1 symmetry mode at $333cm^{-1}$, while the second figure shows the temperature dependence of the $E_1(LO)$ mode at $586cm^{-1}$. For both graphs, the red circles are the values of the width during the heating process, while the blue circles are the values of the width during the cooling process. The black solid line represents the fitted line from the theoretical equation (3.8) .	82

List of Tables

2.1 Raman Active Modes	21
3.1 Second order Raman peaks, and their associated symmetry and position in the Brillouin zone.	72

Chapter 1

Introduction

Materials with special thermal properties are now a priority for scientists and physicists developing a new generation of optoelectronic devices. As some properties of materials are temperature-dependent, a clear and wide study should be done on the temperature-induced changes of the material. In order to understand heat transport in random materials, we should build our knowledge on the heat carriers. In our material, the heat carriers are the phonons. It is known that temperature is considered as a perturbation on the harmonic part of the lattice potential, and this temperature changes the population of the various levels for each specific mode, motivating the change of the lattice parameters. To note here, any change of a lattice parameter with temperature is referred to anharmonic parts of the lattice potential. These anharmonic parts in the lattice potential appear after expanding the potential in a Taylor series of displacement, and become more active and alter the harmonic part when the temperature is present. The anharmonic parts in the potential are embodied by phonon interactions, as the picture of non-interacting phonons breaks down. Thus, non-equilibrium phonon populations decay into lower energies, or combine and go to higher energy, inducing energy shifts in the vibrational modes.

As an effect of the above-mentioned interactions, the phonons' energy get shifted from their original values; which is a shift in the frequency, and their lifetime become shorter. Mainly, there are two ways to measure the frequency shift and the change of the life-time of phonons. This can be done by Raman scattering, or by inelastic neutron scattering. Inelastic neutron scattering happens when an emitted neutron interacts with an atom, and as a consequence it exchanges energy, so it can emit or absorb energy equal to $\hbar\nu$ which is the quantum of phonon energy. In INS the neutron has different wave vectors before and after the interaction, so a technique must be used to determine its wave vector, this technique is called "Three Axis Spectrometer" which is considered as the mother of all crystal spectrometers. This was a brief explanation about INS. For our measurement, the technique we use to determine the various vibrational modes in a lattice is "Raman Spectroscopy". This method works when light is emitted

on the sample, so it interacts with the atoms at their lattice sites, and upon this interaction they exchange energy with the quantum of vibrational modes; the phonons. The reflected photons are gathered and displayed using the appropriate tools, so we can gather information related to phonons.

As there is no clear and adequate theory describing anharmonicity and its effects, first-principle methods and equations were applied to justify some of the obtained results. The expressions for the frequency and width as a function of temperature are based on the anharmonic contribution from the Hamiltonian:

$$\begin{aligned}
H_A = & \sum_{\vec{q}_1, \vec{q}_2, \vec{q}_3} \sum_{j_1, j_2, j_3} V \begin{pmatrix} \vec{q}_1 & \vec{q}_2 & \vec{q}_3 \\ j_1 & j_2 & j_3 \end{pmatrix} A(\vec{q}_1, j_1) A(\vec{q}_2, j_2) A(\vec{q}_3, j_3) \\
& + \sum_{\vec{q}_1, \vec{q}_2, \vec{q}_3, \vec{q}_4} \sum_{j_1, j_2, j_3, j_4} V \begin{pmatrix} \vec{q}_1 & \vec{q}_2 & \vec{q}_3 & \vec{q}_4 \\ j_1 & j_2 & j_3 & j_4 \end{pmatrix} A(\vec{q}_1, j_1) A(\vec{q}_2, j_2) A(\vec{q}_3, j_3) A(\vec{q}_4, j_4)
\end{aligned} \tag{1.1}$$

With $A(\vec{q}, j) = a_{\vec{q}, j} + a_{-\vec{q}, j}^\dagger$ representing the phonon creation and annihilation operators. The effect of the above Hamiltonian is to change the harmonic frequency, $w(0, j)$ to a damped one $w(0, j; \omega)$ as follows:

$$w^2(\vec{0}, j; \omega) = w^2(\vec{0}, j) + 2w(\vec{0}, j)[\Delta(\vec{0}, j; \omega) + i\Gamma(\vec{0}, j; \omega)] \tag{1.2}$$

The term in the brackets is the phonon self energy consisting of real and imaginary parts. The real part stands for the shift in the peak position, which is the frequency change, while the imaginary part describes the line-width change.

For material to maintain thermal equilibrium, one should explore the distribution of optical modes energies, and their associate decay channels alongside with the decay processes. Raman spectroscopy is used to follow the temperature dependent Raman shift and line-width of ZnO nanoparticles, and therefore enable us to gather more info about the behaviour of the associated optical modes and their decay processes. In his paper, Cowley [6] discussed the frequency shift and lifetime change by perturbation theory. In this dilemma, the effect of cubic anharmonicity was calculated to the second order in perturbation theory, and the quartic anharmonicity to first order. This helps us obtain the frequency shift (real part of the phonon self energy), and the life-time change (imaginary part of the phonon self energy). The effect of cubic anharmonicity on the phonon self energy is as follows:

$$\begin{aligned}
\Delta(qj, \Omega) = & \frac{-18}{\hbar^2} \sum_{q_1 q_2 j_1 j_2} \left| V \begin{pmatrix} q & q_1 & q_2 \\ j & j_1 & j_2 \end{pmatrix} \right|^2 \left[\frac{n_1 + n_2 + 1}{(w_1 + w_2 + \Omega)_p} + \right. \\
& \left. \frac{n_1 + n_2 + 1}{(w_1 + w_2 - \Omega)_p} + \frac{n_2 - n_1}{(w_1 - w_2 + \Omega)_p} + \frac{n_2 - n_1}{(w_1 - w_2 - \Omega)_p} \right] \\
& + \frac{12}{\hbar} \sum_{q_1 j_1} V \begin{pmatrix} q & -q & q_1 & -q_1 \\ j & j & j_1 & j_1 \end{pmatrix} (2n_1 + 1)
\end{aligned} \tag{1.3}$$

$$\Gamma(qj, \Omega) = \frac{18\pi}{\hbar^2} \sum_{q_1 q_2 j_1 j_2} \left| V \begin{pmatrix} q & q_1 & q_2 \\ j & j_1 & j_2 \end{pmatrix} \right|^2 (n_1 + n_2 + 1) [\delta(w_1 + w_2 - \Omega) - \delta(w_1 + w_2 + \Omega)] \\ + (n_2 - n_1) [\delta(w_1 - w_2 - \Omega) - \delta(w_1 - w_2 + \Omega)] \quad (1.4)$$

In our work, we intend to study the temperature induced changes on the optical phonon modes of Zinc Oxide nano-particles, so we can fit the results and analyse the anharmonic effects which are the phonon modes' response to temperature, and phonon-phonon interactions happening at elevated temperatures, and the study cooling process of the target material.

Chapter 2

Literature Review

The objective of this literature survey is to give a general overview of some important concepts related to the thesis work. We start by giving an overview about ZnO nano-particles, Raman spectroscopy, phonons as the quantum of the vibrations in a lattice, origin of anharmonic parts and their effect on the material and summary of some work done in this field.

2.1 ZnO Nanoparticles Study

2.1.1 Introduction to Nano-technology

The word "Nano-Technology" has emerged widely in social life, to the stage that nearly everyone; either concerned in the topic or not, have heard of it. It was stated by the physicist Richard Feynmann in 1959, in a meeting held up at California Institute of Technology, when he was delivering a talk entitled "There is Plenty of Room in The Bottom", that was directed to the American Physical Society [7]. In his lecture, he discussed the chances of achieving nano-sized products formed by atoms as building particles. Years passed and no one approached the concept given by Feynmann. Until 1974, when the nomenclature "Nano-Technology." first appeared by Norio Taniguchi, a professor in Tokyo University of Science, who talked about this concept in the "International Conference on Production Engineering "[8]. He was the inventor of the "top-down." approach, which deals with sequential slicing of bulk material, for the aim of deforming it to get nano-sized particles. After that, Kim Eric Drexler, who is an American engineer, came with the 'bottom-up' approach, a technique for building nanostructures, which is creating material at the level of atoms 'atom-by-atom', then molecule by molecule. He represented his ideas and developments for nano-technology techniques in his book: Engines of Creation: The Coming Era of Nano-Technology." Nowadays, the standard production approaches for nano-particles are achieved through the "top-down." and "bottom-up." pro-

cesses introduced by Prof. Norio Taniguchi and Eric Kim Draxler, respectively. Materials consisting of nanoparticles are highly reactive with eminent physical properties, this feature is attributed to the increased high surface/volume rate caused by the formation of nanoparticles, which allows massive number of the consisting atoms to be on the surface of the nanoparticle, thus the material being more effective. Some specific materials consisting of nanoparticles tend to show outstanding physical properties. Therefore a clear and artificial way for creating this nanoparticles is needed. One of the critical issues in nanoparticles' growth is following the various numbers of techniques for the synthesis of these nanoparticles to acquire it to have a uniform shape and size. Seeking simple methods of synthesising is one important issue to be investigated in nanoparticle growth. From the time when "Nano-Technology" first appeared, scientists, engineers and physicists were included in the research of finding the best routes in achieving the required nanoparticle shape and size. This synthesis is possible through 3 states of matter: Solid, gaseous media, and liquid (chemical method) [9, 10]. The favourable method of synthesis is the chemical method because it is of low-cost, more reliable, and it leads us to good matches of the required nanoparticle morphology. One concludes that, nanoparticles with high surface-to-volume ratio is of high demand, but the accumulation of the residual small particles in solution must be taken into account where there is no stabilizers. Regarding this issue, the presence of stable colloids can help in stabilizing the solution. Furthermore, the electric repulsion method is generally used in settling down nano-particles due to the presence of polymer molecular, or any other organic stuff that is attached to the surface of the particles. After listing some of the major advantages of nanoparticles, we can specify types of nanoparticles, which can be created in the following form. In the synthesis process, one can create polymer, metal, and metal-oxide nanoparticles. Among the metal-oxide type, Zinc Oxide is of our interest.

2.1.2 ZnO Structure

ZnO is a Wurtzite-type crystal; which is a crystal of hexagonal shape, and it belongs to C_{6v}^4 space group with two formula units in the primitive cell. The unit cell of Wurtzite ZnO has a hexagonal shape, with two lattice parameters, a and c . In figure (2.1) [11], we see the structure of ZnO. The two interpenetrating hexagonal closed packed sublattices are the main components of this structure. Each sublattice is formed of unique type of atom, either Zinc or Oxygen atoms, and the sublattices are displaced along the three fold c -axis.

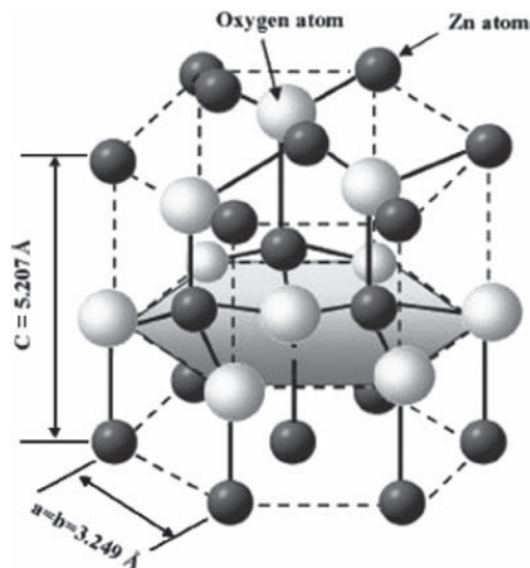


Figure 2.1: The Wurtzite-structure of ZnO. The big white spheres are Oxygen atoms, and the small brown spheres are Zn atoms

2.1.3 Synthesis Methods of ZnO NanoParticles

Now it is agreed among engineers, scientists, chemists and physicists that ZnO nano-structures has wide contributions to many applications. One thinks of the ways of updating and adjusting the synthesis processes of these nano-structures to gain control of the various shapes and sizes required to be obtained, including: Nanorods, nanowires, nanoparticles, and nanotubes [12, 13]...Our focus will be on the synthesis of ZnO nanoparticles by two different methods:

1. Sol-gel Method. (Solution Method)
2. Hydrothermal Method.

As we research about nano-particle synthesis, we find that in many papers the solution method is adopted to be the main procedure in cooking ZnO nano-particles. This is because of its low cost, and it is eco-friendly. As I mentioned before, one of the most important demands in the process is to achieve the required shape and size. The paper published by Monge *et al.*, reports the organometallic synthesis of ZnO nanoparticles at ambient temperature using the first procedure listed above. The basis of this procedure is the disintegration of the organometallic precursor into oxidized materials in the air. It is found in a report [14], that the formation of ZnO nanoparticles with a random shape and size is done by keeping the compound solution $[Zn(c - C_6H_{11})_2]$, named dicyclohexylzinc(II), in tetrahydrofuron (THF), at room temperature in the open air. This formation of ZnO

is a repercussion of the evaporation of the solvent that leaves white residues at the bottom, that is found to be agglomerated ZnO nanoparticles after checking it using X-ray diffraction (XRD). This led Monge *et al.* to utilize a new experimental condition to get well defined ZnO nanoparticles in shape and size, this was done using hexadecylamine (HDA) under Argon atmosphere, and it showed good results. From the study, it is found that the shape and size of the nanoparticles are affected directly by several conditions. These conditions play a role in defining the shape and growth rate of ZnO nanoparticles, and we found the most prevailing conditions to be: The relative and the total concentration of the ligand, the time taken of the evaporation process and its relative temperature, the reaction time, the solvent, and the reaction temperature. Add to that the open dry air effect on the reaction. When the reaction is done in the mentioned medium, the nanoparticles are created with no specific shape and size. More detailed results are available in figure (2.2). In figure (2.2(b)), we can see the formation of homogeneous nanodisks of average size equal to 4.1 nm, this is a result of slow evaporation in (THF), otherwise if we replace THF by toluene or heptane we get isotropic shapes with average size of 2.4 for heptane and 2.6 for toluene. Figure (2.2(c,d)) shows the results of substituting HDA with dodecylamine (c) or octylamine (d), the outcomes are nanodisks of mean diameters of 3 nm and 4 nm respectively.

After this work, the studies by Kahn *et al.* [15] shed the light on the importance of the solvent in deciding the shape of ZnO nano-structures. Furthermore, Andelman [2] specified the dependence of the solvent type on the nano-structure's shape. He used three different types of solvents and obtained three different shapes. The spherical nanoparticles shape is obtained by using 1-octadecene (OA), whereas nanorods is a result of using trioctylamine (TOA), and the third solvent which is 1-hexadecanol (HD) resulted in nanotriangles. The nanoparticles' size ranged from 12-14 nm.

Extending the work on the formation of ZnO nano-structures, Ayudhya *et al.* [3] showed more effects of the solvent on ZnO products. The study introduces four types of organic solvents :

1. Alcohols
2. Glycols
3. Alkanes
4. Aromatic

The synthesis relies on suspending the Zinc acetate in these different types of solvents and then cooking them in an autoclave in a range of $250 - 300C^{\circ}$. This is a solvent dependent method. One concern in the formation of ZnO nanoparticles emerges from the possibility of the decomposition of the Zinc acetate precursor to form Zinc nuclei. This assumption has been taken into account by studying the stability of Zinc acetate through its interaction with the solvent [16, 17]. One important note to be mentioned here is the dependence of the shape of ZnO

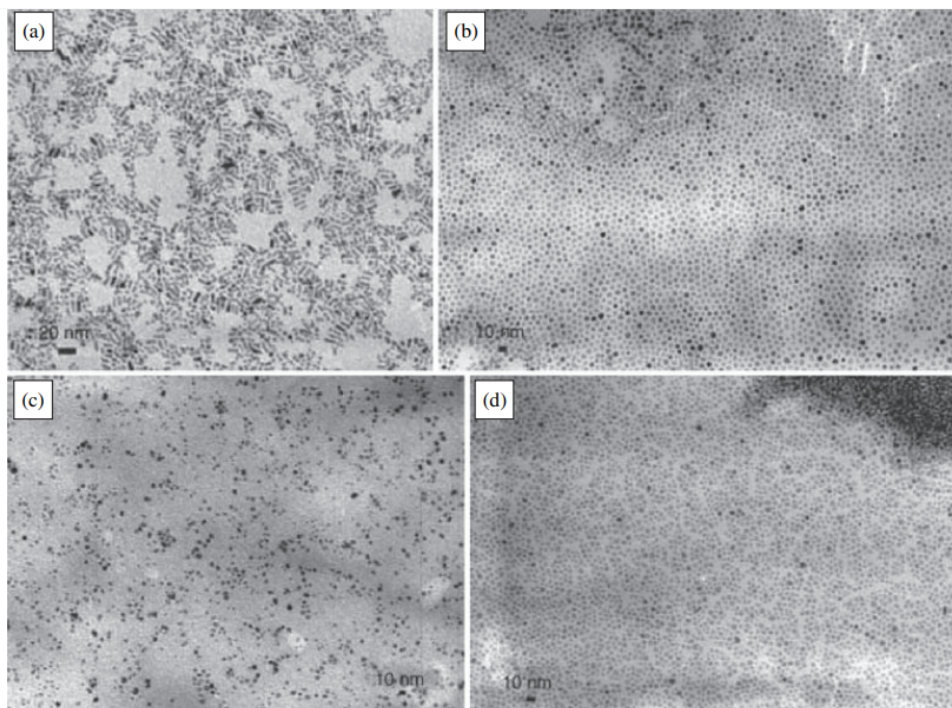


Figure 2.2: TEM micrographs of ZnO nano-structures. (a) ZnO nanorods grown under standard conditions. (b) The result of slow oxidation process (2 weeks) in THF which gave ZnO nanodisks.(c) Standard condition reaction, but with using DDA instead of HDA, also for ZnO nanodisks.(d) Standard condition reaction by using OA instead of HDA.[1]

nano-objects on the length of the alcohol molecules' chain, with this feature is not present for the other 3 solvents. The dielectric constant emerges into the picture of synthesis, it is required by solvents having low-dielectric constants to be cooked at high temperature, which is the case of *n*-alkanes and aromatics compounds, whereas low temperature (250°) is required for high dielectric constant compounds as glycols and alcohols. The retard and delay of the growth of the crystal is attributed to the adsorption of the negatively charged molecules over the the positive ones represented by Zn, this process happens at the facet (0001) of the crystal. A similar process occurs upon using glycols as solvent which lead to the formation of ZnO nanoparticles instead of ZnO nanorods. See figure (2.4). Also the use of long chain alcohols as solvents has given good quality of ZnO nanoparticles in size and shape, this is a direct consequence of the unpolarized nature of alcohols used. This experiment gave much credit to the value of the dielectric constant of the used solvent on deciding the morphology of ZnO nanoparticles, but this is not enough, as more experiments are needed to be more specific about the characterizations of the wanted nanoparticles. One of these needed experiments is done by Kawano *et al.* [18], its study area was to discover

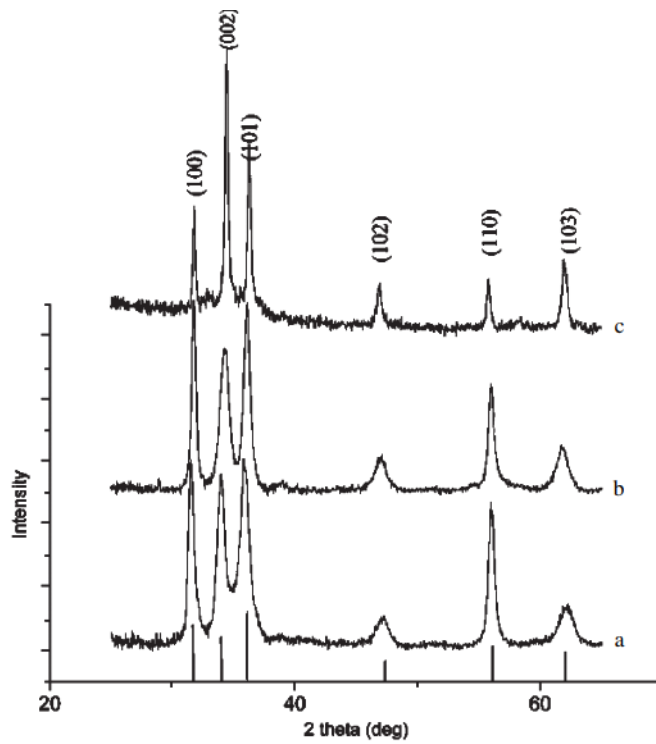


Figure 2.3: XRD measurements of ZnO nano-structures. (a) Triangles, (b) Spherical nanoparticles, (c) Nanorods. [2]

the effects of using basic and acidic solutions on the morphology of ZnO.

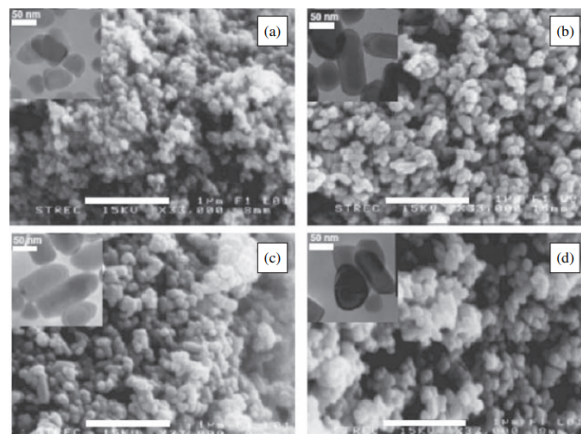


Figure 2.4: SEM micrographs of ZnO nanoparticles, synthesized by solvothermal process in (a) 1,3-propanediol, (b) 1,4-butanediol, (c) 1,5-pentanediol, and (d) 1,6-hexanediol. [3]

2.1.4 Applications Of ZnO Nanoparticles

In general, nanoparticles have massive contributions to biomedical applications. They possess unique physicochemical characteristics where this feature is coming from their high surface-to-volume ratio, which gives them the upper hand against bulk materials. The use of the name nanomedicine is attributed to the utility of various materials of nanoparticles in curative and diagnostic strategies. This comes from the advantage of their low scale dimensions; about ($10^{-9}m$), so this increases the possibility of them to interact with the cell membrane, nucleic acids and proteins, that are of the same size. Scientists took charge of developing and creating material nanoparticles, like Au NPs (gold nanoparticles), silver and platinum nanoparticles. Also, they managed to synthesize metal-oxide nanoparticles as (ZnO, TiO_2 , and CuO), never to forget the quantum dots and lanthanide nanoparticles. Among these materials; and many others, ZnO nanoparticles are the most used ones for their various biomedical applications. As it is obvious in this chapter, we intend to focus on the use of ZnO nanoparticles in versatile medicinal applications. The branches of medicinal applications are wide, ZnO can contribute to wound healing, anticancer activity, drug delivery, bioimaging, and antimicrobial activity [19].

Anti-Cancer Drug Delivery

One important advantage of using nano-particles in drug delivery is to reduce the overall amount of drugs, thus minimizing size effects. ZnO nano-particles are favorable to this mission due to their low toxicity and biodegradable characteristics. In this anti-cancer treatment, various types of drugs such as paclitaxel, curcumin and doxorubicin are loaded onto Zinc Oxide nano particles to enhance the solubility, toxicity and effective delivery to cancer cells.

Anti-Bacterial Activity

As mentioned before, ZnO nano-particles has high specific surface area, and they are active to prevent large amount of pathogenic agents. Their antibacterial activity causes death to the bacterial cells, this is because of the ability of ZnO nano-particles to accumulate in the outer membrane or cytoplasm of the targeted cells, and by triggering large amount of Zn^{+} that affects the bacterial cell[20]. Tests are done on Gram-negative Escherichia coli and Gram-positive Staphylococcus; which are bacteria, to assess the effect of ZnO on the bacterial cells.

ZnO Used In Bio-Imaging

ZnO nano-particles contribution to bio-imaging field comes from oxygen vacancies. This vacancies causes the nano-particle to have green or yellow luminescence

and efficient blue emission. Xiong *et al.* prepared ZnO polymer core-shell nanoparticles for the first time. The feature of his new invention is the high quantum yield and very stable broad photoluminescence of the ZnO nano-particles in aqueous solutions [20]. The ZnO-1 has size of 3nm, green luminescence and is derived

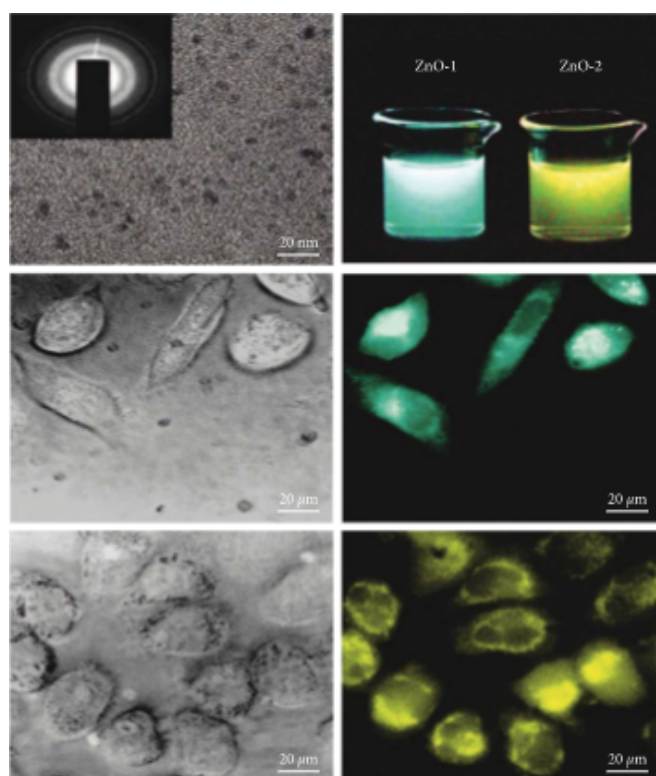


Figure 2.5: The first image is the high-resolution transmission electron microscopy (HRTEM) image of the ZnO polymer core-shell nanoparticles. The second image is the aqueous solution of ZnO-1 and ZnO-2 under UV light. The middle part is the DIC picture and the fluorescent image of the human hepatoma cells labeled by ZnO-1; and the lower part is the DIC picture and the fluorescent image of the hepatoma cells labeled by ZnO-2. Copyright 2008 American Chemical Society.

from LiOH. While ZnO-2 is of 4nm, has yellow luminescence and is derived from NaOH. What is important to mention here, is that these two ZnO polymers did not cause any damage to human hepatoma cells when their concentrations were less than 0.2mg/mL . The cell kept functioning around 45 minutes with very stable luminescence. From here we can say that ZnO polymer has presented itself as a cheap and safe luminescent label, also they can be used as fluorescent probes for cell imaging in vitro [21].

2.2 Raman Spectroscopy

2.2.1 The Basics

The technique is named after the Indian physicist Chandrashekhara Venkata Raman, the man who started his work concerning light scattering back in 1922 when he published his paper "Molecular Diffraction of Light". After some serious work by him and his collaborators, and in 1928, he discovered the inelastic scattering of light with matter and its effects, leading him to win the Nobel Prize in Physics in 1930.

One of its features is to determine the vibrational modes of materials, that are illuminated by a laser beam of some power [22]. The laser beam which is an electromagnetic radiation strikes in a molecule, and interacts with the electrons distributed on the electronic clouds outside the nucleus. The interactions with electrons change the electronic property of the material, and it distort/polarize it, thus the electrons form an unstable and transient virtual energy state.

During the light-matter interaction, a very small amount of the photons heading from the photon cannon which is the laser, reach and collide deeply with the nucleus of the material, which could be in the ground state or in an excited vibrational state. Hence an exchange of energy between the photon and the molecule occur, causing an energy and frequency shift of the scattered light. The photons of the laser beam ($\vec{k} \approx 0$) interact inelastically with phonons (\vec{k}_i) causing a shift in their energy, which is a shift in the frequency. From momentum conservation rule we see

$$\sum_{i=1}^{i=n} \vec{k}_i = \vec{k}_{scattered} - \vec{k}_{incident} \approx 0 \quad (2.1)$$

Therefore only optical phonons with $\vec{k} \approx 0$, which are located in the center of the Brillouin zone, are allowed to interact with the incoming photons. Then these photons are accumulated to the camera, that displays the data in our computer where the data is observed. When the scattering happens, molecules are excited to an intermidate state called the virtual state, these molecules can relax back to 3 possible vibrational states (see figure 2.6) [23])

1. Their initial state.
2. A higher vibrational state.
3. A lower vibrational state.

The first possibility is called Rayleigh scattering. It occurs when an elastic collision happens, and we are not interested in this type of scattering since no frequency shift occurs, also it causes fluorescence. The second possibility is known as the "Stoke's frequency shift" when the molecule decays to a higher vibrational

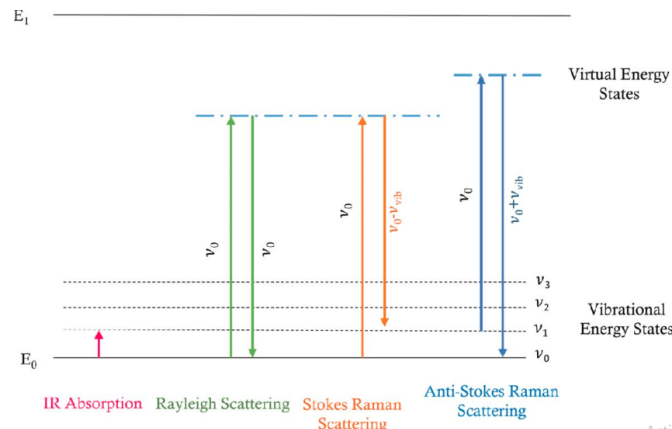


Figure 2.6: Vibrational States of Molecule Excitation

state than the one it was excited from (which is the lowest state). This possibility is of interest since it shows a frequency shift. The third possibility called the "Anti-Stoke's frequency shift" also shows the frequency shift needed and it reduces fluorescence, but the price we pay is in the intensity.

This paragraph is to discuss fluorescence mentioned before, that is a divergence from Raman spectroscopy. Fluorescence is the noisy light that appears and disrupt our figure of the proper inelastic scattering. The cause of it, is when a molecule gets excited to a new energy level; not to an intermediate virtual state as mentioned before, but to an excited electronic energy state, and upon this excitation; by nature, it gets back to the electronic ground state (see Figure 2.2). When the molecule gets back to the ground state from the excited state it emits a Rayleigh photon and this photon causes the fluorescence. The molecule gets excited to the higher vibrational energy state in the excited electronic state because of Frank-Condon principle[24], then it rolls down through the vibrational states to emit a photon and relaxes back to the ground electronic state. The critical point here is the efficiency, which can be very high compared to Raman photons. If the molecule has an energy level that can absorb the photon, it will preferentially do that and cause fluorescence, and this means that this efficiency is so high and a lot of photons are inefficient for Raman. One way to get rid of fluorescence is to burn the electronic levels by emitting photons to bleach it, this is called photobleaching, but it comes with a risk of damaging the molecule, so we will look for another technique to reduce fluorescence. One can notice that the photon gets back to the higher vibrational state of the ground electronic state, which means that it is lower in energy than the energy that excited the molecule just like Stoke's, where anti-Stoke's is on the other side. One piece is missing that is the Boltzmann distribution, the anti-Stoke's intensity has the form of exponential decay, it is because for it the energy difference of the levels become bigger and bigger which is less likely for the molecule to occupy higher states.

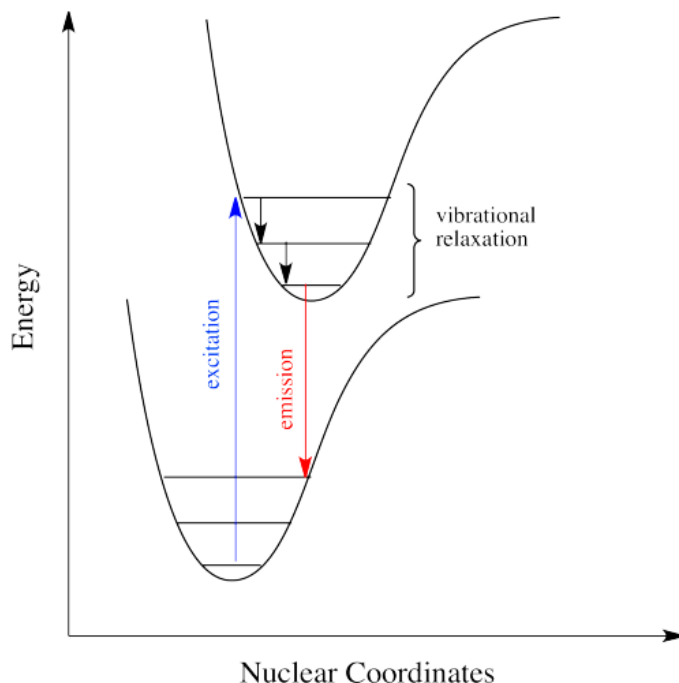


Figure 2.7: Fluorescence

2.2.2 Theoretical Basis

In this section, we intend to discuss the theoretical basis of what causes a molecule to scatter a Raman light. A molecule; which we assume to be diatomic, can undergo what is called ring breathing when the atom-atom bonds all stretch at once and the molecule just breaths. If we think back to Infrared, the fundamental rule of IR is that there must be a change in the dipole moment $\vec{\mu}$. Mathematically the intensity of this is proportional to

$$I \propto \int \psi^* \vec{\mu} \psi d\tau$$

Where ψ^* is the excited wavefunction and ψ is the ground wavefunction. If the dipole moment change is zero, then all of the above is zero and we do not see the IR spectrum. In Raman, we are not looking at the dipole moment. Instead, we look at the polarizability. Polarizability is the ability to polarize, which is the ability of an incident electric field to generate a dipole in the molecule, this property is material dependent, in which the molecular structure and the corresponding bonds defines the polarizability of the material. Imagine when the molecule ring stretches it becomes a bigger molecule, the electronic cloud associated with it moves out, now that is a polarizability change, and the way it is written

$$\vec{\mu}_{Ind} = \vec{\alpha} \cdot \vec{E} \quad (2.2)$$

Where α is the polarizability tensor and E is the strength of the electric field from the incident electromagnetic wave. When we illuminate an electromagnetic field on the matter, the orbits on which the electrons are moving are perturbed periodically with the same frequency as the incident electric field[25]. Now the separation of the charges is caused by the oscillation of the perturbed electronic cloud. The oscillating dipole moment is pronounced for the source of electromagnetic radiation that scatters light. A massive amount of light is scattered with the same frequency of the incident one; that what we called Rayleigh scattering, and another small amount scatter with different frequency that is Raman active. So the point here is that we are not dealing with dipoles but with induced dipoles caused by polarisability change.

We can write the polarisability tensor as function of normal coordinates Q , where

$$Q = Q_0 \cos(2\pi\nu_{vib}t) \quad (2.3)$$

So that the polarisability is written as (using Taylor expansion) [26]:

$$\alpha_{ij} = \alpha_{ij}^0 + \left(\frac{\partial \alpha_{ij}}{\partial Q} \right)_{Q=Q_0} \cdot Q \quad (2.4)$$

The polarisation is as follows:

$$P = \vec{\alpha} \times \vec{E}_0 \cos(2\pi\nu_{las}t) \quad (2.5)$$

$$P_i = \sum_j \alpha_{ij} \times E_j = \sum_j [\alpha_{ij}^0 E_{0j} \cos(2\pi\nu_{las}t) + \frac{E_{0j} Q_0}{2} \left(\frac{\partial \alpha_{ij}}{\partial Q} \right)_{Q=Q_0} \times [\cos(2\pi(\nu_{las} - \nu_{vib})t) + \cos(2\pi(\nu_{las} + \nu_{vib})t)] + \dots \quad (2.6)$$

We can see from equation (2.6) the elastic ($\nu = \nu_{las}$) and inelastic parts ($\nu = \nu_{las} + / - \nu_{vib}$) of light scattering. The first part is responsible for Rayleigh scattering, and the second parts happens when $\left(\frac{\partial \alpha_{ij}}{\partial Q} \neq 0 \right)$, which is when vibrations change polarisability, therefore the intensity proportionality for Raman scattering is different from zero [27].

From the electromagnetic theory of radiation from an oscillating dipole moment, we conclude that Raman lines has Lorentzian shape according to the following formula of the intensity and frequency :

$$I(\tilde{\nu}) = I_0 \times \int_{BZ} \frac{d^3 \vec{k}}{[\tilde{\nu} - \tilde{\nu}(\vec{k})]^2 + \left(\frac{\Gamma_0}{2} \right)^2} \quad (2.7)$$

Where $\tilde{\nu}(\vec{k})$, is the dispersion branch for the selected mode, and Γ_0 is the intrinsic full width at half maximum. Also the term $d^3 \vec{k}$ is an adjustable term to the shape of the material. We can see the contributions from electrical term (the polarisability α_{ij}), and the mechanical term (ν_{vib}); from I_0 , which explains here the sensitivity of Raman spectroscopy to these additional contributions, such as:

1. Electrical terms: Charge transfer (band structure, and ion-covalency) will change as an aspect of the vibration induced charge variation.
2. Mechanical terms: Material geometry, atomic mass, and bond strength will identify the peak positions.

2.2.3 Building The Raman System: Lasers

Since in fluorescence, we were talking about excited Energy levels and how to avoid the excitation of the molecule to these levels, then we should consider the cause of this excitation which is the laser. When building the Raman setup, the laser plays a massive role in terms of the quality of the data collected. So, choosing the laser should get under a proper level of understanding the effect of the laser beam in the interaction with the molecules. As mentioned before, fluorescence is caused by the photon emission from the excited electronic level due to the excitation of the molecule to this level. The first idea to avoid fluorescence is obvious, that is to use a laser that does not have enough energy to get the molecule to the excited state. If the laser is low in energy such that the molecule will end up in the intermediate virtual state rather than the real excited electronic state, then the molecule will not fluoresce, which is no need for it to emit a photon. From here we consider using a green laser of less energy power which is higher in the wavelength, so will come up short in the fluorescence level, and now we are in the virtual state (see figure 2.8 [28]), and we will end up in Raman scattering.

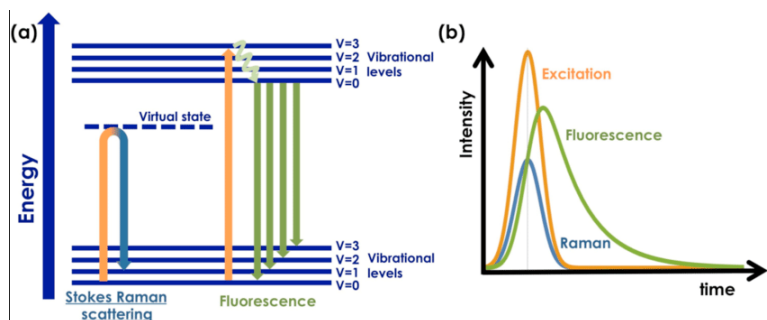


Figure 2.8: (a) Energy level diagram for Raman scattering and fluorescence emission; (b) temporal variation of excitation, Raman scattering and fluorescence emission.

Merchants offer laser of wavelength 785nm that are low in energy, this sounds really good, but why we don't use the 785nm laser and get the job done? First rule in spectroscopy: You never get something for nothing. Here relies one of many compromises that have to be made in Raman spectroscopy. The efficiency is proportional to the inverse of the fourth power of the wavelength.

$$Efficiency = \frac{1}{\lambda^4}$$

So as the laser wavelength gets larger, the Raman efficiency plummets, here we see the trade off. With fluorescence we want the long wavelength so the material will not fluoresce, but for efficiency; the Raman scattering efficiency that actually gets to the detector, becomes low, depending on the molecule. As a user one has to know how to balance these two issues, which is to know what laser to use.

2.2.4 Raman Sensitivity to Polarization

There is also one subtlety in Raman spectroscopy which we will explore now; it is polarization. Let us just not confuse this with what we have said before, polarisability. Polarisability has to do with the ability to cause change in the electronic cloud, while polarization has to do with the polarization of the light being vertical or horizontal. What we will talk about here is how the Raman can be sensitive to the polarization of the light or polarization of the scatter.

One way that a molecule can move is by what we call the normal mode; this normal modes are represented mathematically by "q" in the literature. They define the linear independent ways that a molecule can vibrate. For instance, let us take a molecule with atoms forming bonds with other atoms, for a specific structure of this molecule and specific normal mode, this molecule can go symmetry stretching. Now that does not change the dipole, if we look to the IR spectrum, we will see nothing there, but it does generate a sizeable Raman peak. The other interesting thing is when we stretch these bonds; weather they are stretching or compressing; either way, it does not change the symmetry. The molecule has to be mathematically correct about it to have some type of symmetry, and when it is stretched it maintains its shape. Because of this, when we look at the Raman scattering from the molecule if we use a laser that is polarized (I_{vv} or I_{vh}); let us say polarized vertically, and the detector channel is also polarized vertically (that is called I_{vv} , where the first index stands for light polarization and the second for the detector) so we have four different combinations of polarization. Now in case of vv, if we look at the mentioned type of normal mode that maintains the molecule's shape, we see a large peak for Raman signal, but for vh we see almost nothing, and that is the key: The polarization of Raman scattering is sensitive to this symmetry of the molecule. Polarization is also sensitive to the alignment of molecules if the molecules are aligned on the surface and we hit them with vertically polarized light that lines up with the molecules, we will see a strong Raman scattering. If we rotate the laser's polarization we will not see a strong Raman scattering. The idea of polarization is that if the symmetry is maintained, we get a polarized peak, while if it is broken, we get a depolarized ratio. In my research I used non-polarized laser light, where for this all the spectrum; which is the vibrational modes, appear on the screen.

2.2.5 Raman Instrumentation

Laser

Let us just look at Raman instrumentation from a classical point of view (see figure 2.9). First of all, we need a photon cannon which is the laser. Earlier, they used Mercury lamps or Xenon lamps to have the work of a photon source, but why now we choose lasers? The key is, in order for the Raman peaks to come out with natural line shape, we need to have a source that is very narrow energetically. If that source has broadness (like a white light), then the emission will have a broad shape, so instead of having sharp peaks, we will see peaks that are shaped like the source. The advantage of the laser is two-fold: One, it has the narrow linewidth (like a spike almost). Second, it has lots of photons. The massive number of photons have their advantage in a way by dealing with the efficiency of Raman scattering. As we discussed before, we saw that Rayleigh scattering and fluorescence are more efficient than Raman scattering, so the added amount of photons enhances the chance for a photon to get inelastic scattering so that these photons can accumulate and show a Raman peak at some frequency.

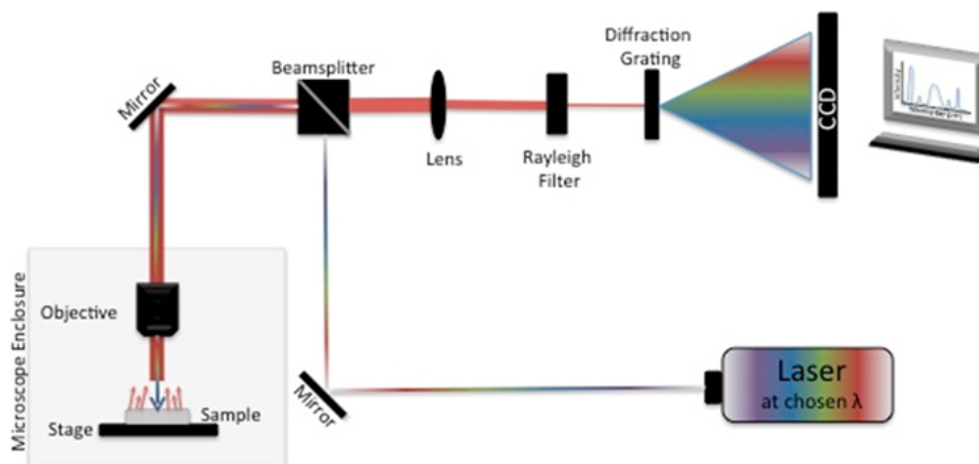


Figure 2.9: Raman Instrumentation

Polarizer

We should have a polarizer that polarizes the beam coming in. The light is then collected by some lens and focused on the entrance slit, but we should have one added thing here, that is the analyzer. The analyzer (which is the second polarizing element) that allows us to go through the different combinations of polarization.

Rayleigh Filter

The other thing that we will be putting here, and it is frequently put just right in front of the entrance slit of the spectrometer is the filter. We have to have the filter to eliminate the Rayleigh light because if we do not eliminate this light, it will get into the detector and burn it up.

Grating

The next thing is that light enters to some sort of diffraction element, the simplest is the grating. This diffraction grating spreads the light out over its spectral range, so now we have light all coming together, then spread out. We get the red light coming at some angle, the green light coming at a different angle, and the violet light coming at a different angle also, now they are spread out.

Detectors

Charge couple device (CCD) detectors are commonly used in Raman machines and so this detector has its duty in our setup. It is an array detector of silicon based multichannel array which are sensitive to light, and it allows multichannel operations giving a chance for detecting the spectrum at once. The light is diffracted from the grating toward the arrays of the CCD, noting that the spectral range depends on the length of the array and focal length of the spectrograph.

2.2.6 Raman Opto-thermal Technique

One other use of Raman spectroscopy is to determine the thermal conductivity, this was attributed to the successful work of Balandin and co-workers. Thermal conductivity is defined by Fourier heat law $q = \kappa \cdot \delta T$, where q is the heat flux density, δT is the temperature gradient along some region, and κ is the thermal conductivity. Thermal conductivity varies with temperature, also for it is direction-dependent. As we know, thermal conductivity describes how well heat is conducted through different materials. From here, we should engage heat carriers which are responsible for heat conduction. Heat carriers can be the free electrons or the phonons (The vibrational modes in a lattice), which means that both can contribute to the thermal conductivity of the material. The methods of measuring thermal conductivity can be divided into two groups:

- i) The Transient Method
- ii) The Steady-State Method

The transient way is a time-dependent technique, where the "laser flash" and the "3w" methods are an example of this process. Balandin and co-workers in-

roduced this technique for measuring the thermal conductivity for single layer graphene [29]. Raman technique analyzes photons coming to the detector after interacting with the lattice vibrational modes demonstrated by phonons; after this inelastic scattering, we observe the energy exchange. The Raman laser is a photon cannon that acts as a temperature source by its power ability. To conduct thermal conductivity exploiting this technique, two steps should be done. At first we modify the laser power and observe the Raman active peak shift. Secondly, to correlate the Raman peak shift to the temperature of the laser beam, we follow this shift by means of an external heat source after lowering the power of the laser to a minimum value which ensures that no heat is induced by the laser. Now we can obtain the slope ξ , that relates the temperature change with the power change $\delta T = \delta w / \xi$. This parameters are used to extract thermal conductivity upon solving the heat diffusion equation. One more parameter is needed which is the absorption power of the material. This technique is not restricted to the dimensions of the material, it can be examined on 2 dimensional, Bulk and 1D materials.

2.2.7 Raman Study of ZnO Crystal

ZnO has presented itself as a considerable competitor in UV optoelectronic devices and in the electronics domain. Its wide-bandgap semiconductor (3.4 eV) and large exciton binding energy (60 meV) made ZnO have some fundamental advantages over GaN[30]. ZnO is a Wurtzite-type crystal, and it belongs to C_{6v}^4 space group with two formula units in the primitive cell. Since Raman spectroscopy works on $q=0$ phonons, we investigate the zone centre optical phonons and find them to have the following irreducible representation: $\Gamma_{opt} = A_1 + E_1 + 2E_2 + 2B_1$. The B_1 mode has no appearance neither in Raman nor in infrared setups, A_1 and E_1 modes are polar and both Raman and infrared active, while E_2 modes are non-polar and Raman active only.

The study of the vibrational properties and the dynamics of heat carriers movements in a material boosts our knowledge on the criteria governing heat conductance. To get deep in the vibrational properties of the materials, we should realize its phonon population of different levels, which has a direct effect on the efficiency of high-speed optoelectronic devices [31]. Raman inelastic scattering measurement is a fast, non-destructive and a perfect technique in assessing the quality of a wide-bandgap semiconductor, it studies the phonons lifetime and it investigates specific aspects of lattice dynamics. Raman introduced itself as a perfect temperature probing technique for materials during device operations. The discovery of the different mechanisms of light-material scattering interactions ignited researchers to study these effects for various materials utilizing Raman spectroscopy. Damen *et al* started ZnO Raman measurement back in 1965 [32].

Continued by Arguello *et al* [33] who sought different geometries of ZnO and reported on Raman peaks, he obtained all Raman active mode frequencies using selection rules. Few years passed, and Calleja and Cardona [4] presented the resonant behaviour of the high frequency $E_2(\text{high})$, $A_1(\text{TO})$ and $E_1(\text{TO}, \text{LO})$ modes. Lately, an *ab-initio* density functional theory (DFT) was published, that helped more in understanding the available data possible.

2.2.8 First-Order Raman Spectrum of ZnO

In the following sections we intend to discuss the first and second order Raman spectrum of ZnO crystal, and their associated symmetries. The E_2 high mode frequency shows an asymmetry in its corresponding line shape. This asymmetry is justified by the sharpness of the edge of the two phonon density of states near the E_2 high frequency. The Raman spectroscopy line-shape; thus full width at half maximum value, could be observed with some uncertainty. The instrumental broadening correction is calculated by using this formula:

$$\Delta_L = \Delta - \frac{\Delta_G^2}{\Delta} \quad (2.8)$$

Where in this equation Δ is the full width at half maximum measured on the Raman spectrum, and Δ_L is the intrinsic FWHM. In the paper "Temperature Dependence of Raman scattering in ZnO", Cusco *et al.* [34] found the instrumental width to be less than 1 percent of the measured one. In this paper, the first part of the author's work is to report the Raman peaks of ZnO with their associated symmetries using polarized Raman scattering measurements in different configurations. The results of the associated Raman active modes are displayed in table (2.1). Their associated Raman tensors are:

Scattering geometry	E_2	$A_1(\text{LO})$	$A_1(\text{TO})$	$E_1(\text{LO})$	$E_1(\text{TO})$
$z(\text{xx})\bar{z}$	A	A			
$z(\text{xy})\bar{z}$	A				
$x(\text{yy})\bar{x}$	A		A		
$x(\text{zy})\bar{x}$					A
$x(\text{zy})y$				A	A

Table 2.1: Raman Active Modes

$$\begin{aligned}
E_2^{(1)} &= \begin{pmatrix} d & 0 & 0 \\ 0 & -d & 0 \\ 0 & 0 & 0 \end{pmatrix} & E_2^{(2)} &= \begin{pmatrix} 0 & d & 0 \\ d & 0 & 0 \\ 0 & 0 & 0 \end{pmatrix} \\
E_1(x) &= \begin{pmatrix} 0 & 0 & c \\ 0 & 0 & 0 \\ c & 0 & 0 \end{pmatrix} & E_1(y) &= \begin{pmatrix} 0 & 0 & 0 \\ 0 & 0 & c \\ 0 & c & 0 \end{pmatrix} \\
A_1(z) &= \begin{pmatrix} a & 0 & 0 \\ 0 & a & 0 \\ 0 & 0 & b \end{pmatrix} & & & (2.9)
\end{aligned}$$

Where the coordinate in parenthesis represents the polarization type of the associated phonon. The $E_1(LO)$ mode is the only mode missing in the backscattering geometry, unlike the other modes, from which all are derived from the Raman tensors. The cause of the absence of the $E_1(LO)$ mode is due to the change of the phonon polarization and the polarizability components involving z components in the vibration, which makes this mode untraceable. On the other hand, the observation of this mode is achieved by the scattering configuration of symmetry $x(zy)y$, in which the components here are non-vanishing. Figure (2.10) aids this discussion, also it shows polarized first order Raman spectra.

As observed from figure (2.10), in the back-scattering configuration $z(xx)\bar{z}$, the dominant modes are the E_2 low and E_2 high modes, belonging to the ($E_2 + A_1$ symmetry). The E_2 low mode, attributed to the Zn motion, is observed at 99cm^{-1} and it shows very narrow line-width. The second observed peak is for E_2 high vibrational mode and it is detected at 482cm^{-1} , it shows a clear asymmetry in the direction of low frequency region. Although the work of Calleja and Cardona [4] denied the observation of the $A_1(LO)$ mode for excitation wavelength greater than 406.7nm , where here in this work the excitation wavelength is 514.5nm corresponding to Ar^+ laser, and the $A_1(LO)$ peak is observed at 574cm^{-1} . An additional peak is observed at 333cm^{-1} which is a second-order Raman peak and will be discussed later. In the second configuration geometry $x(yy)\bar{x}$ ($E_2 + A_1$ symmetry), the E_2 modes appear with high intensity, but an extra peak appears at 378cm^{-1} which corresponds to $A_1(TO)$ mode. An extra peak exists having a frequency 410cm^{-1} in the $x(zy)\bar{x}$ spectrum (E_1 symmetry), which is attributed to $E_1(TO)$ mode. Finally for the last configuration, the $E_1(LO)$ mode is observed at 590cm^{-1} in the $x(zy)y$ spectrum. This last observed mode ($E_1(LO)$) marks the mode with the highest frequency in the first-order Raman spectrum of ZnO, which appears to have a frequency greater than of ($A_1(LO)$), of value 16cm^{-1} . This is unnoticed in DFT calculations, in a way that this calculation has predicted that $E_1(LO)$ mode to be lower from $A_1(TO)$ mode by 4cm^{-1} . A scarce intensity corresponding to the E_2 mode appears in both configurations $x(zy)\bar{x}$ and $z(zy)y$, this could be due to the contribution of some x components in the z polarization direction caused by misalignment of the sample.

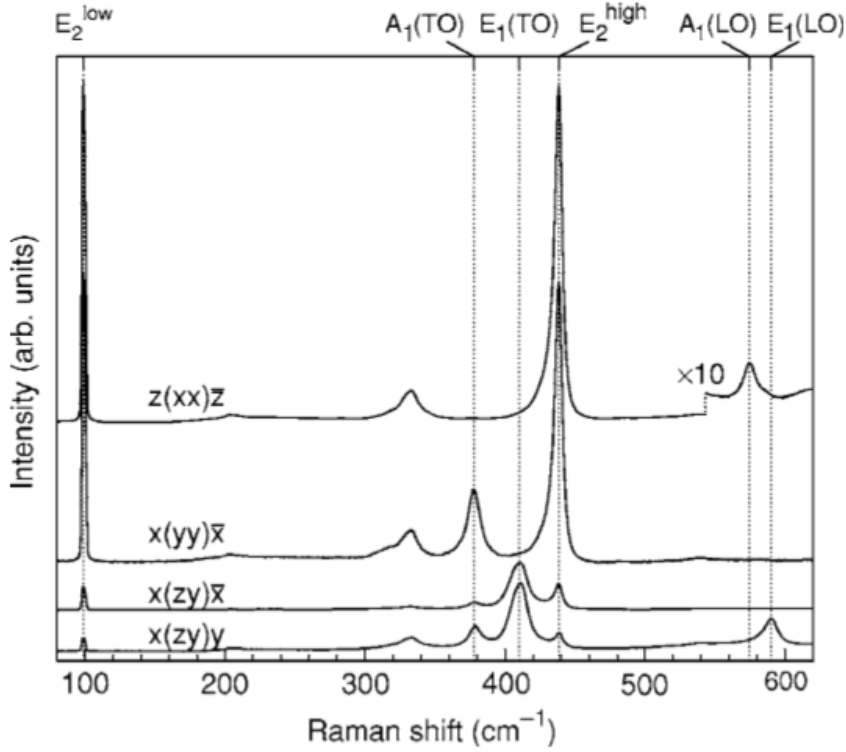


Figure 2.10: First order Raman study of the $A_1 + E_2 + E_1$ scattering geometries at room temperature.

2.2.9 Second Order Raman Spectrum of ZnO

The first order Raman scattering results from the interaction of the incoming electromagnetic wave represented by its quanta; the photon particle, with the zone-center optical phonons of $q = 0$. The scattered photons in the second-order Raman scattering have had interacted with phonons from the entire Brillouin zone. This spectrum is determined by the phonon density of state (DOS), and by using the selection rules of two-phonon scattering. The selection rules are reported by Seigle *et al.* [35], on the other hand the DOS were determined by DFT calculations by J. Serrano [36]. All first order and second order Raman peaks of ZnO are shown in figure (2.11) the results are reported by Cusco *et al.* and compared with the results from [4].

The DOS calculated using DFT calculation shows a frequency gap between acoustic and optical phonon frequencies. The gap starts from 270cm^{-1} to 410cm^{-1} . Therefore, we can divide the second order spectra into 3 regions.

1. Region One: Dominated by acoustic phonons overtones, and it is in the frequency region from $160\text{-}540\text{cm}^{-1}$.
2. Region Two: It is a high frequency region where the optical phonons over-

Frequency (cm ⁻¹)		Symmetry	Process	Brillouin zone points/lines
Our data	Ref. 13			
99	101	E_2	E_2^{low}	Γ
203	208	$A_1, (E_2)$	$2TA; 2E_2^{\text{low}}$	$L, M, H; \Gamma$
284		A_1	$B_1^{\text{high}} - B_1^{\text{low}}$	Γ
333	332	$A_1, (E_2, E_1)$	$E_2^{\text{high}} - E_2^{\text{low}}$	Γ
378	380	A_1	$A_1(\text{TO})$	Γ
410	408	E_1	$E_1(\text{TO})$	Γ
438	437	E_2	E_2^{high}	Γ
483		A_1	$2LA$	$M-K$
536	541	A_1	$2B_1^{\text{low}}; 2LA$	$\Gamma; L, M, H$
574	574	A_1	$A_1(\text{LO})$	Γ
590	584	E_1	$E_1(\text{LO})$	Γ
618		A_1	$TA+TO$	H, M
657		E_1, E_2	$TA+LO$	L, H
666		A_1	$TA+LO$	M
700		A_1	$LA+TO$	M
723		A_1	$LA+TO$	$L-M$
745		A_1	$LA+TO$	$L-M$
773		A_1	$LA+TO$	M, K
812		A_1	$LA+LO$	L, M
980	990	A_1	$2TO$	$L-M-K-H$
1044		A_1	$TO+LO$	A, H
1072	1080	A_1	$TO+LO$	M, L
1105		A_1	$2LO$	H, K
1158	1160	A_1	$2A_1(\text{LO}), 2E_1(\text{LO}); 2LO$	$\Gamma; A-L-M$

Figure 2.11: First and second order Raman spectra of ZnO and their symmetries, compared to ref [4], the symmetries in parenthesis represents lower intensities of the dominant symmetry configuration.

tones prevail on other branches and this region extends from 820-1120cm⁻¹.

3. Region Three: This region is the intermediate region in the frequency range 540-820cm⁻¹, and it contains both branches, the optical and acoustic phonons.

As mentioned before, the identification of the second-order Raman spectra is obtained by using phonon dispersion and selection rules for two-phonon Raman scattering. Figure (2.12) shows the temperature dependence of the second-order Raman peaks of ZnO in the $z(xx)\bar{z}$ polarization. It shows an eminent peaks corresponding LO overtones, and other combinations of this branch, noting that this branch is in the high frequency region. Another wide peak of high intensity at 1158cm⁻¹ includes contributions from $2E_1(LO)$ and $2A_1(LO)$ modes, and it is situated at the Γ point in the first Brillouin zone. One other possibility of the origin of this peak comes from the scattering of $2LO$ by mixed modes from the flat bands along $A-L-M$ line. Directly below this frequency, a peak is observed at 1105cm⁻¹ at the H and K points which refers to $2LO$. In the first section

we mentioned that a mismatch between DFT calculations and measured spectra has been observed for sequence of E_1 and A_1 (LO) modes, in a manner that measured spectrum shows that $E_1(LO)$ mode exceeds $A_1(LO)$ mode by 16cm^{-1} , whereas calculations show that $E_1(LO)$ comes before $A_1(LO)$ by 4cm^{-1} . Add to this ambiguity, DFT calculation despises LO frequencies in general, which implies that the calculated Raman peaks in this region are lower than the measured ones. In high frequency region, two shoulders of the prominent peak at 1158cm^{-1} exist at 1044 and 1072cm^{-1} , specially at low temperature. The first peak at 1044cm^{-1} is assigned to $TO + LO$ combination in the points A and H in the Brillouin zone. The second peak at 1072cm^{-1} also is attributed to $TO + LO$ combinations but it is located in points M and L in the Brillouin zone. A weak band appears at 980cm^{-1} which is from TO overtones, one thing we realize here is that LO modes' scattering efficiency is greater than the processes of TO modes.

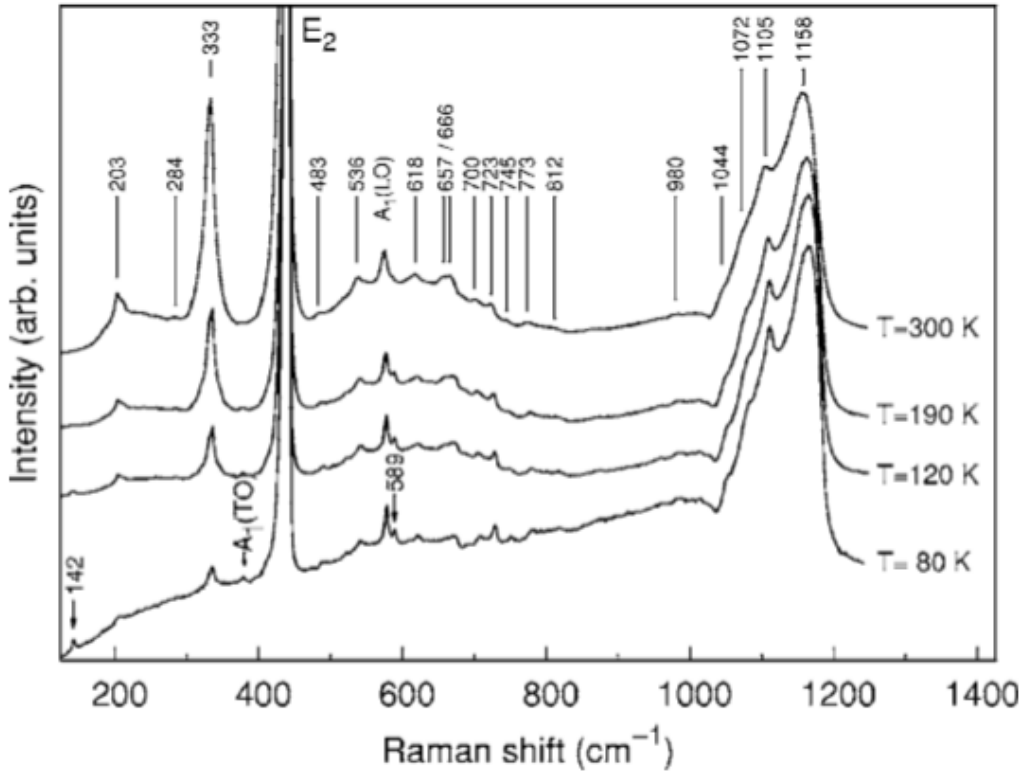


Figure 2.12: Temperature dependence of second order Raman peaks in ZnO.

Having finished the analysis of the peaks in the high frequency region, we move to the low-intermediate frequency region, where multiplicity of structures appear there. To get familiar with their symmetries, figure (2.13) shows the peaks in this region with their associated symmetries. The most eminent peak is at 333cm^{-1} , which was thought to be TA overtone at point M in the Brillouin zone.

However in figure (2.12), we observe the temperature dependence of this peak and it appears to show a difference mode. The 333cm^{-1} frequency happens to be the difference between E_2 high and E_2 low modes. According to the notation in [35] the difference mode contains symmetry $\Gamma_6 \otimes \Gamma_6 \supset A_1$. Figure (2.11) gives further justification of this peak, when it shows peaks corresponding to their symmetry, it indicates that the symmetry of the 333cm^{-1} mode is dominated by A_1 symmetry, and small contribution appear from E_2 symmetry, and even smaller peaks emerge from E_1 symmetry. DFT calculations show that this peak could also belong to some contributions from $[TO - TA]_{A,L,H}$ differences. On the other hand, the contributions from the theoretically justified symmetry has to make this peak of higher frequency and to have E_1 symmetry. In order to explain the origin of this peak, figure(2.13) shows the Raman intensity of this peak renormalized to its room temperature intensity, and we compare it with 2 calculations: First, the statistical occupation factor of the $E_2^{high} - E_2^{low}$ mode. Secondly, the statistical occupation factor for TA overtones. For the first calculation we use

$$\rho(T) = [1 + n(E_2^{high})]n(E_2^{low}) \quad (2.10)$$

Where $n(E)$ displays Bose-Einstein distribution. The statistical occupation number for the second calculation, which represents TA phonon is, $\hbar\omega_{TA} = 160\text{cm}^{-1}$. This calculations are represented in figure (2.14). The graph shows that the sta-

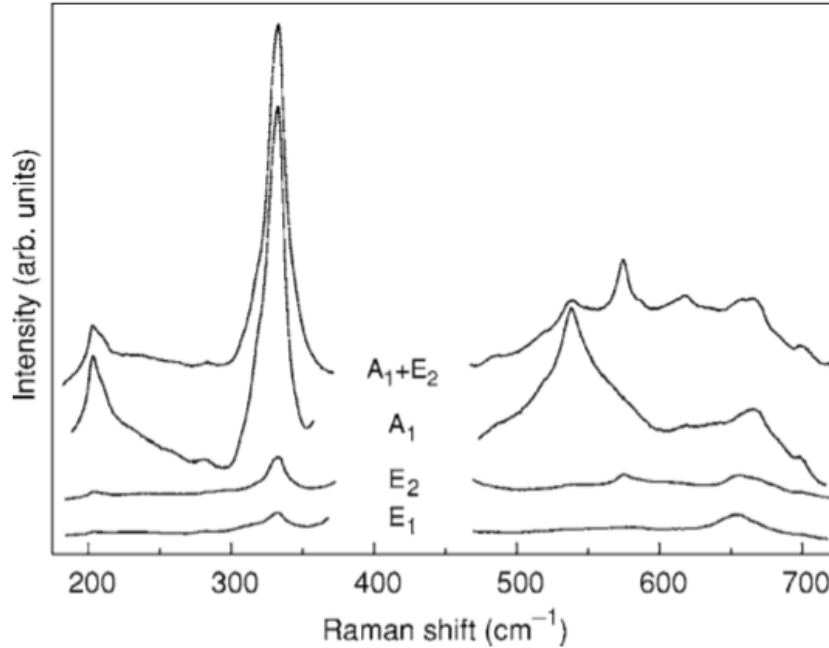


Figure 2.13: Second order peak of ZnO obtained for different scattering geometries. From bottom to top, $x(z\bar{y})\bar{x}$, $z(xy)\bar{z}$, $x(zz)\bar{x}$, and $z(xx)\bar{z}$.

tistical occupation factor of $E_2^{high} - E_2^{low}$ difference mode best fits the experimental

data, therefore the assumption of the 333cm^{-1} mode to have A_1 symmetry is correct. A weak peak appears at 284cm^{-1} which is temperature dependent peak, because at room temperature it appears with weak intensity, but its presence disappears at lower temperature, this suggests the possibility that this peak is a difference mode peak. We look at figure (2.13) to define the symmetry of this peak, it shows A_1 symmetry. Many difference modes give the value of the associated frequency of this peak, but not all of them show same symmetry. This suggests that this peak can only be attributed to the $B_1^{high} - B_1^{low}$ difference mode. The two peaks at 483 and 536cm^{-1} show A_1 symmetry, and are attributed to LA overtones alone $M - K$ and $L - M - H$.

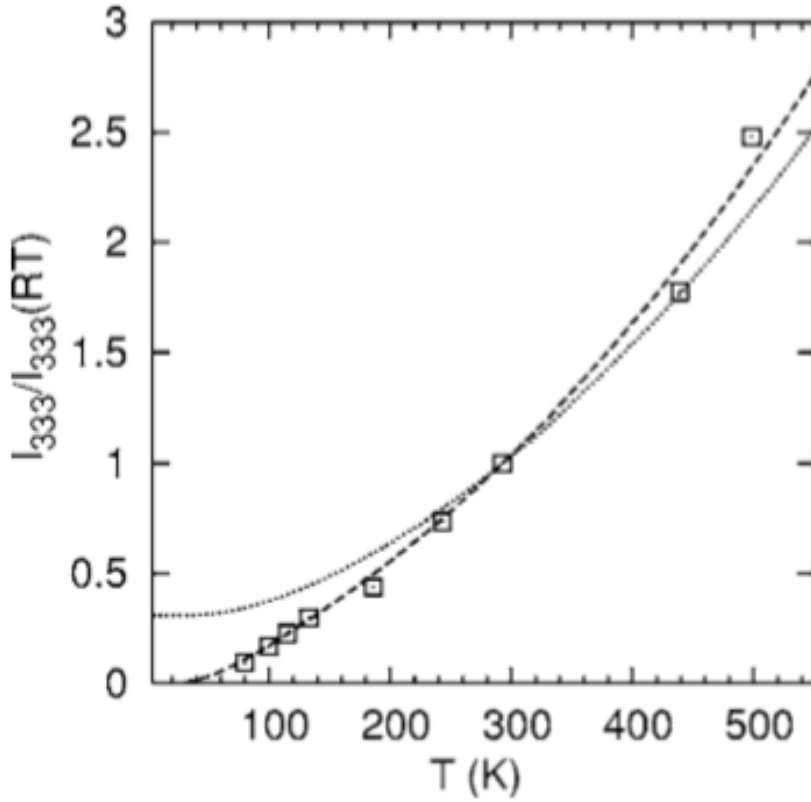


Figure 2.14: Intensity of the second order peak at 33cm^{-1} normalized to its value at room temperature. The dashed line represents the calculation for the difference mode $E_2^{high} - E_2^{low}$, while the dotted line is for TA overtones around point M

In the intermediate region, we find combinations from acoustic and optical phonons. In this region, one observes a peak at 618cm^{-1} that is $TA + TO$ at H and M points. Also, this combination gives birth to a doublet observed at $657-666\text{cm}^{-1}$, which have E_1 and E_2 symmetry for the first at 657cm^{-1} and A_1 symmetry for the second. As in intermediate region we have peaks attributed

to combinations from both acoustic and optical phonons, these peaks are of low intensity and are shown at 700, 723, 745, 773, and 812 cm^{-1} . These peaks are common for having A_1 symmetry, whereas the peak at 700 cm^{-1} is caused by $LA + TO$ combinations at point M , on the other hand, the last peak in this region is from $LO + LA$ combinations at L and M points.

2.3 Anharmonicity

2.3.1 Introduction

We analyze a crystal with N atoms to have $3N$ degrees of freedom, each demonstrating a normal mode. As we describe the photon to be the quantum of the electromagnetic wave, we treat the phonon to be the quantum of energy for the normal mode of vibration, although it is a quasi-particle, we associate to it a quasi-momentum $\hbar q$. The term quasi-particle is in its place here since the phonon's momentum is coded in the q wave vector, which cannot increase indefinitely. When the phonon holds energy equals to $\hbar G$ (where G is the reciprocal lattice vector), Bragg reflection takes place, and $\hbar G$ momentum is transferred to the whole lattice. As in the previous treatment for the crystal, it was approximated to have non-interacting phonons, where only nearest neighbours of an atom are allowed to exchange energy with it, linked by the force constants between them. The real picture differs from this one, as in this approximation, only the harmonic part of the lattice potential is active, and most of the results are derived from it, but there exists the anharmonic part upon expanding the lattice potential in Taylor series in powers of displacement. When the anharmonic terms appear, the temperature of the lattice increases and the anharmonic terms act as a perturbation on the harmonic part of the lattice potential, hence altering the lattice parameters, and changing the lattice constants. We intend now to discuss the lattice Hamiltonian of a 3D lattice, taking into consideration the lowest anharmonic terms in the potential and following the phonon-phonon interaction caused by the anharmonic terms.

2.3.2 Model of Vibrational Diatomic Lattice

We consider linear chain of two types of atoms of masses M_1 and M_2 .

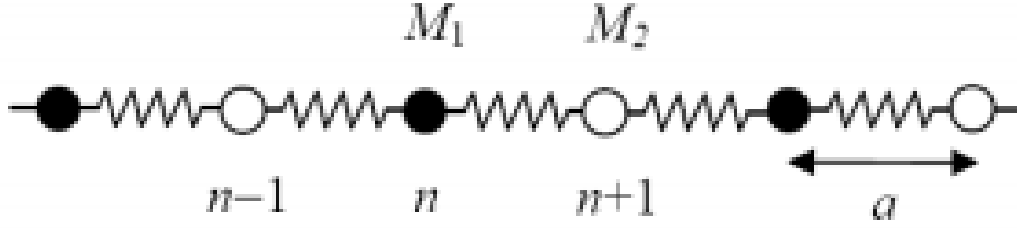


Figure 2.15: Diatomic Linear Chain

Where ' n ' labels the index of each atom and ' a ' is the separation between atoms. To obtain the frequencies of vibration we solve the equations of motions of this system. We treat this system by writing two equations of motion for each atom (one of mass M_1 and the other of mass M_2). Therefore we obtain:

$$\begin{aligned} M_1 \frac{d^2 u_n}{dt^2} &= -C(2u_n - u_{n+1} - u_{n-1}) \\ M_2 \frac{d^2 u_{n+1}}{dt^2} &= -C(2u_{n+1} - u_{n+2} - u_n) \end{aligned} \quad (2.11)$$

The letter "C" here stands for the force constant between the atoms (assuming same force constant between different atoms). Also u is the displacement of each atom from its equilibrium position, where every atom is labeled by the index n , so that $n + 1$ is the next atom. To solve these equations, we look at a solution for the displacement of the form :

$$\begin{aligned} u_n &= A_1 \exp^{i(qna - wt)} \\ u_{n+1} &= A_2 \exp^{i(q(n+1)a - wt)} \end{aligned} \quad (2.12)$$

Where here A is the maximum displacement, q is the wave vector and w is the frequency. Now we come to the substitution of this suggested solutions to the equations of motion and solve this system. Therefore, to ease our work of solving the two system of equations obtained, we do it in the matrix form:

$$\begin{bmatrix} 2C - M_1 w^2 & -2C \cos(qa) \\ -2C \cos(qa) & 2C - M_2 w^2 \end{bmatrix} \begin{bmatrix} A_1 \\ A_2 \end{bmatrix} = 0$$

What we need now is to solve the determinant of the above matrix to be zero, in other words:

$$(2C - M_1 w^2)(2C - M_2 w^2) - 4C^2 \cos^2(qa) = 0 \quad (2.13)$$

We solve this equation to get the dispersion relation:

$$w^2 = C \left(\frac{1}{M_1} + \frac{1}{M_2} \right) \pm \sqrt{\left(\frac{1}{M_1} + \frac{1}{M_2} \right)^2 - \frac{4 \sin^2(qa)}{M_1 M_2}} \quad (2.14)$$

We observe from the above solution, the existence of two different solutions depending on the sign, therefore obtaining two different dispersion curves.

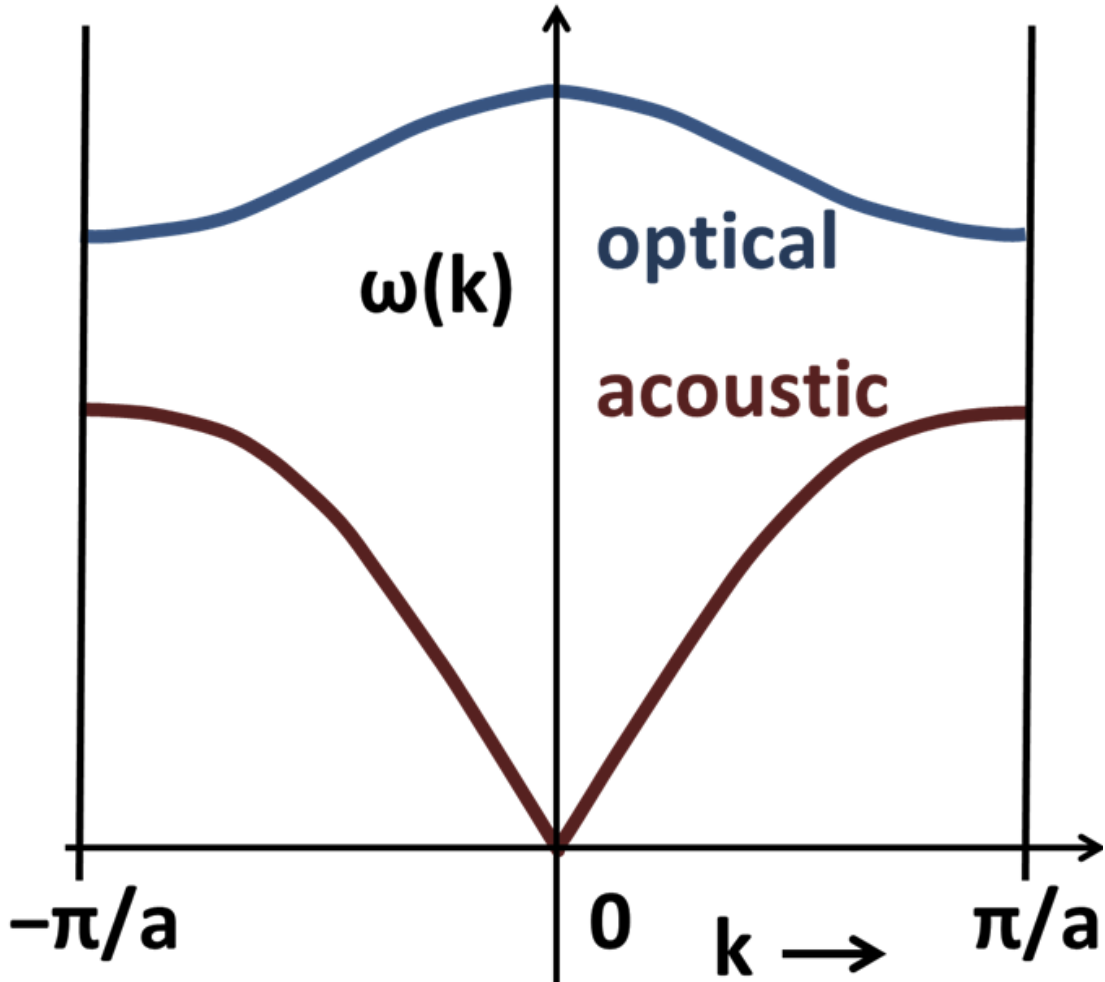


Figure 2.16: Dispersion Curve

A frequency gap is obvious in the vibrational spectrum of phonons, as there exist modes that can't be attained by the phonons. Therefore, the phonons are grouped into acoustic branch and optical branch. Where in the optical branch, vibrational modes exist at $q = 0$, which is at the center of the Brillouin zone, where we see a non-zero value of frequency. This zone-center phonon interacts with light that matches its wave vector $k = 0$, therefore this branch is responsible for light-matter interactions. As $q \rightarrow 0$, the acoustical branch frequency $w \rightarrow 0$, and so from the above dispersion relation we find that $A_1 = A_2$, concluding that the two atoms in the cell have the same amplitude and the phase dispersion is linear for small q . On the other hand, for the optical branch when $q \rightarrow 0$, $w = \sqrt{2C(\frac{1}{M_1} + \frac{1}{M_2})}$, arriving to $M_1A_1 + M_2A_2 = 0$, so that the center of mass

of the atoms remains fixed. The two atoms move out of phase. The optical branch gives more freedom for the phonon to vibrate. If there are p atoms in the primitive cell, there are $3p$ branches to the dispersion relation: 3 acoustical branches and $3p-3$ optical branches. Each phonon has 3 degrees of freedom in each branch (two transverse and one longitudinal), as transverse motion means that the phonons are vibrating perpendicularly to the wave's direction, and there exist two behaviours of perpendicular motion of phonons with respect to the wave's direction in 3D systems. The longitudinal motion is when the phonon is moving in the same direction or parallel to the wave's direction. In what follows we label a phonon branch by the index j .

2.3.3 Hamiltonian Of 3d Crystal

We build our model for a general 3D crystal. To make our model simple, we associate a position vector l for a unit cell in the crystal, and atomic position b for an atom in the unit cell. For this purpose, and in this section, we follow what Srivastava did in his book (The Physics of Phonons [37]). In this model and for the harmonic approximation, we consider the motion of the atoms to resemble the harmonic oscillators, where only nearest neighbours are allowed to exchange energy. From here, we need to know the displacement of each atom from its equilibrium position, which happens to be :

$$u(lb) = x(lb) - (l + b) \quad (2.15)$$

Where $x(lb)$ is the actual coordinate of the b th atom. As we mentioned before, in this treatment we intend to expand the potential in a Taylor series in powers of the displacement in order to analyze the contribution of the anharmonic terms:

$$\begin{aligned} V &= V_0 + \sum_{l,b,\alpha} \frac{\partial V}{\partial u_{\alpha}(lb)} \Big|_0 + \frac{1}{2} \sum_{l,b,l',b'} \sum_{\alpha,\beta} \frac{\partial^2 V}{\partial u_{\alpha}(lb) \partial u_{\beta}(l'b')} \Big|_0 u_{\alpha}(lb) u_{\beta}(l'b') \\ &+ \frac{1}{3!} \sum_{l,b,l',b'',l''} \sum_{\alpha,\beta,\gamma} \frac{\partial^3 V}{\partial u_{\alpha}(lb) \partial u_{\beta}(l'b') \partial u_{\gamma}(l''b'')} \Big|_0 u_{\alpha}(lb) u_{\beta}(l'b') u_{\gamma}(l''b'') + \dots \\ &= V_0 + V_1 + V_2 + V_3 + \dots \end{aligned} \quad (2.16)$$

The term V_0 which stands for the zero potential can be set to be zero, also the term in V_1 ($\frac{\partial V}{\partial x(lb)} \Big|_0 = 0$), which describes the force on the equilibrium state to have minimal energy. Then equation (3.2) transforms to:

$$\begin{aligned} V &= \frac{1}{2} \sum_{l,b,l',b'} \sum_{\alpha,\beta} \phi_{\alpha,\beta}(lb, l'b') u_{\alpha}(lb) u_{\beta}(l'b') \\ &+ \frac{1}{3!} \sum_{l,b,l',b'',l''} \sum_{\alpha,\beta,\gamma} \psi_{\alpha,\beta,\gamma}(lb, l'b', l''b'') u_{\alpha}(lb) u_{\beta}(l'b') u_{\gamma}(l''b'') \end{aligned} \quad (2.17)$$

Where both ϕ and ψ are matrices (cartesian tensors of second and third rank with 9 and 27 elements respectively) defined as :

$$\phi_{\alpha,\beta}(lb, l'b') = \frac{\partial^2 V}{\partial u_\alpha(lb) \partial u_\beta(l'b')} \Big|_0 \quad (2.18)$$

$$\psi_{\alpha,\beta,\gamma}(lb, l'b', l''b'') = \frac{\partial^3 V}{\partial u_\alpha(lb) \partial u_\beta(l'b') \partial u_\gamma(l''b'')} \Big|_0 \quad (2.19)$$

Moving to the crystal Hamiltonian we define the momentum operator $p(lb)$ to be the atom momentum operator located at $l + b$ with mass m_b . Now we can write:

$$\begin{aligned} H = & \sum_{l,b} \frac{p(lb)p(lb)}{2m} + \frac{1}{2} \sum_{l,b,l',b'} \sum_{\alpha,\beta} \phi_{\alpha,\beta}(lb, l'b') u_\alpha(lb) u_\beta(l'b') \\ & + \frac{1}{3!} \sum_{l,b,l',b',l'',b''} \sum_{\alpha,\beta,\gamma} \psi_{\alpha,\beta,\gamma}(lb, l'b', l''b'') u_\alpha(lb) u_\beta(l'b') u_\gamma(l''b'') \end{aligned} \quad (2.20)$$

When needed we can impose the cyclic boundary condition on the displacement for a D lattice, which happens to be :

$$u_b(l) = u_b(l + N_1 a_1) = u_b(l + N_2 a_2) = u_b(l + N_3 a_3) \quad (2.21)$$

We can see that from the Hamiltonian in equation (2.20) is somehow complicated and needs to be renormalized. One way of simplification is by adjusting the coordinates. The goal of simplifying this Hamiltonian is to achieve a diagonal representation of it. We start by making Fourier analysis for both the coordinates (u) and momentum (p) such that:

$$u(lb) = \frac{1}{\sqrt{N_0 \Omega}} \sum_q X(q, b) e^{iq l} \quad (2.22)$$

$$p(lb) = \frac{1}{\sqrt{N_0 \Omega}} \sum_q P(q, p) e^{-iq l} \quad (2.23)$$

Where $N_0 \Omega$ is the volume of the crystal and N_0 is the total number of unit cells upon multiplying the number of unit cells of each dimension together. We know that u and p both are hermitian, then for X and P we must have:

$$X^\dagger(q, b) = X(-q, b) = \frac{1}{\sqrt{N_0 \Omega}} \sum_l u(lb) e^{iq l} \quad (2.24)$$

$$P^\dagger(q, b) = P(-q, b) = \frac{1}{\sqrt{N_0 \Omega}} \sum_l p(lb) e^{-iq l} \quad (2.25)$$

Which implies that the new coordinates are non-hermitian and satisfy the following commutation relation:

$$\begin{aligned}
[X(q, b), P(q', b')] &= \frac{1}{N_0\Omega} \sum_{l, l'} e^{-i(q.l - q'.l')} [u(lb), p(l'b')] \\
&= \frac{1}{N_0\Omega} \sum_{l, l'} e^{-i(q.l - q'.l')} \hat{I} i \hbar \delta_{l, l'} \delta_{b, b'} \\
&= \hat{I} i \hbar \delta_{q, q'} \delta_{b, b'}
\end{aligned} \tag{2.26}$$

We conclude that if the new normal coordinates does not correspond to the same wave vector or basis vector, then they are independent variables, otherwise they are dependent and non-commuting. Now after the coordinate transformation we substitute equation (2.22) and (2.23) into equation (2.20):

$$\begin{aligned}
H &= \frac{1}{N_0\Omega} \sum_{q, q', l, b} \frac{P(q, b)P(q', b)}{2m_b} e^{-i(q+q').l} \\
&+ \frac{1}{2} \frac{1}{N_0\Omega} \sum_{q, q', l, b, l', b'} \sum_{\alpha, \beta} \phi_{\alpha\beta}(lb, l'b') X_\alpha(q, b) X_\beta(q', b') e^{i(q.l + q'.l')} \\
&+ \frac{1}{3!} \frac{1}{(N_0\Omega)^{\frac{3}{2}}} \sum_{\substack{q, q', q'' \\ lb, l'b', l''b''}} \sum_{\alpha, \beta, \gamma} \psi_{\alpha, \beta, \gamma}(lb, l'b', l''b'') X_\alpha(q, b) X_\beta(q', b') X_\gamma(q'', b'') e^{i(q.l + q'.l' + q''.l'')}
\end{aligned} \tag{2.27}$$

Further simplification is done by performing summation on l , in the first term of the previous equation:

$$\begin{aligned}
\text{First term} &= \sum_{q, q', b} \frac{P(q, b) \cdot P(q', b)}{2m_b} \frac{1}{N_0\Omega} \sum_l e^{-i.(q+q').l} \\
&= \sum_{q, q', b} \frac{P(q, b)P(q', b)}{2m_b} \delta_{q+q', 0} \\
&= \sum_{q, b} \frac{P(q, b) \cdot P^\dagger(q, b)}{2m_b}
\end{aligned} \tag{2.28}$$

Tracking the simplification of the second term, we use the lattice transformation symmetry, which allows us to write the force constant matrix as follows:

$$\phi_{\alpha, \beta}(lb, l'b') = \phi_{\alpha, \beta}(0b, (l' - l)b') \tag{2.29}$$

Upon introducing $h = l' - l$ and defining:

$$\begin{aligned}
\phi_{\alpha, \beta}(bb'|q) &= \sqrt{m_b m_b'} D_{\alpha, \beta}(bb'| - q) \\
&= \sum_h \phi_{\alpha, \beta}(0b, hb') e^{-iq.h}
\end{aligned} \tag{2.30}$$

we can write the second term in equation (2.13) as:

$$\text{Second term} = \frac{1}{2} \sum_{q,b,b',\alpha,\beta} \phi_{\alpha,\beta}(bb'|q) X_{\alpha}(q,b) X_{\beta}^{\dagger}(q,b') \quad (2.31)$$

This result is obtained by doing the summation on l of the second term in equation (2.27) and upon introducing (2.30). For the third term in (2.27), we follow the same method of simplification, thus we define $h' = l' - l$ and $h'' = l'' - l$. Then:

$$V_3 = \frac{1}{3!} \frac{1}{(N_0\Omega)^{\frac{3}{2}}} \sum_{qb,q'b',q''b''} \sum_{\alpha,\beta,\gamma} \sum_l e^{i(q+q'+q'')\cdot l} \psi_{\alpha,\beta,\gamma}(qb, q'b', q''b'') X_{\alpha}(q,b) X_{\beta}(q',b') X_{\gamma}(q'',b'') \quad (2.32)$$

Where

$$\psi_{\alpha,\beta,\gamma}(qb, q'b', q''b'') = \sum_{h',h''} \psi_{\alpha,\beta,\gamma}(0b, h'b', h''b'') e^{iq'h'} e^{iq''h''} \quad (2.33)$$

now doing the summation over l we get:

$$V_3 = \frac{1}{3!} \frac{1}{\sqrt{N_0\Omega}} \sum_{qb,q'b',q''b''} \delta_{G,q+q'+q''} \sum_{\alpha,\beta,\gamma} \psi_{\alpha,\beta,\gamma}(qb, q'b', q''b'') X_{\alpha}(q,b) X_{\beta}(q',b') X_{\gamma}(q'',b'') \quad (2.34)$$

Where G is the reciprocal lattice vector. Now after all these simplifications we look back to the previous Hamiltonian and introduce these terms in it, we get:

$$\begin{aligned} H = & \sum_{qp} \frac{P(q,b)P^{\dagger}(q,b)}{2m_b} + \frac{1}{2} \sum_{q,b,b',\alpha,\beta} \phi_{\alpha,\beta}(bb'|q) X_{\alpha}(qb) X_{\beta}^{\dagger}(q,b') \\ & + \frac{1}{3!} \frac{1}{\sqrt{N_0\Omega}} \sum_{\substack{qb,q'b',q''b'' \\ \alpha,\beta,\gamma}} \delta_{G,q+q'+q''} \cdot \psi_{\alpha,\beta,\gamma}(qb, q'b', q''b'') X_{\alpha}(q,b) X_{\beta}(q',b') X_{\gamma}(q'',b'') \end{aligned} \quad (2.35)$$

The crystal Hamiltonian is viewed in terms of the new coordinates $X(q,b)$ and $P(q,b)$, and the harmonic and anharmonic force constants $\phi(bb'|q)$ and $\psi(qb, q'b', q''b'')$. After the transformation to q , we intend to find the eigenstates of the Hamiltonian. This discussion can be completed by introducing the eigenstates of the system. For this purpose we introduce the polarisation vector $e(b|qs)$ that describes the magnitude and the direction of vibration of the atom (b) in the vibrational mode (qs). Here s can be transverse (T) or longitudinal (L) polarisation branch. One property of this eigenvector is:

$$\sum_b e^*(b|qs) \cdot e(b|qs') = \delta_{ss'} \quad (2.36)$$

Now we make further normal coordinate transformation as follow:

$$X(qs) = \sum_b \sqrt{m_b} e^*(b|qs) X(qb) \quad (2.37)$$

$$P(qs) = \sum_b \frac{1}{m_b} e(b|qs) P(qb) \quad (2.38)$$

When doing the previous normal coordinate transformation as in equations (2.37) and (2.38) we extend out crystal Hamiltonian simplification and do another set of transformations:

$$a_{qs} = \frac{1}{\sqrt{2\hbar w(q,s)}} P(qs) - i \sqrt{\frac{w(qs)}{2\hbar}} X^\dagger(qs) \quad (2.39)$$

$$a^\dagger_{qs} = \frac{1}{\sqrt{2\hbar w(qs)}} P^\dagger(qs) + i \sqrt{\frac{w(qs)}{2\pi}} X(qs) \quad (2.40)$$

Where the new operators $a(qs)$ and $a^\dagger(qs)$ are known to be the phonon annihilation and creation operators respectively. These operators obey the following relation:

$$[a(qs), a^\dagger(q's')] = \delta_{q,q'} \delta_{s,s'} \hat{I} \quad (2.41)$$

From equations (2.39) and (2.40) we get:

$$X(qs) = -i \sqrt{\frac{\hbar}{2w(qs)}} (a^\dagger_{qs} - a_{-qs}) \quad (2.42)$$

$$P(qs) = \sqrt{\frac{\hbar w(qs)}{2}} (a_{qs} + a^\dagger_{-qs}) \quad (2.43)$$

Where $w(-qs) = w(qs)$, $X^\dagger(qs) = X(-qs)$, and $P^\dagger(qs) = P(-qs)$. Now, from equations (2.37), (2.38), (2.42), and (2.43) we obtain :

$$\begin{aligned} X(qb) &= \frac{1}{\sqrt{m_b}} \sum_s e(b|qs) X(qs) \\ &= -i \sum_s \sqrt{\frac{\hbar}{2m_b w(qs)}} e(b|qs) (a^\dagger_{qs} - a_{-qs}) \end{aligned} \quad (2.44)$$

$$\begin{aligned} P(qb) &= \sqrt{m_b} \sum_s e^*(b|qs) P(qs) \\ &= \sum_s \sqrt{\frac{m_b \hbar w(qs)}{2}} e^*(b|qs) (a_{qs} + a^\dagger_{-qs}) \end{aligned} \quad (2.45)$$

These new transformations allow us to express the coordinate and momentum vectors in terms of the phonon creation and annihilation operators and the polarisation vectors which are the eigenstates of the Hamiltonian. We try to substitute equations (2.44) and (2.45) in the last obtained form of the Hamiltonian:

$$\begin{aligned}
\text{First term} &= \frac{1}{2} \sum_{qb} \frac{1}{m_b} P(qb) \cdot P^\dagger(qb) \\
&= \frac{1}{4} \sum_{qs} \hbar \omega(qs) (a_{qs} + a_{-qs}^\dagger) (a_{qs}^\dagger + a_{-qs}) \quad (2.46)
\end{aligned}$$

Where we use equation (2.36).

$$\begin{aligned}
\text{Second term} &= \frac{1}{2} \sum_{q,b,b',\alpha,\beta} \phi_{\alpha\beta}(bb'|q) X_\alpha(qb) X_\beta^\dagger(qb') \\
&= \frac{1}{2} \sum_{q,b,b',s,\alpha,\beta} \phi_{\alpha\beta}(bb'|q) \frac{\hbar}{2\omega(qs)} \frac{1}{\sqrt{m_b m_b'}} e_\alpha(b|qs) e_\beta^*(b'|qs) \cdot (a_{qs}^\dagger - a_{-qs}) (a_{qs} - a_{-qs}^\dagger) \\
&= \frac{1}{4} \sum_{q,b,s\alpha} \hbar \omega(qs) e_\alpha(b|qs) e_\alpha^*(b|qs) (a_{qs}^\dagger - a_{-qs}) (a_{qs} - a_{-qs}^\dagger) \\
&= \frac{1}{4} \sum_{qs} \hbar \omega(qs) (a_{qs}^\dagger - a_{-qs}) (a_{qs} - a_{-qs}^\dagger) \quad (2.47)
\end{aligned}$$

We now add the 2 terms to get :

$$\begin{aligned}
H_{\text{harm}} &= \text{term 1} + \text{term 2} \\
&= \frac{1}{4} \sum_{qs} \hbar \omega(qs) [(a_{qs} + a_{-qs}^\dagger) (a_{qs}^\dagger + a_{-qs}) + (a_{qs}^\dagger - a_{-qs}) (a_{qs} - a_{-qs}^\dagger)] \\
&= \frac{1}{4} \sum_{qs} \hbar \omega(qs) (a_{qs} a_{qs}^\dagger + a_{qs}^\dagger a_{qs} + a_{-qs} a_{-qs}^\dagger + a_{-qs}^\dagger a_{-qs}) \\
&= \frac{1}{2} \sum_{qs} \hbar \omega(qs) (a_{qs} a_{qs}^\dagger + a_{qs}^\dagger a_{qs}) \quad (2.48)
\end{aligned}$$

Upon obtaining this result we obeyed the fact that a summation over the allowed values of $-q$ duplicates that of q . Further simplification of the above result, when using the commutation relation in equation (2.27) we get for the Hamiltonian in the harmonic approximation to be :

$$H_{\text{harm}} = \sum_{qs} \hbar \omega(qs) (a_{qs}^\dagger a_{qs} + \frac{1}{2}) \quad (2.49)$$

As we pointed at the beginning, our goal was to achieve a Hamiltonian at its simplest form, which is to get the diagonal form from the Hamiltonian. In the last

equation we obtained this result after making two-step coordinate transformation. The first step was about changing the normal coordinate and momentum from the particle picture described by vectors l and b to the wave picture described by the wave vector q and the polarisation vector s . In the second step of transformation we presented the annihilation and creation operators (a_{qs} and a_{qs}^\dagger). To appreciate what we get, we try to calculate the crystal eigenvalues. First let us see the effect of the annihilation and creation operators on the phonon state $|n_{qs}\rangle$, for this we apply it and get the following:

$$\begin{aligned} a_{qs}^\dagger |n_{qs}\rangle &= \sqrt{n_{qs} + 1} |n_{qs} + 1\rangle \\ a_{qs} |n_{qs}\rangle &= \sqrt{n_{qs}} |n_{qs} - 1\rangle \\ a_{qs}^\dagger a_{qs} |n_{qs}\rangle &= n_{qs} |n_{qs}\rangle \end{aligned} \quad (2.50)$$

We see that while a_{qs} is responsible to annihilate a phonon from a phonon state and a_{qs}^\dagger to create a phonon, combined $a_{qs}^\dagger a_{qs}$ is the phonon number operator. Then by applying the Hamiltonian of the phonon eigenstates we get:

$$\begin{aligned} H_{harm} |n_{qs}\rangle &= \sum_{qs} \hbar\omega(qs) \left(n_{qs} + \frac{1}{2}\right) |n_{qs}\rangle \\ &= \sum_{qs} \epsilon_{qs} |n_{qs}\rangle \end{aligned} \quad (2.51)$$

We see that the eigenvalue of a 3D simple harmonic oscillator with the previous Hamiltonian is :

$$\epsilon_{qs} = \hbar\omega(qs) \left(n_{qs} + \frac{1}{2}\right) \quad (2.52)$$

And the average energy of a phonon in mode (qs) is :

$$\bar{\epsilon}_{qs} = \hbar\omega(qs) \bar{n}_{qs} \quad (2.53)$$

Where \bar{n}_{qs} is the average Bose-Einstein distribution function. After analyzing the harmonic part of the crystal Hamiltonian, we now proceed to the cubic anharmonic part V_3 . Using equations (2.44 and 2.45), we write the anharmonic term in equation (2.35) as follows:

$$\begin{aligned} V_3 &= \frac{1}{3!} \frac{1}{\sqrt{N_0}} (i) \sum_{\substack{qb, q'b', q''b'' \\ ss', \alpha\beta\gamma}} \left(\frac{\hbar^3}{8m_b m_b' m_b'' \omega(qs) \omega(q's') \omega(q''s'')} \right)^{\frac{1}{2}} \cdot \delta_{G, q+q'+q''} \\ &e_\alpha(b|qs) e_\beta(b'|q's') e_\gamma(b''|q''s'') \psi_{\alpha, \beta, \gamma}(qb, q'b', q''b'') \cdot (a_{qs}^\dagger - a_{-qs}) (a_{q's'}^\dagger - a_{q's'}) (a_{q''s''}^\dagger - a_{-q''s''}) \\ &= \frac{1}{3!} \sum_{qs, q's', q''s''} \delta_{G, q+q'+q''} \psi(qs, q's', q''s'') \cdot (a_{qs}^\dagger - a_{-qs}) (a_{q's'}^\dagger - a_{q's'}) (a_{q''s''}^\dagger - a_{-q''s''}) \end{aligned} \quad (2.54)$$

where

$$\psi(qs, q's', q''s'') = \frac{i}{\sqrt{N_0\Omega}} \sum_{bb'b''\alpha\beta\gamma} \left(\frac{\hbar^3}{8m_b m'_b m''_b w(qs)w(q's')w(q''s'')} \right)^{\frac{1}{2}} \cdot e_\alpha(b|qs) e_\beta(b'|q's') e_\gamma(b''|q''s'') \cdot \psi_{\alpha\beta\gamma}(qb, q'b', q''b'') \quad (2.55)$$

Similarly for four phonon process:

$$V_{\lambda, \lambda_1, \lambda_2, \lambda_3}^{(4)} = \sum_{0b, bl_1, bl_2, bl_3} \sum_{\alpha, \alpha_1, \alpha_2, \alpha_3} \Phi_{0b, bl_1, bl_2, bl_3}^{\alpha, \alpha_1, \alpha_2, \alpha_3} \cdot \frac{e_{\alpha b}^\lambda e_{\alpha_1 b_1}^{\lambda_1} e_{\alpha_2 b_2}^{\lambda_2} e_{\alpha_3 b_3}^{\lambda_3}}{\sqrt{m_b m_{b_1} m_{b_2} m_{b_3}}} \times e^{i.k_1.r_{11}} \cdot e^{i.k_2.r_{12}} \cdot e^{i.k_3.r_{13}} \quad (2.56)$$

Where λ describes the phonon mode. We should note here that the factor $\psi_{(qs, q's', q''s'')}$ is proportional to the the average of the Fourier transformed tensor $\psi_{(qb, q'b', q''b'')}$ that is projected on the directions of the various polarisation vectors $e(b|qs)$, $e(b'|q's')$ and $e(b''|q''s'')$.

Now we have completed the picture of the transformation of both the harmonic and anharmonic part in the crystal Hamiltonian using the second quantisation scheme for coordinate transformation. Note here, in this representation the harmonic part is diagonal, while the anharmonic part is not. This rises the possibility of interacting phonons that is missed in the harmonic part and ignored for a crystal with no perturbations or external forces or temperature acting on it.

2.3.4 Effects Of Anharmonicity On Phonon States

As we can see from equation (2.51), the harmonic part of the Hamiltonian introduces the picture of non-interacting phonons. We mentioned before our interest in the anharmonic part of the crystal Hamiltonian that was obtained after expanding the crystal potential in a Taylor series for the displacement. This anharmonic part acts as a perturbation on the harmonic one at finite temperature, that explains the existence of the anharmonic lattice forces in the crystal. This fact was born out from the appearance of the phonon peaks in neutron scattering, which ignited the assumption that anharmonicity can be viewed as a perturbation on the non-interacting phonon states. As we saw before that anharmonicity works with the the picture of interacting phonons. As seen from the cubic part in the potential V_3 explored before, in the first order this term causes three phonon interaction process, while it is responsible for four phonon interaction process in the second-order.

We intend to study now the V_3 term and how it can change the phonon states. We will discover the types of three phonon processes and their conservation rules.

As known, and due to the translational invariance in the crystal potential energy, the phonon wave vectors are under the restriction of the following equation:

$$q + q' + q'' = G \quad (2.57)$$

Where G is the reciprocal lattice vector, which can be zero. So that q , q' and q'' are restricted to the first Brillouin zone. When $G=0$, the phonon-phonon interaction process is called the normal or $N - process$ and it conserves momentum. While when G is different from zero, the process is called Umklapp process or $U - process$ and it does not conserve momentum.

From the last equation for the cubic anharmonic term of the crystal potential, we see that the part acting on the phonon states is summed in the term :

$$(a_{qs}^\dagger - a_{-qs})(a_{q's'}^\dagger - a_{-q's'})(a_{q''s''}^\dagger - a_{-q''s''}) \quad (2.58)$$

Expanding this term yields to:

$$\begin{aligned} & a_{qs}^\dagger a_{q's'}^\dagger a_{q''s''}^\dagger - a_{qs}^\dagger a_{q's'}^\dagger a_{-q''s''} - a_{qs}^\dagger a_{-q's'} a_{q''s''}^\dagger \\ & + a_{qs}^\dagger a_{-q's'} a_{-q''s''} - a_{-qs} a_{q's'}^\dagger a_{q''s''}^\dagger + a_{-qs} a_{q's'}^\dagger a_{-q''s''} \\ & + a_{-qs} a_{-q's'} a_{q''s''}^\dagger - a_{-qs} a_{-q's'} a_{-q''s''} \end{aligned} \quad (2.59)$$

The three phonon states includes the phonon density of states and it is:

$$|n_{qs}n_{q's'}n_{q''s''} > \quad (2.60)$$

This three phonon state is acted on by the above operators mentioned in equation (2.59), governed by the rules in equation (2.50). So for the first term of equation (2.59) its effect is to increase by one each of the phonons in the states represented by qs , $q's'$ and $q''s''$ respectively, and so on for the rest of the terms as the operator a^\dagger creates a phonon in some wave vector mode and polarisation mode, and a operator annihilates a phonon. An important conclusion is extracted from equation (2.59) which distinguishes between 4 different basic processes of three-phonon interactions, we list them :

1. Annihilation of two phonon and creation of a third one (class 1 events).
2. Creation of two phonons and annihilation of one (class 2 events).
3. Simultaneous creation of three phonons.
4. Simultaneous annihilation of 3 phonons.

However only the first two possibilities are achievable as they conserve energy, while the second two possibilities violates energy conservation rules, which are marked to be possible as virtual three-phonon processes considering higher order anharmonic processes.

Let us track energy and momentum conservation law for class 1 and class 2 events for annihilation or creation a phonon in mode qs .

Class 1 events:

$$\begin{aligned} w(qs) + w(q's') &= w(q''s'') \\ q + q' &= q'' + G \end{aligned} \tag{2.61}$$

Class 2 events:

$$\begin{aligned} w(qs) &= w(q's') + w(q''s'') \\ q + G &= q' + q'' \end{aligned} \tag{2.62}$$

In class 1 events, 2 phonons with modes qs and $q's'$ respectively interact, as a result of this interaction, these 2 phonons get annihilated and a third phonon is created in the mode $q''s''$. There are 2 possible ways for this interaction to be done, arising from the summation of $q + q'$. The first possibility is when the summation lies in the first Brillouin zone, therefore the momentum is conserved and this is what we call *N-process*, and it conserves momentum. The second possibility is when the summation $q + q'$ extends to escape the boundaries of the first Brillouin zone, so it needs to be flipped back inside it, and this is done by an appropriate reciprocal lattice vector G that returns the resultant vector from the summation of the first 2 vector into the first Brillouin zone. This process does not conserve momentum and its called *U-process*. We see here that the resultant wave vector q'' is opposite in direction to $q + q'$ because of the intervention of the reciprocal lattice vector G that returns it to the first Brillouin zone, this intervention changes the direction of q'' , and hence it creates a resistance to the heat flow by phonons. See figure (2.17). The interaction in the second class event has the same interpretation as this one.

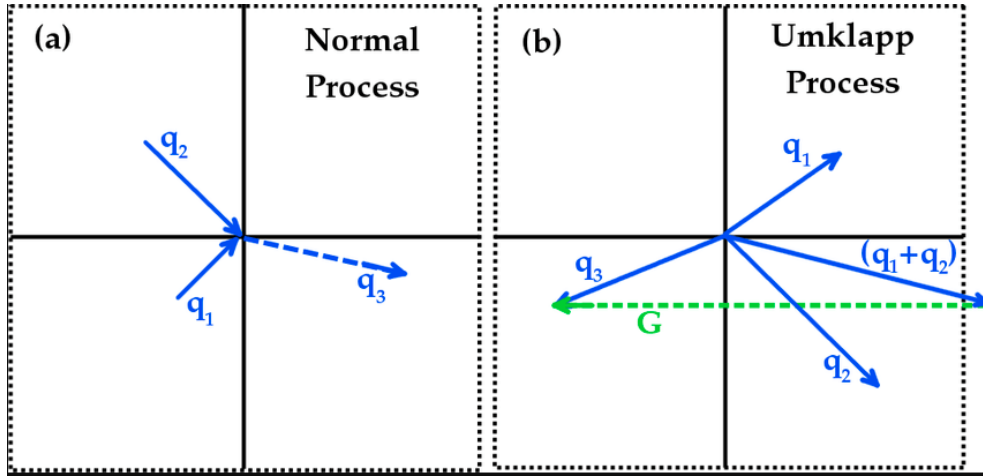


Figure 2.17: (a) N-Process (b) U-process.[5]

2.3.5 Anharmonicity effects on Phonon Self Energy, Responsible For The Frequency and Lifetime Change

One might think that the extra parts in the Hamiltonian of the atom only serve for the purpose of having high precision in calculations. This is wrong. Two new physical properties appear when introducing the extra terms in the Hamiltonian. The first appearing phenomena is under the category of equilibrium properties and it is the thermal expansion effect. The second one is a transport property, which destroys the idea of infinite thermal conductivity of the lattice in the picture of non-interacting phonons, and introduces new phonon interaction mechanisms. In his paper, Cowley [38] recognised the effect of the anharmonic part of the phonon Hamiltonian on the parts of the phonon self energy, and deduced that this part of the Hamiltonian changes the phonon's self energy components with respect to frequency and temperature, therefore they are dependent on this two parameters. The change with respect to frequency is related to the position of the mode's frequency with respect to the two-phonon density of states. This is a renormalisation of the bare harmonic frequency with respect to frequency. The other change is related to the temperature change, and it effects both parts of the phonon self energy, which are the real and imaginary parts. The first is responsible for the frequency change, and the second describes lifetime change.

The anharmonic part of the Hamiltonian is :

$$\begin{aligned}
H_A = & \sum_{\vec{q}_1, \vec{q}_2, \vec{q}_3} \sum_{j_1, j_2, j_3} V \begin{pmatrix} \vec{q}_1 & \vec{q}_2 & \vec{q}_3 \\ j_1 & j_2 & j_3 \end{pmatrix} A(\vec{q}_1, j_1) A(\vec{q}_2, j_2) A(\vec{q}_3, j_3) \\
& + \sum_{\vec{q}_1, \vec{q}_2, \vec{q}_3, \vec{q}_4} \sum_{j_1, j_2, j_3, j_4} V \begin{pmatrix} \vec{q}_1 & \vec{q}_2 & \vec{q}_3 & \vec{q}_4 \\ j_1 & j_2 & j_3 & j_4 \end{pmatrix} A(\vec{q}_1, j_1) A(\vec{q}_2, j_2) A(\vec{q}_3, j_3) A(\vec{q}_4, j_4)
\end{aligned} \tag{2.63}$$

With $A(\vec{q}, j) = a_{\vec{q}, j} + a_{-\vec{q}, j}^\dagger$ representing the phonon creation and annihilation operators. The change of the frequency as an effect of the anharmonic interactions is as follows :

$$w^2(\vec{0}, j; \Omega) = w^2(\vec{0}, j) + 2w(\vec{0}, j)[\Delta(\vec{0}, j; \Omega) + i\Gamma(\vec{0}, j; \Omega)] \tag{2.64}$$

For small real and imaginary parts of phonon self energy; compared to the frequency $w(\vec{0}, j)$, the above equation transforms to :

$$w(\vec{0}, j; \Omega) = w(\vec{0}, j) + \Delta(\vec{0}, j; \Omega) + i\Gamma(\vec{0}, j; \Omega) \tag{2.65}$$

The effect of the anharmonic Hamiltonian on the real and imaginary parts of the phonon self energy is as follows, the three lowest order contribution to the real part is :

$$\begin{aligned}
\Delta(0, j; \Omega) = & \Delta^{(0)} + \frac{12}{\hbar} \sum_{\vec{a}, j'} V \begin{pmatrix} \vec{0} & \vec{0} & \vec{q} & -\vec{q} \\ j & J & j' & j' \end{pmatrix} [2n(\vec{q}, j') + 1] \\
& - \frac{18\pi}{\hbar^2} \sum_{\vec{q}, j_1, j_2} \left| V \begin{pmatrix} \vec{0} & \vec{q} & -\vec{q} \\ j & j_1 & j_2 \end{pmatrix} \right|^2 [n(\vec{q}, j_1) + n(-\vec{q}, j_2) + 1] \left[\frac{1}{w(\vec{q}, j_1) + w(\vec{q}, j_2) - \Omega} \right]_P
\end{aligned} \tag{2.66}$$

The first order term ($\Delta^{(0)}$) is the thermal expansion contribution, which we will address later. This term and the second order term of the above equation are Ω independent. Whereas, for the third term, it is Ω and T dependent, and it contributes directly to the three phonon process interactions. For the line-shape, which is accounted by the imaginary part of the phonon self energy, the effect of the anharmonic Hamiltonian on it is as follows :

$$\Gamma(\vec{0}, j; \Omega) = -\frac{18\pi}{\hbar^2} \sum_{\vec{q}, j_1, j_2} \left| V \begin{pmatrix} \vec{0} & \vec{q} & -\vec{q} \\ j & j_1 & j_2 \end{pmatrix} \right|^2 [n(\vec{q}, j_1) + n(-\vec{q}, j_2) + 1] \delta(w(\vec{q}, j_1) + w(-\vec{q}, j_2) - \Omega) \tag{2.67}$$

The above equation is a manifest of an optical phonon decay to two phonons of energies $w(\vec{q}, j_1)$ and $w(-\vec{q}, j_2)$, reserving energy conservation by summing up

to the frequency Ω . In the beginning I've mentioned that both parts of the phonon self energy are frequency dependent, this is obvious when we take the matrix elements in the imaginary part of the phonon self energy to be constant, therefore:

$$\Gamma(\Omega) \propto \frac{1}{V} \sum_{\vec{q}, j_1, j_2} \delta(w(\vec{q}, j_1) + w(-\vec{q}, j_2) - \Omega) \equiv \rho^2(\Omega) \quad (2.68)$$

Otherwise, the matrix elements determining the width are:

$$\begin{aligned} V \begin{pmatrix} \vec{0} & \vec{q} & -\vec{q} \\ j & j_1 & j_2 \end{pmatrix} &= \frac{1}{6} \left[\frac{\hbar^3}{8NM^3 w_0 w(q, j_1) w(-q, j_2)} \right]^{\frac{1}{2}} \\ &+ \sum_{l', l''} \sum_{k, k', k''} \sum_{\alpha, \beta, \gamma} \phi_{\alpha\beta\gamma} \begin{pmatrix} 0 & l' & l'' \\ k & k' & k'' \end{pmatrix} e_{\alpha}(k|\vec{0}, j) e_{\beta}(k'|\vec{q}, j_1) e_{\gamma}(k''|-\vec{q}, j_2) e^{i\vec{q} \cdot [\vec{R}(l') - \vec{R}(l'')]} \end{aligned} \quad (2.69)$$

Where $\phi_{\alpha\beta\gamma}$ multiplied by the matrix following it, is the third order derivative of the inter-atomic potential, along the directions of the atoms. The index l represents the position of the primitive cell, while the index k points to the position of the atom inside the cell. The eigenvectors of the problem are $e(k|\vec{q}, j)$. N is the number of cells in the crystal and M is the atomic mass [39]. The cubic anharmonicity effect on the imaginary part of the phonon self energy to the second order in perturbation theory is :

$$\begin{aligned} \Gamma(w_0, T) &= \frac{18\pi}{\hbar^2} \sum_{qj_1j_2} |V_3(qj_1, -qj_2)|^2 [(n_1 + n_2 + 1)\delta(w_1 + w_2 - w) \\ &+ (n_2 - n_1)\delta(w_1 - w_2 - w)] \end{aligned} \quad (2.70)$$

Here $V_3(qj_1, -qj_2)$ is the third order coefficient in the expansion of the lattice potential in normal coordinates. One should note here that the real and imaginary parts of the phonon self energy are related by Kramers-Kronig relation :

$$\Delta(w) = -\frac{2}{\pi} P \int_0^{\infty} \frac{w'}{w'^2 - w^2} \Gamma(w') dw' \quad (2.71)$$

Where $\Delta(w)$ is the real part in the phonon self energy and it is responsible for the frequency shift, and $\Gamma(w)$ is the imaginary part in the phonon self energy and is responsible for the width change.

Another form of the frequency shift and lifetime equations that can be obtained from expanding the phonon self energy components to the three lowest order are :

$$\begin{aligned} \Gamma(w_0, T) &= \Gamma(w_0) + A \left[1 + \frac{1}{e^{\frac{\hbar w_1}{kT}} - 1} + \frac{1}{e^{\frac{\hbar w_2}{kT}} - 1} \right] \\ &+ B \left[1 + \frac{1}{e^{\frac{\hbar w_1}{kT}} - 1} + \frac{1}{e^{\frac{\hbar w_2}{kT}} - 1} + \frac{1}{e^{\frac{\hbar w_3}{kT}} - 1} \right] \end{aligned} \quad (2.72)$$

$$\begin{aligned}
w(w_0, T) = w_0 + \Delta^{(0)} + A & \left[1 + \frac{1}{e^{\frac{\hbar w_1}{kT}} - 1} + \frac{1}{e^{\frac{\hbar w_2}{kT}} - 1} \right] \\
& + B \left[1 + \frac{1}{e^{\frac{\hbar w_1}{kT}} - 1} + \frac{1}{e^{\frac{\hbar w_2}{kT}} - 1} + \frac{1}{e^{\frac{\hbar w_3}{kT}} - 1} \right]
\end{aligned} \tag{2.73}$$

Where here, it is clearly obvious that this equations are missing the contribution of the interaction of the modes frequency with the combinations of phonon in the two phonon density of states, whereas in the above constructed model, this interaction is immense. One would be curious to ask now how the width is related to the phonon lifetime of optical phonons, or in other words, how the rate of scattering is proportional to the line-width of the phonon peaks present in the Raman spectrum. The answer to this question is addressed in the following section where we have used Fermi golden rule to calculate the transition probabilities of three and four phonon process, to use them in calculating the phonon distribution decay rate using the single mode relaxation time approximation.

2.3.6 Fermi Golden Rule of Three and Four Phonon Processes

For the quantum calculation of the three and four phonon processes scattering rates, we apply the Fermi golden rule, of the interacting Hamiltonian of the mentioned processes on the initial and final phonon populations.

We consider a three phonon process where a phonon can decay to two phonons or vice versa, in other words:

$$\lambda \rightarrow \lambda_1 + \lambda_2 \tag{2.74}$$

Or

$$\lambda \leftarrow \lambda_1 + \lambda_2 \tag{2.75}$$

We take the initial state to be $|i\rangle = |n_\lambda + 1, n_{\lambda_1}, n_{\lambda_2}\rangle$, and the final state $|f\rangle = |n_\lambda, n_{\lambda_1} + 1, n_{\lambda_2} + 1\rangle$. To figure out the transition probability between this two states we utilize the Fermi golden rule in the following way [40]:

$$\begin{aligned}
& \frac{2\pi}{\hbar} | \langle f | \hat{H}_3 | i \rangle |^2 \delta(E_i - E_f) \\
& \sim |\sqrt{n_\lambda} \sqrt{1 + n_{\lambda_1}} \sqrt{1 + n_{\lambda_2}}|^2 |\hat{H}_{\lambda\lambda_1\lambda_2}^{(3)}|^2 \\
& \sim n_\lambda (1 + n_{\lambda_1}) (1 + n_{\lambda_2}) |\hat{H}_{\lambda\lambda_1\lambda_2}^{(3)}|^2
\end{aligned} \tag{2.76}$$

In the same manner we do it for $\lambda \leftarrow \lambda_1 + \lambda_2$:

$$\begin{aligned}
\frac{2\pi}{\hbar} &< i|\hat{H}_3|f \rangle|^2 \delta(E_i - E_f) \\
&\sim |\sqrt{1+n_\lambda} \sqrt{n_{\lambda_1}} \sqrt{n_{\lambda_2}}|^2 |\hat{H}_{\lambda\lambda_1\lambda_2}^{(3)}|^2 \\
&\sim (1+n_\lambda)n_{\lambda_1}n_{\lambda_2} |\hat{H}_{\lambda\lambda_1\lambda_2}^{(3)}|^2
\end{aligned} \tag{2.77}$$

We move forward to the rate of change of the occupation number of the phonon modes due to the three and four phonon processes :

$$\begin{aligned}
\left. \frac{\partial n_\lambda}{\partial t} \right|_s = & - \sum_{\lambda_1\lambda_2} \left(\frac{1}{2} [n_\lambda(1+n_{\lambda_1})(1+n_{\lambda_2}) - (1+n_\lambda)n_{\lambda_1}n_{\lambda_2}] L_- \right. \\
& + [n_\lambda n_{\lambda_1}(1+n_{\lambda_2}) - (1+n_\lambda)(1+n_{\lambda_1})n_{\lambda_2}] L_+ \left. \right) \\
& - \sum_{\lambda_1\lambda_2\lambda_3} \left(\frac{1}{6} [n_\lambda(1+n_{\lambda_1})(1+n_{\lambda_2})(1+n_{\lambda_3}) - (1+n_\lambda)n_{\lambda_1}n_{\lambda_2}n_{\lambda_3}] L_{--} \right. \\
& + \frac{1}{2} [n_\lambda n_{\lambda_1}(1+n_{\lambda_2})(1+n_{\lambda_3}) - (1+n_\lambda)(1+n_{\lambda_1})n_{\lambda_2}n_{\lambda_3}] L_{+-} \\
& \left. + \frac{1}{2} [n_\lambda n_{\lambda_1}n_{\lambda_2}(1+n_{\lambda_3}) - (1+n_\lambda)(1+n_{\lambda_1})(1+n_{\lambda_2})n_{\lambda_3}] L_{++} \right) \tag{2.78}
\end{aligned}$$

This transition rate is divided into two main parts. The first one concerns three phonon processes and the second one is related to the four phonon processes. On the other hand, the first part has 2 parts: The first one describes the splitting process $\lambda \rightarrow \lambda_1 + \lambda_2$, and the second part describes the combination process $\lambda + \lambda_1 \rightarrow \lambda_2$. Furthermore, the first part in the first term describes the decay rate of n_λ due to splitting process, where it shows the difference between the transition rates $\lambda \rightarrow \lambda_1 + \lambda_2$ and $\lambda \leftarrow \lambda_1 + \lambda_2$. The term L_\pm codes the required selection rules in energy and momentum for the interaction to occur. For the interaction to happen the energy conservation requires $w_\lambda \pm w_{\lambda_1} - w_{\lambda_2} = 0$, and momentum conservation, $k \pm k_1 + k_2 = R$. Normal processes put $R = 0$, while Umklapp processes has $R \neq 0$.

The second summation term stands for four phonon processes, where it contains 3 main terms describing the following transitions. First, the decay of a single phonon into three phonon: $\lambda \rightarrow \lambda_1 + \lambda_2 + \lambda_3$. Second, the combination of two phonons to give another two phonons: $\lambda + \lambda_1 \rightarrow \lambda_2 + \lambda_3$. Third, the combination of three phonons to give birth to one phonon: $\lambda + \lambda_1 + \lambda_3 \rightarrow \lambda_2$. Similarly the terms $L_{\pm\pm}$ codes the transition probabilities of the four phonon process to occur. The conservation laws of energy and momentum restricts the frequency $w_\lambda \pm w_{\lambda_1} \pm w_{\lambda_2} - w_{\lambda_3} = 0$, and the momentum $k \pm k_1 \pm k_2 - k_3 = R$. The terms L_\pm and $L_{\pm\pm}$ for the three and four phonon processes are the transition probabilities calculated from the Fermi golden rule, and they have the following

formulas:

$$\begin{aligned}
L_{\pm} &= 18 \times 2 \times \frac{2\pi}{\hbar} |\hat{H}_{\lambda\lambda_1\lambda_2}^{(3)}|^2 \delta(E_i - E_f) \\
&= \frac{\pi\hbar}{4N} |V_{\pm}^{(3)}|^2 \Delta_{\pm} \frac{\delta(w_{\lambda} \pm w_{\lambda_1} - w_{\lambda_2})}{w_{\lambda} w_{\lambda_1} w_{\lambda_2}}
\end{aligned} \tag{2.79}$$

And

$$\begin{aligned}
L_{\pm\pm} &= 96 \times 2 \times \frac{2\pi}{\hbar} |\hat{H}_{\lambda\lambda_1\lambda_2\lambda_3}^{(4)}|^2 \delta(E_i - E_f) \\
&= \frac{\pi\hbar}{4N} \frac{\hbar}{2N} |V_{\pm\pm}^{(4)}|^2 \Delta_{\pm\pm} \frac{\delta(w_{\lambda} \pm w_{\lambda_1} \pm w_{\lambda_2} - w_{\lambda_3})}{w_{\lambda} w_{\lambda_1} w_{\lambda_2} w_{\lambda_3}}
\end{aligned} \tag{2.80}$$

To simplify equation (2.78) we adopt the single mode relaxation time approximation (SMRTA). This approximation states that only the phonon mode we are dealing with is at non-equilibrium ; in other words it deviates from equilibrium, and all other modes are at equilibrium. For the phonon mode λ , the occupation number is :

$$n_{\lambda} = n_{\lambda}^{(0)} + n'_{\lambda} \tag{2.81}$$

On the other hand, the rest modes stay at equilibrium:

$$\begin{aligned}
n_{\lambda_1} &= n_{\lambda_1}^0 \\
n_{\lambda_2} &= n_{\lambda_2}^0 \\
n_{\lambda_3} &= n_{\lambda_3}^0
\end{aligned} \tag{2.82}$$

Also we use the following facts:

$$\begin{aligned}
\lambda \rightarrow \lambda_1 + \lambda_2 : n_{\lambda}^0 (1 + n_{\lambda_1}^0) (1 + n_{\lambda_2}^0) - (1 + n_{\lambda}^0) n_{\lambda_1}^0 n_{\lambda_2}^0 &= 0 \\
\lambda + \lambda_1 \rightarrow \lambda_2 : n_{\lambda}^0 n_{\lambda_1}^0 (1 + n_{\lambda_2}^0) - (1 + n_{\lambda}^0) (1 + n_{\lambda_1}^0) n_{\lambda_2}^0 &= 0 \\
\lambda \rightarrow \lambda_1 + \lambda_2 + \lambda_3 : n_{\lambda}^0 (1 + n_{\lambda_1}^0) (1 + n_{\lambda_2}^0) (1 + n_{\lambda_3}^0) - (1 + n_{\lambda}^0) n_{\lambda_1}^0 n_{\lambda_2}^0 n_{\lambda_3}^0 &= 0 \\
\lambda + \lambda_1 \rightarrow \lambda_2 + \lambda_3 : n_{\lambda}^0 n_{\lambda_1}^0 (1 + n_{\lambda_2}^0) (1 + n_{\lambda_3}^0) - (1 + n_{\lambda}^0) (1 + n_{\lambda_1}^0) n_{\lambda_2}^0 n_{\lambda_3}^0 &= 0 \\
\lambda + \lambda_1 + \lambda_2 \rightarrow \lambda_3 : n_{\lambda}^0 n_{\lambda_1}^0 n_{\lambda_2}^0 (1 + n_{\lambda_3}^0) - (1 + n_{\lambda}^0) (1 + n_{\lambda_1}^0) (1 + n_{\lambda_2}^0) n_{\lambda_3}^0 &= 0
\end{aligned} \tag{2.83}$$

Also the facts

$$\begin{aligned}
\lambda \rightarrow \lambda_1 + \lambda_2 : (1 + n_{\lambda_1}^0)(1 + n_{\lambda_2}^0) - n_{\lambda_1}^0 n_{\lambda_2}^0 &= \frac{n_{\lambda_1}^0 n_{\lambda_2}^0}{n_{\lambda}^0} = 1 + n_{\lambda_1}^0 + n_{\lambda_2}^0 \\
\lambda + \lambda_1 \rightarrow \lambda_2 : n_{\lambda_1}^0 (1 + n_{\lambda_2}^0) - (1 + n_{\lambda_1}^0) n_{\lambda_2}^0 &= \frac{(1 + n_{\lambda_1}^0) n_{\lambda_2}^0}{n_{\lambda}^0} = n_{\lambda_1}^0 - n_{\lambda_2}^0 \\
\lambda \rightarrow \lambda_1 + \lambda_2 + \lambda_3 : (1 + n_{\lambda_1}^0)(1 + n_{\lambda_2}^0)(1 + n_{\lambda_3}^0) - n_{\lambda_1}^0 n_{\lambda_2}^0 n_{\lambda_3}^0 &= \frac{n_{\lambda_1}^0 n_{\lambda_2}^0 n_{\lambda_3}^0}{n_{\lambda}^0} \\
\lambda + \lambda_1 \rightarrow \lambda_2 \lambda_3 : n_{\lambda_1}^0 (1 + n_{\lambda_2}^0)(1 + n_{\lambda_3}^0) - (1 + n_{\lambda_1}^0) n_{\lambda_2}^0 n_{\lambda_3}^0 &= \frac{(1 + n_{\lambda_1}^0) n_{\lambda_2}^0 n_{\lambda_3}^0}{n_{\lambda}^0} \\
\lambda + \lambda_1 + \lambda_2 \rightarrow \lambda_3 : n_{\lambda_1}^0 n_{\lambda_2}^0 (1 + n_{\lambda_3}^0) - (1 + n_{\lambda_1}^0)(1 + n_{\lambda_2}^0) n_{\lambda_3}^0 &= \frac{(1 + n_{\lambda_1}^0)(1 + n_{\lambda_2}^0) n_{\lambda_3}^0}{n_{\lambda}^0}
\end{aligned} \tag{2.84}$$

Therefore equation (2.78) becomes:

$$\begin{aligned}
\frac{\partial n'_{\lambda}}{\partial t} \Big|_s &= n'_{\lambda} \sum_{\lambda_1 \lambda_2} \left(\frac{1}{2} (1 + n_{\lambda_1}^0 + n_{\lambda_2}^0) L_- + (n_{\lambda_1}^0 - n_{\lambda_2}^0) L_+ \right) \\
&\quad - n'_{\lambda} \sum_{\lambda_1 \lambda_2 \lambda_3} \left(\frac{1}{6} \frac{n_{\lambda_1}^0 n_{\lambda_2}^0 n_{\lambda_3}^0}{n_{\lambda}^0} L_{--} + \frac{1}{2} \frac{(1 + n_{\lambda_1}^0) n_{\lambda_2}^0 n_{\lambda_3}^0}{n_{\lambda}^0} L_{+-} \right. \\
&\quad \left. + \frac{1}{2} \frac{(1 + n_{\lambda_1}^0)(1 + n_{\lambda_2}^0) n_{\lambda_3}^0}{n_{\lambda}^0} L_{++} \right) \\
&= n'_{\lambda} (\tau_{3,\lambda}^{-1} + \tau_{4,\lambda}^{-1})
\end{aligned} \tag{2.85}$$

Therefore the scattering rate referring to SMRTA is :

$$\tau^{-1} = \tau_{3,\lambda}^{-1} + \tau_{4,\lambda}^{-1} \tag{2.86}$$

Where we have used and defined the relaxation time to be :

$$\tau^{-1} = \frac{1}{n} \frac{\partial N}{\partial t} \tag{2.87}$$

From here we see that the phonon lifetime (τ) is inversely proportional to the phonon width, or the phonon scattering rate is proportional to the phonon width. Where upon simplifying $\tau_{3,\lambda}^{-1}$ in the Klemens approximation, the second term in parenthesis is zero since $n_1 = n_2$, and in the first term $n_1 + n_2 = 2n$, and therefore we can relate phonon width to the phonon lifetime.

2.3.7 Thermal Expansion Effect

As mentioned before, in the picture of non-interacting phonons in a perfect harmonic crystal, the equilibrium size is out of the picture. Therefore, the normal

modes of vibration are independent on the thermal expansion of the crystal. One can see this from the harmonic part of the crystal potential [41]:

$$U^{har} = U^{equ} + \frac{1}{2} \sum_{R,R'} u(R)D(R - R')u(R') \quad (2.88)$$

Where :

$$D_{\mu_1 \dots \mu_n}^{(n)}(R_1 \dots R_n) = \frac{\partial^n U}{\partial u_{\mu_1}(R_1) \dots \partial u_{\mu_n}(R_n)} \Big|_{u=0} \quad (2.89)$$

So applying a change in the displacement ($u(R) = \epsilon R + \bar{u}(\bar{R})$, with $r(R) = \bar{R} + \bar{u}(\bar{R})$, and $\bar{R} = (1 + \epsilon)R$), and inserting this change into the expansion of the potential energy around the new equilibrium position, we get:

$$U^{eq} + \frac{1}{2} \epsilon^2 \sum_{R,R'} RD(R - R')R' + \frac{1}{2} \sum_{R,R'} \bar{u}(R)D(R - R')\bar{u}(R') \quad (2.90)$$

Which leaves the potential unchanged after substituting $\bar{u}(R)$ with its equivalent. From here we can see that the potential is unchanged with changing the volume, which mean that the normal mode frequencies are the same with volume change. The thermal expansion term first appeared in equation (2.66) upon applying the anharmonic term to the first three lowest orders of the real part of the phonon self energy, and this term is evaluated to be:

$$\Delta^{(0)} = w_0 * e^{-\gamma \int_0^\infty [3\alpha]dT} \quad (2.91)$$

Where γ is the Gruneisen parameter of the selected optical mode. By definition, the Gruneisen parameter is a dimensionless parameter that describes the effect of changing the volume of the material on its vibrational modes. Also, α is the linear thermal expansion coefficient. From here, we can obtain the full design of the fitting equations of the frequency and linewidth needed to analyse our peaks from the Raman spectra of ZnO nanoparticles.

2.3.8 Life-time of Optical Phonons

In Klemens' thoughts to gain more information about anharmonicity, he discussed the three-phonon interaction process and compared his theoretical results to the present experimental results on Si done by J. H. Parker and D. W. Feldman [42]. In our work, we track the effects of the cubic part of the lattice potential, which is non-linear in the force. Therefore, there is anharmonicity in the lattice forces, that lead an optical mode to decay into other modes, thereby interchanging energy and maintaining thermal equilibrium. In this aspect, the optical phonon resembles the acoustic phonon. As we know that an optical phonon contributes

with a negligible amount to heat conduction (mainly because of their short lifetimes and small group velocities, as can be seen from the slope of the curve of (w vs k), the relaxation time of optical phonon does contribute to thermal conductivity, especially in low dimensional materials. Therefore, a clear conceptual insight into the laws and models governing and affecting the relaxation time of the optical phonons must be done. In his approach, Klemens used the perturbative calculation in the Hamiltonian. He calculated the lifetime of optical phonon at zero temperature, and developed his equation to calculate the lifetime at any temperature T . For this he relates the width of the phonon peak to the lifetime of the optical phonon.

The Perturbation Calculation

We consider an optical phonon at the center of the Brillouin zone with $k = 0$, and intrinsic frequency w_0 . This optical phonon interacts via anharmonic three-phonon process with two acoustical phonons with opposite momentum, but same magnitude. We ensure on momentum conservation by:

$$k = k' + k'' = 0 \quad (2.92)$$

And on energy conservation:

$$w_0 = w' + w'' \quad (2.93)$$

When writing the perturbation Hamiltonian, we include a strength term for the cubic anharmonic process as follows:

$$H' = \sum_{k,k',k'',x} \frac{1}{G} e^{i(k-k'-k'')x} c(k, k', k'') \times a(k) \times a^\dagger(k') \times a^\dagger(k'') \quad (2.94)$$

Where $x = \frac{\hbar w}{kT}$ and $c(k, k', k'')$ is related to cubic anharmonicity, where also a^\dagger and a are the phonon creation and annihilation operators respectively, and G is the number of atoms.

As a result of this decay channel, the phonon N population of a specific mode is changed:

$$t \frac{dN}{dt} = \sum_{j',j'',k'} \frac{c^2 \hbar^3}{M^3 w w' w''} \frac{1 - \cos(\Delta w t)}{\hbar^2 \Delta w^2} \times [(N + 1)N'N'' - N(N' + 1)(N'' + 1)] \quad (2.95)$$

Here (j', j'') are the polarizations of the modes (k', k'') which are longitudinal or transverse, also $\Delta w = w_0 - w' - w''$. The terms in brackets comes from the Fermi golden rule of three phonon process (See section "Fermi Golden Rule of Three and Four Phonon Processes"). Taking $N = N^0 + n$ the second term in the above equation; at zero temperature, reduces to $-n$. The term :

$$\int \frac{1 - \cos(\Delta w t)}{\Delta w^2} d(\Delta w) = \pi t \quad (2.96)$$

Snatches contributions from $\Delta w = 0$. Also

$$\Delta w = w - (1 + \alpha)vk' \quad (2.97)$$

Where αv is the velocity of k'' and v is the velocity of k' . When both vectors belong to the same polarization branch ($\alpha = 1$), we can consider ($w' > w''$), and we shall adopt it. Back to the summation on the various types of polarization ($\sum_{j',j''}$) of the modes (k', k''), we find that there are 6 types of different combinations of polarization (knowing that the transverse type is double degenerate) for the 2 modes. Not all these combinations obey energy conservation, it is ($\sum_{j',j''} = J$) where J is a number between 1 and 6.

The relaxation time τ is defined to be :

$$\frac{1}{\tau} = \frac{-1}{n} \frac{dN}{dt} \quad (2.98)$$

In the expression of ($\frac{dN}{dt}$), we have ($\sum_{k'}$) which can be transformed to an integral:

$$\sum_{k'} = \frac{V}{(2\pi)^3} \int d^3k' = \frac{Ga^3}{(2\pi)^3} 4\pi \int (k')^2 dk' \quad (2.99)$$

Here V is the total volume of the crystal, while a^3 is the volume per atom. We do some changes that eases our work in the integral such that, ($\frac{d\Delta w}{dk'} = -2v$), and ($w' = w'' = w_0/2$), using this simplifications we obtain :

$$\frac{1}{\tau} = \frac{J}{32\pi} \frac{\hbar w_0}{M^3} \frac{g^2 G a^3 w_0^2}{v^3} w_0 \quad (2.100)$$

The new parameter g contains the anharmonic cubic term $c(k, k', k'')$ such that $c(k, k', k'') = gw w' w''$. This result serves zero temperature value. One piece is still missing, which is the value of the the cubic anharmonic term $c(k, k', k'')$, or the term g . We can use one of the available results, in terms of the Gruneisen's parameter γ (this parameter measure the effect of changing the volume of a crystal, on its vibrational properties):

$$c(k, k', k'') = -\frac{i}{\sqrt{G}} \gamma \frac{2M}{\sqrt{3}} \frac{1}{v} w w' w'' \quad (2.101)$$

Therefore the equation of the inverse of the life-time of the optical phonon changes to :

$$\frac{1}{\tau} = w_0 \frac{J}{24\pi} \gamma^2 \frac{\hbar w_0}{M v^2} \frac{a^3 w_0^3}{v^3} \quad (2.102)$$

Further simplification can be done, we can take the Debye frequency of the monatomic lattice, which is only an approximation,

$$\frac{a^3 w_0^3}{v^3} = a^3 k_D^3 = \frac{3}{4\pi} (2\pi)^3 \approx 60 \quad (2.103)$$

k_D is the Debye wave number, also by taking $\gamma=2$ and the polarization type $J=1$, we get:

$$\frac{1}{\tau} = \frac{60 \times 4}{24\pi} w_0 \frac{\hbar w_0}{Mv^2} = 3w_0 \frac{\hbar w_0}{Mv^2} \quad (2.104)$$

After submitting some parameters with their actual values we get:

$$\frac{1}{\tau} = 0.06w_0 \quad (2.105)$$

Unfortunately the above equation failed to predict the line-width of the Raman peak of Si from the work done by Parker and Feldman [43]. The equation showed broader lines from what obtained from the experiment.

The Interaction Hamiltonian

The problem is in the cubic anharmonic term, and therefore we must reconsider our choice of the interaction Hamiltonian, and derive it again. The unperturbed Hamiltonian is:

$$H_0 = \frac{1}{G} \sum_{x,k,k'} Mww' e^{i(k-k')x} a(k) a^\dagger(k') \quad (2.106)$$

Which is functional for $k = k'$. Note that an expansion can change w to $w(1-\gamma\Delta)$, or if it is space dependent, it can be taken into account in the summation of the Hamiltonian among x , such that :

$$H' = \frac{1}{G} \sum_{k,k'} 2Mww' a(k) a^\dagger(k') \sum_x \Delta(x) e^{i(k-k') \cdot x} \quad (2.107)$$

The previous treatment for deriving the term $c(k, k', k'')$ is for some specific features of the wave vector k and its strain, where k must be long, so that its strain varies slowly, whereas the wave vectors k, k' are somehow equal. In the other hand, equation (2.98) was used in the region where the strain is not varying slowly, therefore it is no longer valid.

In our case the strain of the optical phonon is $(w/v)a(k)$, which has the sign of the first wave k in (w/v) , and we note here that the 2 vectors; although they have the same frequency, but they move in opposite directions, therefore the use of uniform strain theory is not valid.

In the current derivation, we consider the energy,

$$M(w')^2 a^\dagger(k') a(k') \quad (2.108)$$

Which is as obvious from the creation and annihilation operators, is related to the mode k' . After that, we force a static strain correlated to the first wave mode k , the optical mode. This change happens to change the energy by the following amount:

$$2Mw' \delta w' a^\dagger(k') a(k') \quad (2.109)$$

We now equate this change to the cubic anharmonic term multiplied by $a(k = 0)a(-k')a(k')$, therefore:

$$c(k, k', -k')a(k) = 2Mw'\delta w' \quad (2.110)$$

The term $\delta w'$ can be derived for the same strain as the first wave.

In his model to calculate $\delta w'$, Klemens thought of alternating force constants to link a linear chain of atoms. Because of anharmonicity of the optical mode, the force constants are perturbed, and this perturbation changes the sign from linkage to linkage. In this calculation we consider $w' = w_0/2$. For the mentioned linear chain, the frequency of the lattice wave of wave vector k is :

$$w^2 = \frac{\alpha + \beta}{M} \pm \left[\frac{(\alpha + \beta)^2}{M^2} - \frac{4\alpha\beta}{M^2} \sin^2(ka) \right]^{\frac{1}{2}} \quad (2.111)$$

Where all has the same mass, with constant distance between each other, and harmonic force constants α and β . When we use the wave vector of the optical mode ($k = 0$) we get:

$$w_0^2 = 2\frac{\alpha + \beta}{M} \quad (2.112)$$

For the branch where k is small, the acoustical branch:

$$\frac{2\alpha\beta}{(\alpha + \beta)M} \sin^2(ka) \quad (2.113)$$

While when $\sin(ka) = 1$:

$$w^2 = 2\alpha/m \quad \text{or} \quad 2\beta/M \quad (2.114)$$

Upon choosing the different direction of the strain ϵ of the two types of links α and β we get:

$$\begin{aligned} \alpha &= \alpha_0(1 + 2\gamma\epsilon) \\ \beta &= \beta_0(1 - 2\gamma\epsilon) \end{aligned} \quad (2.115)$$

Now substituting what we obtained in (2.111), and using the frequency (2.112) for the optical phonon, we can find the energy change that empowers us to obtain the c or g terms, considering the changes in the lattice forces α and β we find $\delta w'$ to be :

$$\frac{\delta(w')^2}{w'^2} = \frac{4}{3} \frac{\alpha + \beta}{\alpha - \beta} \cdot \gamma\epsilon \quad (2.116)$$

The values of the life times calculated before are reduced by the square of the factor :

$$\frac{2}{\sqrt{3}} \frac{\alpha - \beta}{\alpha + \beta} \quad (2.117)$$

After some simplifications, the lifetime for silicon, like in conditions used to determine it as before ($T = 0$), we obtain :

$$\frac{1}{\tau} = 0.007w_0 \quad (2.118)$$

Temperature Dependence of Phonon Rates

To generalize this relaxation rate, to be used for temperature T , the rate at $T = 0$ is multiplied by the factor :

$$1 + \frac{2}{e^{\frac{\hbar w_0}{2kT}} - 1} \quad (2.119)$$

Now, and by adopting Klemen's model for three phonon decay mechanisms, we can reach the final form of the equations governing the frequency and width change of phonons due to anharmonicity:

$$\begin{aligned} w(w_0, T) = & w_0 + \Delta^{(0)} + A \left[1 + \frac{2}{e^{\frac{\hbar w_0}{2kT}} - 1} \right] \\ & + B \left[1 + \frac{3}{e^{\frac{\hbar w_0}{3kT}} - 1} + \frac{3}{(e^{\frac{\hbar w_0}{3kT}} - 1)^2} \right] \end{aligned} \quad (2.120)$$

$$\begin{aligned} \Gamma(w_0, T) = & \Gamma_0 + A \left[1 + \frac{2}{e^{\frac{\hbar w_0}{2kT}} - 1} \right] \\ & + B \left[1 + \frac{3}{e^{\frac{\hbar w_0}{3kT}} - 1} + \frac{3}{(e^{\frac{\hbar w_0}{3kT}} - 1)^2} \right] \end{aligned} \quad (2.121)$$

These are the famous fitting equations used in many experiments and paper to fit experimental data, whether by combining the occupation number of phonon when using Kleme's mode, or by splitting them.

2.3.9 Temperature Dependence of The E_2^{high} Mode

The study of the temperature dependence of the E_2^{High} mode was done in the temperature range 80-750K, according to [34], and is compared to theory using the above-mentioned derivation of the frequency shift and width change, when cubic anharmonicities were applied to the second order in perturbation theory to the imaginary part of the phonon self energy . As temperature increases, the intensity of the E_2 peak decreases, with an increase in its line-width and decrease in the frequency. The below figure shows the dependence of the frequency and FWHM on temperature.

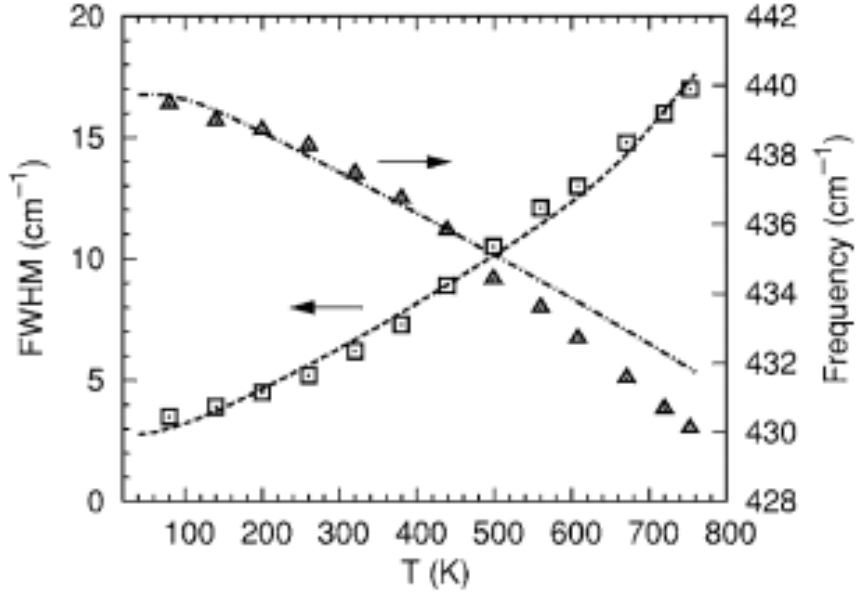


Figure 2.18: . Temperature dependence of the linewidth (squares), left axis and frequency (triangles), right axis of the E2 high mode. The dashed line is a fit of the model discussed in the text to the linewidth data. The dot-dashed line corresponds to the temperature dependence of the frequency given by the model for the same set of parameters.

[34]

2.3.10 Temperature Dependence of $A_1(LO)$ and $E_1(LO)$ Modes Using The Ridley channel model

A simpler model can be used to analyze the temperature dependence of this two modes, where their frequencies lies in a region of high density of states in the two phonon DOS. Therefore, the contributions from the self energy terms can be neglected. From the dispersion relations, its found that the generalized Ridley channel suits the phonon decay of these modes, where a longitudinal optical phonon decays into transverse acoustic branches and transverse optical branch. The suggested decay channel for $A_1(LO)$ mode is to $455cm^{-1}$ branch in the TO region and into $120cm^{-1}$ in the TA region at the $L - M$ points. For the $E_1(LO)$ mode, we assume the decay of phonon to $490cm^{-1}$ from the TO branch and $100cm^{-1}$ from the TA branch. For the fitting graphs of the FWHM and frequency change, the following equations were used:

$$\Gamma(T) = \Gamma_0 + A[1 + n_1(w_1, T) + n_2(w_2, T)] \quad (2.122)$$

$$w(T) = w_0 + \Delta_0(T) + B[1 + n_1(w_1, T) + n_2(w_2, T)] \quad (2.123)$$

In the first equation, Γ_0 represents the intrinsic FWHM from the impurity and/or defect scattering, $n(w, T)$ are the Bose-Einstein distribution functions. In the second equation, w_0 is the intrinsic frequency of the mode, and $\Delta_0(T)$ is the thermal expansion shift. We observe mode softening of $A_1(LO)$, with increase in FWHM as temperature increases. The fitting parameters give $\Gamma_0 = 1.3cm^{-1}$, $A=3.7cm^{-1}$, $B=-2.1cm^{-1}$ and $w_0 = 581.4cm^{-1}$. A similar behaviour in the frequency shift and FWHM increase is shown by the $E_1(LO)$ mode, where the fitting parameters are: $\Gamma_0 = 2.8cm^{-1}$, $A=3.3cm^{-1}$, $B=-1.7cm^{-1}$ and $w_0 = 595cm^{-1}$.

2.4 Phonon Confinement Model In Raman Spectroscopy For Nano-Materials

One extra feature that can be determined by Raman spectroscopy is to observe phonon confinement in small nano-particles (below 6nm). It is known that in 1981; a group of physicists, which are H. Richter, Z.P. Wang, and L. Ley, introduced a kind of a model that accounts for the red shift and broadening of the one phonon Raman spectrum of nano-structured silicon films [44]. The core of their model was the relaxation in the conservation of q -vector, which allowed phonons other than zone center ones to contribute to Raman spectrum.

Back in 1979, Morhange *et al.* studied Raman spectrum for Si wafers produced previously by ion bombardment, and observed a frequency shift of magnitude $7cm^{-1}$ (from $522cm^{-1}$ to $515cm^{-1}$), and total full width at half maximum (FWHM) of magnitude $8cm^{-1}$ [45]. Extended by the work of Tsu *et al.*, who observed Raman lines for Si films in the range from $512cm^{-1}$ to $476cm^{-1}$, and concluded line-width increase accompanied with a red-shift [46]. They thought that their results were the first signs of crystallization of the Si films, their thoughts were aided by the work of Iqbal *et al.*, which obtained similar spectrum for polycrystalline Si [47].

To account for the Raman line-position and line-width changes, the model considers that the phonons are confined in the nano-structure and only in it. For this let us consider an infinite crystal having a phonon of wave vector q_0 , therefore the wave function of the phonon is :

$$\phi(\vec{q}_0, \vec{r}) = u(\vec{q}_0, \vec{r})e^{-i\vec{q}_0 \cdot \vec{r}} \quad (2.124)$$

Where here $u(\vec{q}_0, \vec{r})$ hold the periodicity of the lattice. With the assumption of the localization of the phonon in the crystallite, which is a sphere with diameter L , this imposes to introduce a new wave function for the phonon restricting it to the sphere :

$$\begin{aligned} \psi(\vec{q}_0, \vec{r}) &= A \exp\left(\frac{-r^2/2}{(L/2)^2}\right) \phi(\vec{q}_0, \vec{r}) \\ &= \psi'(\vec{q}_0, \vec{r})u(\vec{q}_0, \vec{r}) \end{aligned} \quad (2.125)$$

With

$$|\psi|^2 = A^2 \exp\left(\frac{-r^2}{(L/2)^2}\right) \quad (2.126)$$

and

$$\psi'(\vec{q}_0, \vec{r}) = A \exp\left(\frac{-r^2/2}{(L/2)^2}\right) e^{-i\vec{q}_0 \vec{r}} \quad (2.127)$$

This Gaussian distribution localizes the new phonon wave function ψ to a radius $|r| \leq L$ and width $\sqrt{\ln 2}L$. For us to calculate the Raman spectrum, we need to expand ψ' in a Fourier series:

$$\psi'(\vec{q}_0, \vec{r}) = \int d^3q C(\vec{q}_0, \vec{q}) e^{i\vec{q}\vec{r}} \quad (2.128)$$

Where $C(\vec{q}_0, \vec{q})$ is a Fourier coefficient given in the form:

$$C(\vec{q}_0, \vec{q}) = \frac{1}{(2\pi)^3} \int d^3r \psi'(\vec{q}_0, \vec{r}) e^{-i\vec{q}\vec{r}} \quad (2.129)$$

Inserting equation (2.127) to $C(\vec{q}_0, \vec{q})$ in the above equation we get :

$$C(\vec{q}_0, \vec{q}) = \frac{AL}{(2\pi)^{\frac{3}{2}}} \exp\left(\frac{-1}{2} \frac{L^2}{2} (\vec{q} - \vec{q}_0)^2\right) \quad (2.130)$$

Therefore we have abandoned the old representation $\phi(q_0, r)$ of phonons, and created the new phonon wave functions ψ and ψ' , to be the superposition of wave functions having wave vector q in the region $|\vec{q}_0 - \vec{q}| \leq \frac{1}{2L}$ centered at q_0 .

For this particular choice of localization, where we weighted the eigenfunctions by $C(q_0, q)$, as we said before, the illuminating idea of this model is created because of the relaxation of Δq , so that the phonon is localized in the small spherical nano-particle, therefore the phonon transition matrix has non-vanishing terms also for values of $q \neq 0$, and:

$$| \langle \vec{q}_0 | \hat{O} | \vec{q} \rangle |^2 = | \langle \vec{q}_0 | \hat{O} | \vec{q}_0 \rangle |^2 \cdot C(\vec{q}_0, \vec{q})^2 \quad (2.131)$$

Here \hat{O} is the photon-phonon interaction operator. Therefore, and upon handling the excitation of the zone-center optical phonons ($q = 0$), we allowed the contribution from phonons having wave vector $q \neq 0$, this has a direct impact on the energies and frequencies of the Raman spectrum, because it allows phonons rather than the zone-center ones to exchange energy with the photons. The new energies are determined by the dispersion $w(q)$. Furthermore, away from zone-center, the optical phonon dispersion is degenerate, and this degeneracy is because of the two polarization branches; the transverse and longitudinal branches, and both have negative dispersion. In a nutshell, because of this added transitions from $q \neq 0$, it is clear now the causes of the broadening in line-width (Γ_1) and the frequency shift (Δw) in the Raman spectrum. The new changes among the

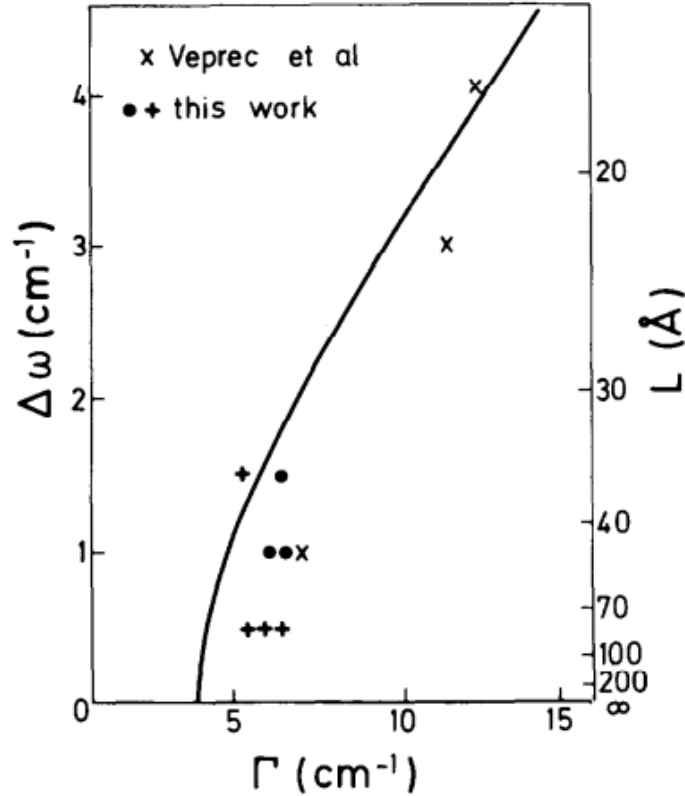


Figure 2.19: Relation between the frequency shift and line-width in Raman line

frequency and line-width are connected via $w(q)$; the dispersion relation, and the coefficient $C(\vec{q}_0, 0)$ in equation (2.130) see Figure (2.19).

Where in this graph, Γ is the summation of the intrinsic line-width Γ_0 and the added one due to phonon confinement Γ_1 (from the contribution of $q \neq 0$ phonons). The right-side ordinate have information about the crystallite size in Angstrom, this parameter is of major importance due to its appearance in the equation (2.130), thus it is a crucial element in calculating the coefficient $C(\vec{q}_0, \vec{q})$. As mentioned by Richter *et al.*, this numerical values are model dependent and therefore they are consistent with the longitudinal optical phonon branch in the direction Γ -X. Also figure (2.19) shows experimental data conducted from the work of Iqbal *et al.* of films prepared by plasma transport method. The experimental points are consistent with the graph linking the relationship between Γ and Δw upon taking advantage of an uncertainty ± 0.5 on both the frequency shift and line-width.

The Raman lines for micro-crystalline samples shows a sort of asymmetry manifested by the tailing toward lower frequencies as shown in figure (2.20), which is well accounted for in this model. The accumulated intensity and asymmetry is caused by the amorphous type of the material. We know that in Crystalline

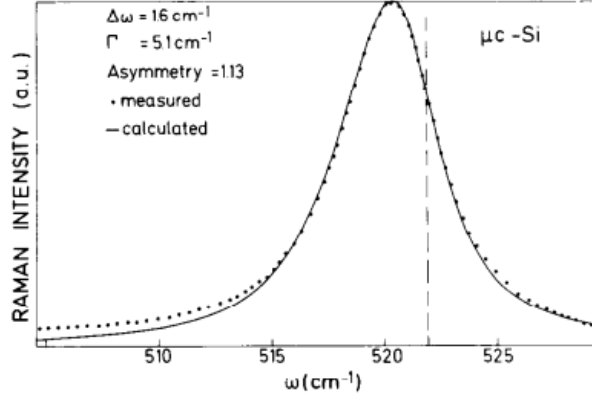


Figure 2.20: Measured and calculated Raman line for μc -Si sample. The solid line is calculated Raman intensity, while the dotted line is for measured intensity

materials, the zone-center optical phonons abide to the wave vector conservation rule. As we discussed above in the previous section " Life-Time of Optical Phonons", Klemens stated that the favorable decay channel for zone-center optical phonons is the creation of two acoustical phonons of equal and opposite wave vectors, so that their sum is equal to zero. The transition probability of the above-mentioned decay is:

$$\Gamma_0(w_0) \propto |M|^2 \cdot N(w') \cdot N(w'') \quad (2.132)$$

Where $w' = w'' = w_0/2$, $N(w)$ is the density of states of the acoustical phonons, and M is the transition matrix element. Upon working in micro-crystal structure, the model suggests the relaxation of the wave vector conservation law. Therefore equation (2.132) is adjusted to:

$$\Gamma_0(w_0) \propto |M|^2 \int F(\vec{q}_-, \vec{q}_+) N(w_0/2 - w') \cdot N(w_0/2 + w') dw' \quad (2.133)$$

This integral is bounded for a range of w' , which is done through the weighing function $F(\vec{q}_-, \vec{q}_+) = F(|\vec{q}(w_0/2 - w') - \vec{q}(w_0/2 + w')|)$, that is the weighing function is Guassian centered around $q(w_0/2)$, and has width Δq . One thing to note here is the intrinsic line-width (Γ_0), it is expected to increase whenever the averaged two-phonon density of states applied in equation (2.133) is greater than the actual two-phonon density of states. Therefore we describe this temperature dependence in Γ_0 as follows:

$$\Gamma^2(T) = \Gamma_0^2 \left(1 + \frac{2}{e^x - 1}\right)^2 + \Gamma_1^2 \quad (2.134)$$

Where Γ_1 is temperature independent term, and it has to deal with the size of the micro-crystal, and $x = \hbar w_0 / kT$.

In accordance to this, measurements were done on 4 samples annealed at different temperatures, in which four of them were micro-crystal Silicon and one is actual crystal Silicon. After that, a fit was done to obtain the intrinsic line-width (Γ_0) and (Γ_1). See Figure (2.21) and table (2.22).

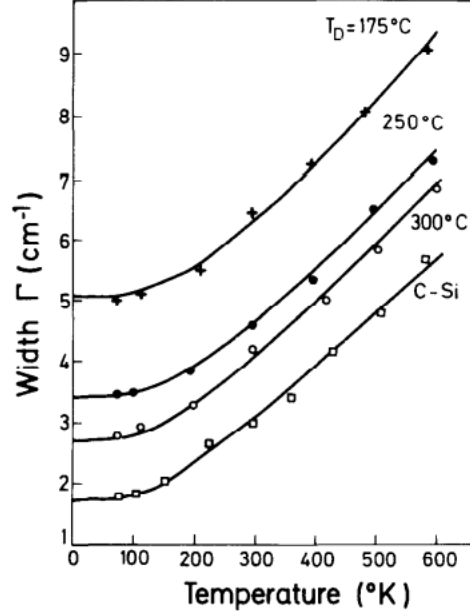


Figure 2.21: Raman line-width versus temperature of 3 $\mu\text{c-Si}$ samples and 1 c-Si sample. The solid lines are the fitted results

sample	Γ_1 (cm^{-1})	Γ_0 (cm^{-1})	$\frac{\Gamma_0}{\Gamma_0(\text{cryst})}$	L (\AA)
cryst. Si	0	1.7	1	∞
$\mu\text{c-Si}$, $T_D=300^\circ\text{C}$	1.8	2.0	1.18	100
$\mu\text{c-Si}$, $T_D=250^\circ\text{C}$	2.7	2.1	1.24	90
$\mu\text{c-Si}$, $T_D=175^\circ\text{C}$	4.4	2.5	1.47	80

Figure 2.22: The obtained line-width from fitting the temperature dependence line-width of 4 Si samples

In the table we have listed the values of Γ_0 and Γ_1 , where the Γ_0 was determined from the slope of the graph in figure (2.19) for large T part, and the latter is determined by taking the temperature $T \rightarrow 0$ in equation (2.134). As can be seen from the table, the values for Γ_0 increases with decreasing the crystallite's size, which is in good agreement with the phonon dispersion in Si.

Finally, we observe good agreement between the theoretical model concluded by Richter, and the experimental work on $\mu\text{c-Si}$. This lead us to conclude the effect caused by imposing relaxation on the wave vector selection rule which happens to be crucial in micro-crystalline Si.

Extending the work of Richter *et al.*, I.H. Campbell and P.M. Fauchet [48] wrote a paper discussing 2 new features of confinement. The first feature was established when they look after the form of confinement of Richter and found no physical reason for choosing the Gaussian weighting function. In their paper, they introduced new forms of weighting functions and compared the theoretical results with the measurements done by Iqbal *et al* [49]. The second feature was taken to test the frequency shift and line-width change for different shapes of the micro-crystalline to the best fit weighting function from feature 1. They started the paper with the same work of Richter *et al.* by expressing the wave function of a phonon in an infinite crystal material with the weighting function, that they named it $W(r, L)$. So for an infinite crystal, the phonon wave function is :

$$\phi(\vec{q}_0, \vec{r}) = u(\vec{q}_0, \vec{r}) e^{-i\vec{q}_0 \vec{r}} \quad (2.135)$$

When introducing the weighting function, the above equation transforms to:

$$\psi(q_0, r) = W(r, L)\phi(q_0, r) = \psi'(q_0, r)u(q_0, r) \quad (2.136)$$

Richter *et al.* [44], choose a Gaussian distribution of $W(r, L)$ with with phonon magnitude $1/e$ at the boundary. So that expanding ψ' in Fourier series we get:

$$\psi'(q_0, r) = \int d^3q C(q, q_0) e^{iqr} \quad (2.137)$$

with the Fourier coefficient $C(q, q_0)$:

$$C(q, q_0) = \frac{1}{(2\pi)^3} \int d^3r \psi'(q_0, r) e^{-iqr} \quad (2.138)$$

Therefore as it was concluded before, the new wave function is superposition of wave functions of wave vector $q \neq 0$ centered at $q_0 = 0$. The Fourier coefficient was in the paper by Richter:

$$|C(0, q)|^2 = e^{-\frac{q^2 L^2}{4}} \quad (2.139)$$

Where we assumed $q_0 = 0$. The first order Raman scattering is:

$$I(w) \simeq \int \frac{d^3q |C(0, q)|^2}{(w - w(q))^2 + (\Gamma_0/2)^2} \quad (2.140)$$

Where in this equation, Γ_0 is the intrinsic line-width, and $w(q)$ is the phonon dispersion relation. We take the limits of integration to cover a spherical Brillouin

zone, with the dispersion being independent on direction. Richter's model was consistent with the measured crystals that were spherical, but it was mistaken in predicting the micro-crystal size, which appears that his calculations were consistently low to 20 Angstroms from the measured values. Tiong *et al.* [48] tried to fit his results of his samples "Ion Implanted GaAs" through this model. To get good fitting results, one must change the amplitude at the boundary from $1/e$ to $\exp(-4\pi^2)$. Also to get a consistent theory for both Si and GaAs, this paper tried to test 3 different confinement models with different values at the boundary. The adjustment was played at the level of the weighting function. The three new used weighting functions are:

1. $\sin(\alpha r)/(\alpha r)$
2. $\exp(-\alpha r)$
3. $\exp(-\alpha r^2/L^2)$

The three weighting functions were chosen to make analogy with: The ground state of an electron in a hard sphere for the first function. Second, wave in a lossy medium, which is a medium that an electro-magnetic wave would lose energy in it as it propagates. Third, to account for all the distribution of micro-crystals. For the *sinc* function the value at the boundary was taken $\alpha = 2\pi/L$, so that it has zero value at the boundary. For the other two functions, the value is calculated once, because it changes the crystallite size. The data of Iqbal *et al.* [49] were used to compare the results obtained from these functions. The Fourier coefficients are as follow:

$$\begin{aligned}
|C(0, q)|^2 &\simeq \frac{\sin^2(qL/2)}{(4\pi^2 - q^2L^2)^2} & W(r, L) &= \frac{\sin(2\pi r/L)}{2\pi r/L} \\
|C(0, q)|^2 &\simeq \frac{1}{(16\pi^4 - q^2L^2)^4} & W(r, L) &= e^{-4\pi^2 r/L} \\
|C(0, q)|^2 &\simeq e^{-q^2L^2/16\pi^2} & W(r, L) &= e^{-8\pi^2 r^2/L^2} \quad (2.141)
\end{aligned}$$

We can see the comparison between the calculated results and the work done by Iqbal in the below figure. The left-ordinate of the figure shows the frequency shift (Δw) with respect to the intrinsic frequency of a crystal sample. The horizontal-ordinate is the line-width (FWHM), and the right-ordinate is the calculated length L of the micro-crystal. As shown from the results, the rapprochement between measured values and theoretical weighting functions is clearly seen for the Gaussian weighting function with the value of $\exp(-4\pi^2)$ at the boundary of the crystallite. Add to that, this choice of weighting function and its corresponding value at the boundary are in agreement with the measurements of Tiong *et al.* [50] for ion implementation in GaAs. From the value of $\exp(-4\pi^2)$, we can say that this type of confinement is rigid so the amplitude of the phonon at the boundary $\neq 0$.

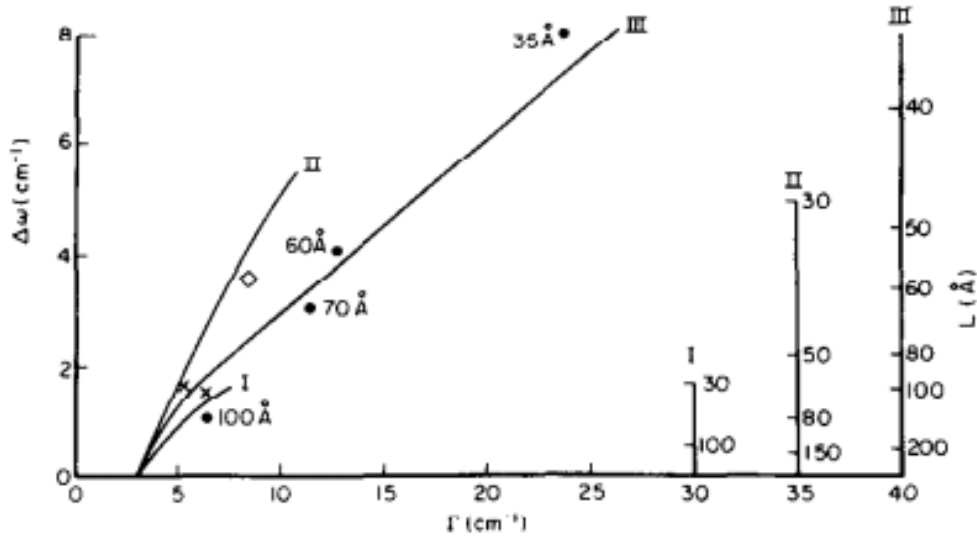


Figure 2.23: The calculated frequency shift and broadening for the micro-crystal structures using I. exponential II. Sinc III. Gaussian. The dots are from the work of Iqbal *et al*, the (X) are from the work of Richter *et al*, and the hollow rhombus is from the authors' work

After finishing this fitting criteria among the three different confinement functions, we selected the Gaussian weighting function with its corresponding value at the boundary to be used in the following feature of the phonon confinement model. Now we seek results from the Raman spectrum of various micro-crystal shapes, and their accordance to the confinement model with our specific choice of confinement function. The different shapes of the micro-crystals enters the calculations by adjusting the confinement function to take account of the magnitude and direction of the shape. The three shapes we will be dealing with are :

1. Sphere
2. Column shaped crystal
3. Thin film

See figure (2.24) for the shapes of micro-crystals.

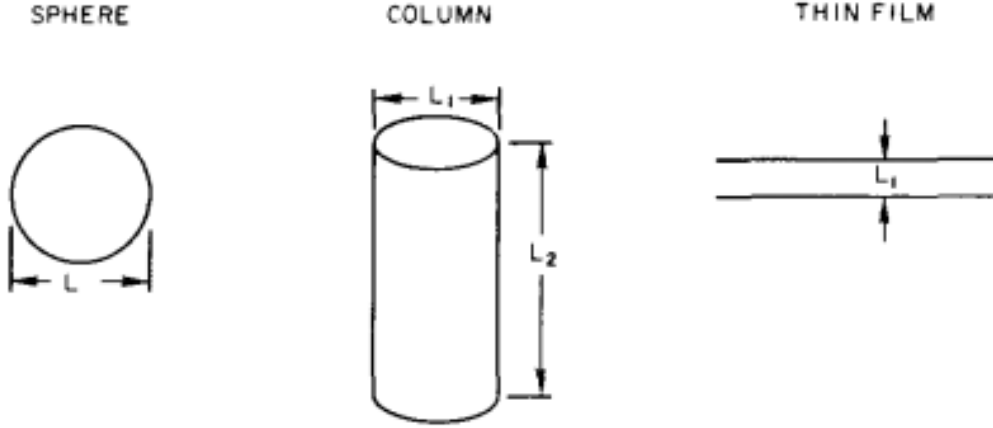


Figure 2.24: The three micro-crystals shapes. Length L_2 of the column is considered to be infinite.

The Fourier coefficients for the corresponding shapes are:

$$|C(0, q_1, q_2)|^2 \simeq e^{(-q_1^2 L_1^2)/(16\pi^2)} e^{(-q_2^2 L_2^2)/(16\pi^2)} \left| 1 - \operatorname{erf}\left(\frac{q_2 L_2}{\sqrt{32\pi}}\right) \right|^2 \quad \text{For Column}$$

$$|C(0, q_1^2)|^2 \simeq e^{(-q_1^2 L_1^2)/(16\pi^2)} \left| 1 - \operatorname{erf}\left(\frac{q_1 L_1}{\sqrt{32\pi}}\right) \right|^2 \quad \text{For Thin Film}$$

(2.142)

Now it is the time to observe the comparison between these 3 different shapes, knowing that this comparison empowers us to distinguish between the three, two and one dimensional effect on the Raman spectrum, see figure (2.25). The scales for the line-width and the frequency shift are the same for the three shapes, but the scale for the dimensions on the right-side ordinate differs from shape to shape, noting that for the column shape, only L_1 is displayed since L_2 is infinite. In addition to the experimental points in figure (??), the work from Murphy *et al.* on thin Silicon films samples prepared by thermal oxidation [51], is added. Note here that there is no experimental data for columns.

It can be concluded that this figure shows frequency shift and line-width increase for the measure and calculated Raman lines. The strength of the Raman lines goes in ascending order from thin film shaped micro-crystals, then column, and finally the strongest Raman lines are for the spheres. This is a direct cause from the sensitivity of Raman line to number of ordinates in micro-crystals, so that it is affected by crystallographic orientation of the different films. The confinement in thin films occur only in the Z direction, on the other hand, for column shaped micro-crystals the confinement is along X and Y directions, while for spheres, the confinement is in three directions X, Y, and Z. This distinction is made between Raman lines of thin films and for those of sphere shaped

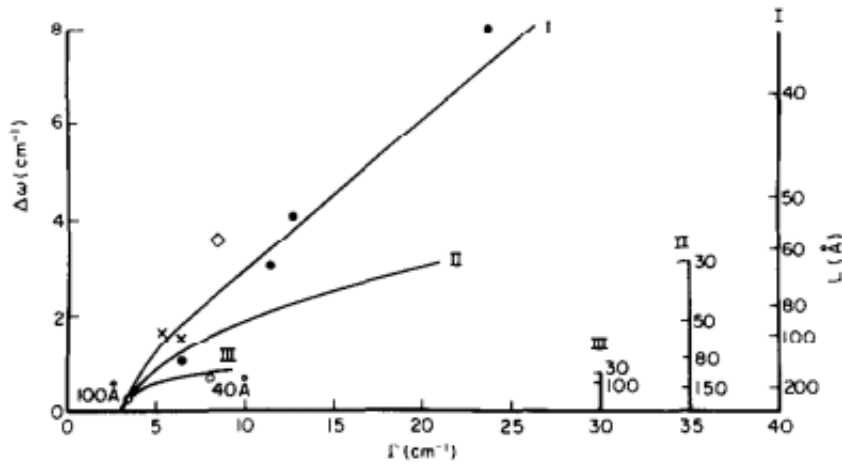


Figure 2.25: This graph displays the relation between the calculated frequency shift, broadening and crystal size of the three various shapes: I.Sphere II. Column III. Thin film. The experimental points are the same as figure (2.23) with the addition from the measurements of Murphy *et al.* displayed by hollow circles.

micro-crystals. Figure (2.26) shows the comparison between experimental and theoretical data from the work of Murphy *et al.* on Silicon thin films on sapphire (SOS). The length was of 40 Angstroms and the samples were made by thermal oxidation. The graph shows good agreement between the line-width and symmetry of the calculated and the experimental work.

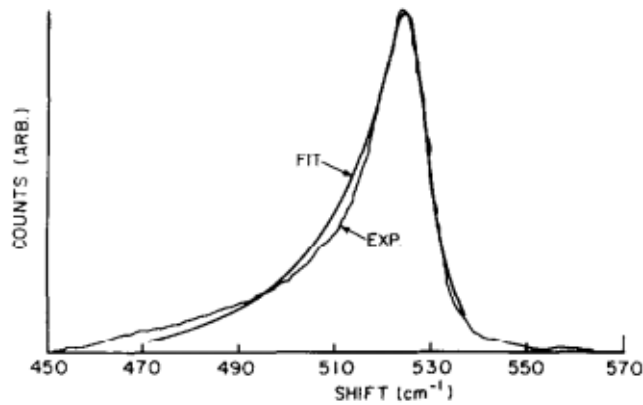


Figure 2.26: Experimental and theoretical spectra of 40 Angstroms thin film.

Lately, and in 2010, a paper proposed by Rodeenko *et al.* titled "Modified Phonon Confinement Model for Raman Spectroscopy of Nanostructured Materials" [52], looked after the details of the original "PCM" model, and improved some of its features. At first, it shed the light on the parameters in the Gaus-

sian weighting function, and showed the discrepancies in the weighting function proposed by Richter *et al.* Secondly, in the Richter-Campbell-Fauchet model, the medium was taken to be isotropic and the dispersion relation was of linear mode, this assumption was made because they considered that only a small region of the Brillouin zone contributed to the scattering process. Rodeenko's model insisted to deal with the anisotropy of the material, thus adjusting the phonon dispersion relation, because it showed that for low dimensional materials, the broadening is strongly affected by the anisotropy.

Chapter 3

Results and Discussion

In this chapter, we intend to use the model developed by Menedez and Klemens, to gain more information about the decaying processes and channels of zone-center optical phonon in ZnO, and thus to determine the intrinsic frequency and lifetime.

The peaks or as we know them, the vibrational modes of ZnO nano-particles were measured using Raman spectroscopy described in section 2 in the literature review. Then a heater was connected to do further measurements at high temperature and to track the various ZnO phonons' response to temperature. After that, a fitting is done using the fitting equations discussed in the literature review, this helped us to extract the intrinsic frequency and lifetime of the phonons, and gave us more information about their respective decaying processes.

3.1 Experiment

In our experiment we started by growing Zinc-Oxide nanoparticles using the following process. The synthesis of zinc oxide nanoparticles was carried out as follows: In the beginning a solution of zinc nitrate hexahydrate was prepared by dissolving 0.2 g of this compound in 10 mL of double distilled water heated at 80 degrees celsius. In a second step, the solution was kept under reflux for 1 hour at 80 degrees Celsius under continuous stirring (400 rpm). In this time, KOH solution ($C=0.2$ M) was made by dissolving 0.11 g of potassium . After reflux, KOH was added to the mixture drop by drop using a burette with constant stirring. Lastly, the obtained solution was centrifuged at 4000 rpm for 10 minutes and the precipitate was washed 3 times with double distilled water. The final solution was kept for 24 hours under freeze dryer to obtain the nanoparticles in form of powder.

The Raman line spectra were excited using Cobolt Samba laser of 532nm in wavelength. The scattered light was analyzed by the means of Acton SpectraPro (2500i) coupled to a charged -coupled device (CCD) detector. Finally, the heater

from HeatWave Labs (Model 101303 temperature controller) was connected to the sample holder.

3.2 First Order Raman Spectrum

As discussed in Section 2, ZnO has four main optical phonon modes with the following irreducible representation:

$$\Gamma_{optical} = A_1 + E_1 + 2E_2 + 2B_2 \quad (3.1)$$

In our work, we used unpolarized Raman spectrum, so that all the phonon modes with various symmetries can appear, this is because we are using unpolarized light source. The observed peak at 437cm^{-1} is attributed to the $z(xx)\bar{z}$ spectrum of $(E_2 + A_1)$ symmetry. This mode; named the E_2^{high} mode, shows a clear asymmetry toward lower frequencies as shown from the below spectrum. This asymmetry is understood from the anharmonic interactions concerned to this mode, discussed in details in the following section.

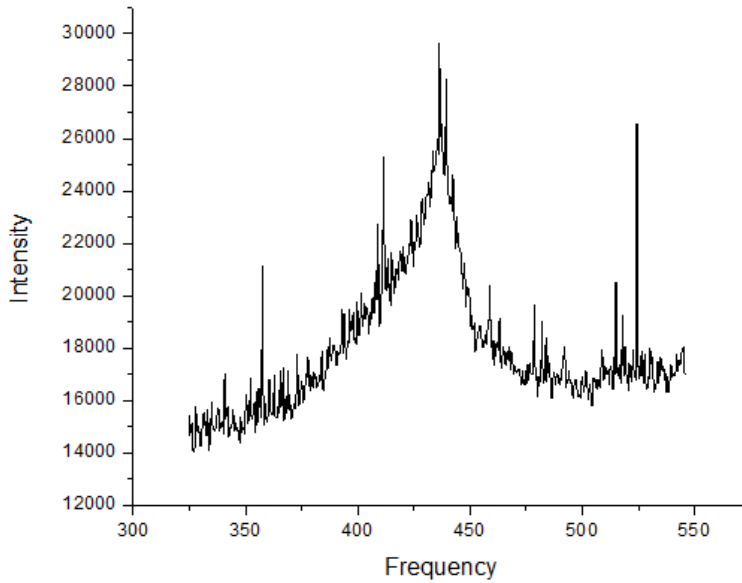


Figure 3.1: Raman Spectrum of E_2^{high} mode

One more peak can be seen at 410cm^{-1} that corresponds to $E_1(TO)$ mode of spectrum $x(zy)y$. An additional peak is detected at 387cm^{-1} , which is assigned to $A_1(TO)$ mode.

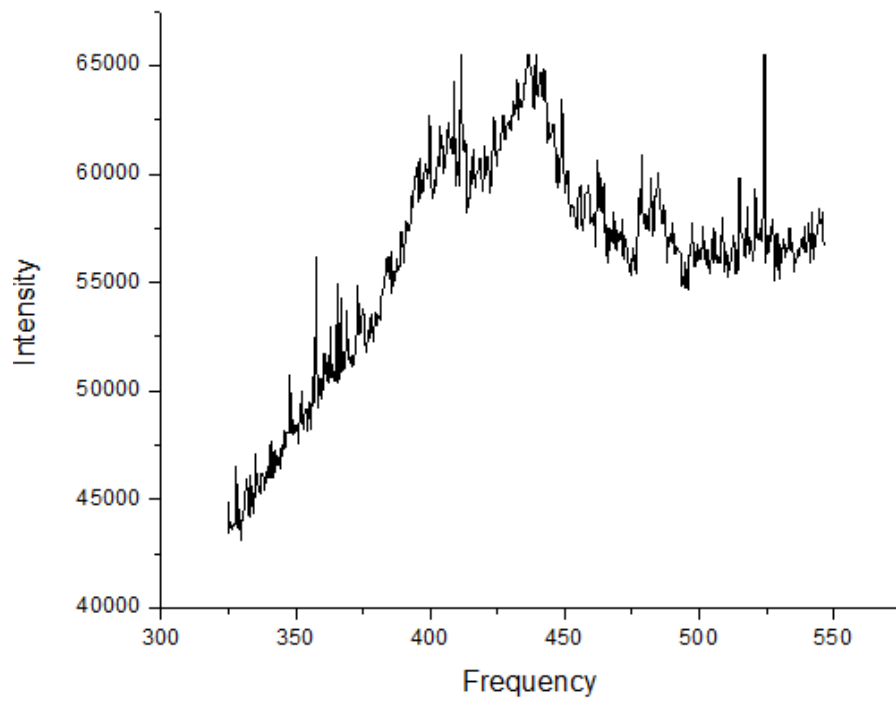


Figure 3.2: Raman Spectrum of $E_1(TO)$ mode

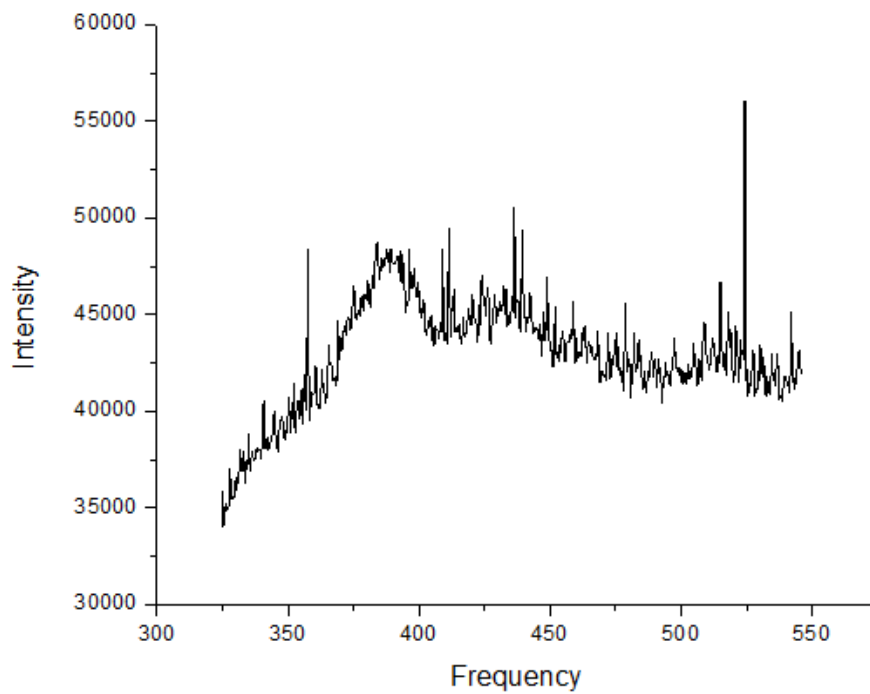


Figure 3.3: Raman Spectrum of $A_1(TO)$ mode

Furthermore, additional 2 peaks in the first order Raman spectrum are seen at 570cm^{-1} and 582cm^{-1} . This two peaks are assigned to $z(xx)\bar{z}$ and $x(zy)y$ spectra and meant to be the $A_1(LO)$ and $E_1(LO)$ modes respectively.

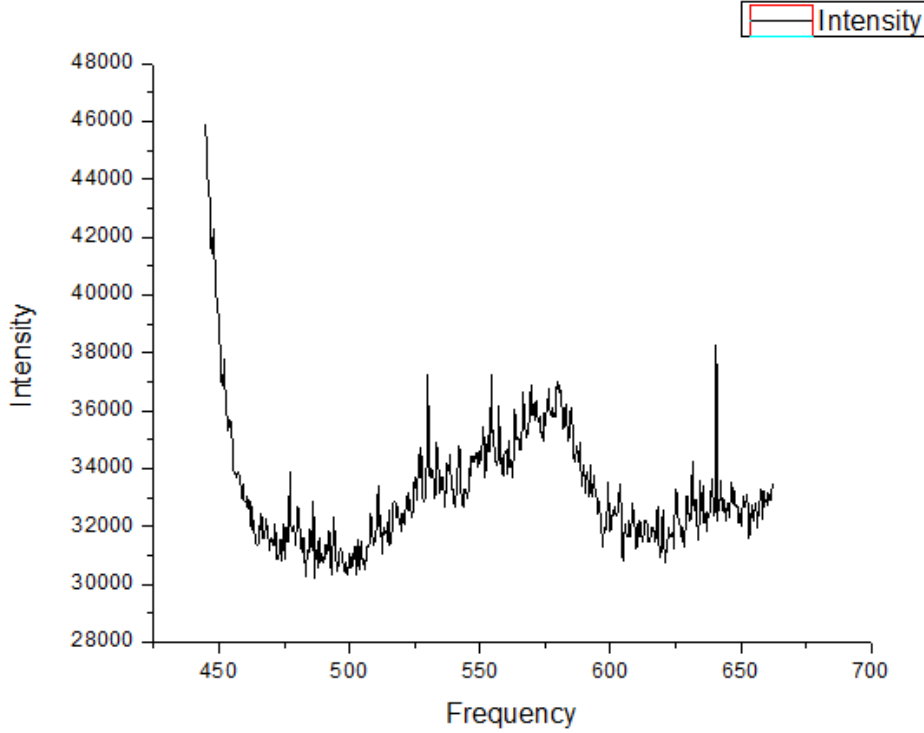


Figure 3.4: Raman Spectrum of $A_1(LO)$ and $E_1(LO)$ modes

To sum up this section, 5 First order Raman peaks of ZnO nano-particles were found at $383, 410, 437, 570, 582\text{ cm}^{-1}$.

3.3 Second order Raman Spectrum

The phonons involved in the first order Raman scattering are restricted to $\vec{k} = 0$ conservation rule. Whereas in the second order Raman spectrum, phonons from the entire Brillouin zone contribute to the spectrum. This is an outcome from the relaxation of the momentum conservation rule, due to very small nano-particles size (around 5nm) presented in the sample.

In the second order spectrum of ZnO phonons, we find a peak at 1160cm^{-1} that contains perturbation from $2E_1(LO)$ and $2A_1(LO)$, and it is found between the doubled frequency of $E_1(LO)$ and $A_1(LO)$. The peak just under it at 1102cm^{-1} , is attributed to $2LO$ mode at $H - K$. The mode at 1060cm^{-1}

is assigned to $TO + LO$ combinations at $M - L$ points. This three peaks are combined into one big peak as can be seen from the following figure:

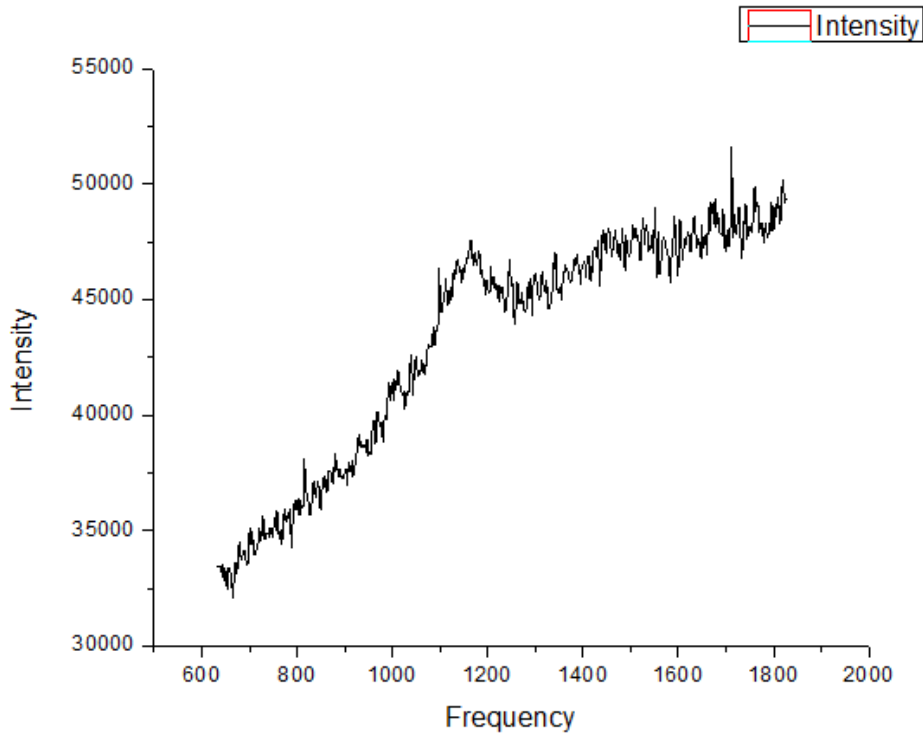


Figure 3.5: Raman Spectrum of 1060,1102 and 1160 cm^{-1} peaks

The peak at 333 cm^{-1} was previously assigned to TA overtone scattering occurring at M point, but from the paper "Temperature dependence of ZnO", they found that this mode is clearly a difference mode taking into account its behaviour with temperature. They compared its Raman intensity normalized to the intensity at room temperature versus temperature to the statistical occupation factor of $E_{2low} - E_{2high}$ modes, and found an agreement.

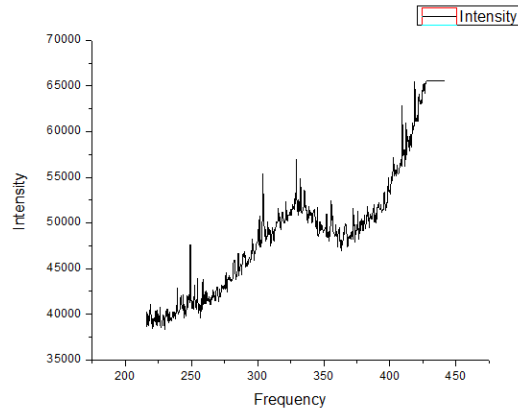


Figure 3.6: Raman Spectrum of 333cm^{-1}

A peak appears at 277 and is assigned to a difference mode ($B_{1high} - B_{1low}$), one more peak is seen at 197cm^{-1} , which has $A_1, (E_2)$ symmetry.

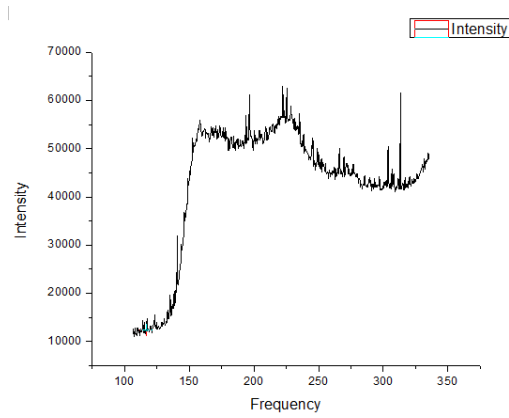


Figure 3.7: Raman Spectrum of 197cm^{-1} and 277cm^{-1} modes

A peak is seen at 478cm^{-1} that exhibits A_1 symmetry and is assigned to LA overtones along $M - K$, which is seen from the figure (3.4). The peak at 530 has A_1 symmetry and is attributed to LA overtones along $L - M - H$, and can be seen from the figure (3.4). The $TA + LO$ combinations arise the doublet observed at $654-666$. The 654 peak has $E_2 + E_1$ symmetry, while the symmetry of the 666 peak is A_1 at M point.

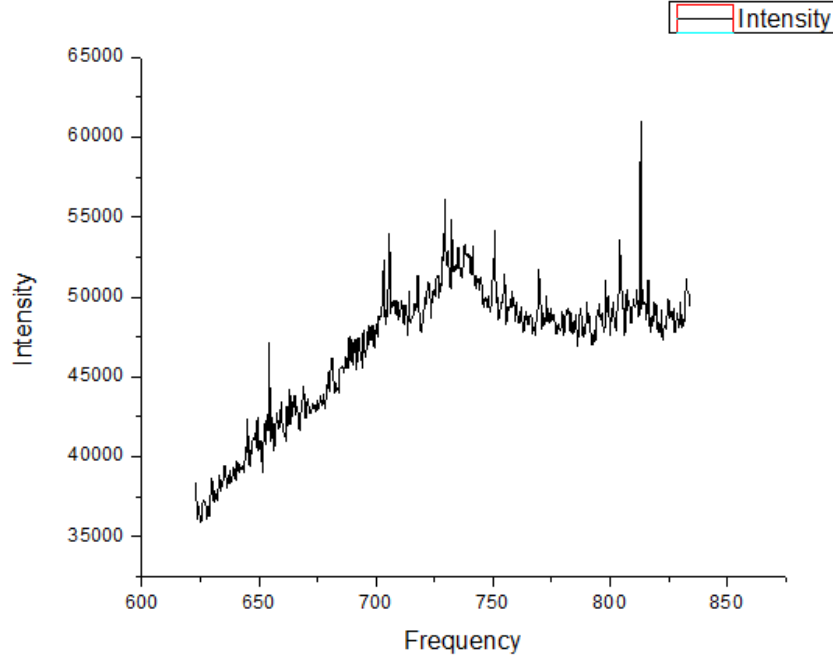


Figure 3.8: Raman Spectrum of $654,666\text{cm}^{-1}$

Low intensity modes are detected at 704cm^{-1} and 732cm^{-1} having A_1 symmetry and are attributed to acoustic and longitudinal combinations. We summed up our results of second order Raman peaks in the following table:

Frequency	Symmetry	Brillouin zone points
197	$A_1, (E_2)$	L,M,H; Γ
277	A_1	Γ
333	$A_1(E_2, E_1)$	Γ
478	A_1	M-K
530	A_1	$\Gamma; L, M, H$
654	E_1, E_2	L,H
666	A_1	M
704	A_1	M
732	A_1	L,M
1060	A_1	M-L
1102	A_1	H-K
1160	$2A_1(LO), 2E_1(LO); 2LO$	$\Gamma; A - L - M$

Table 3.1: Second order Raman peaks, and their associated symmetry and position in the Brillouin zone.

3.4 Asymmetry of E_2^{high} Mode

The E_2^{high} phonon mode shows a clear asymmetry toward lower frequencies. This asymmetry is a direct consequence of the anharmonicity effects, that is the renormalization of the bare harmonic frequency of this mode, that manipulates the components of its phonon self energy. The effect of the cubic anharmonicity to the second order in perturbation theory on the imaginary part of the phonon self energy is :

$$\Gamma(w) = \frac{18\pi}{\hbar^2} \sum_{q,j_1,j_2} |V_3(qj_1, -qj_2)|^2 [(n_1 + n_2 + 1)\delta(w_1 + w_2 - w) + (n_2 - n_1)\delta(w_1 - w_2 - w)] \quad (3.2)$$

The expansion of the lattice potential to third order gives the $V_3(qj_1, -qj_2)$ term . The phonon occupation number of the modes $w(q, j_1)$ and $w(-q, j_2)$ is represented by n_1 and n_2 respectively, where q is the phonon wave vector and j is the phonon branch. For simplification, an assumption was taken here that considers a slowly varying Bose-Einstein factors and V_3 in a small energy range. From the above we found :

$$\Gamma(w) = |V_3^+|^2(1 + n_1 + n_2)\rho^+(w) + |V_3^-|^2(n_2 - n_1)\rho^-(w) \quad (3.3)$$

The above equation has new components. We observe the split of the third order lattice potential coefficient into anharmonic constants describing the decay into phonon sums and differences. Also there are the two-phonon DOS, where $\rho^+(w)$ is the two-phonon sum DOS, and $\rho^-(w)$ is the two phonon difference DOS. The triumph here is in the two-phonon sum and difference DOS. We get the real part of the phonon self energy from Kramers-Kronig relation that relates the imaginary part with the real part:

$$\Delta(w) = -\frac{2}{\pi}P \int_0^\infty \frac{w'}{w'^2 - w^2} \Gamma(w') dw' \quad (3.4)$$

Now we can see the frequency dependent renormalization in the phonon self-energy of the intrinsic frequency. Another player in the mode softening and the asymmetric shape of the E_2^{high} mode is the frequency shift due to thermal expansion of the lattice. Its effect can be taken to be :

$$\Delta_0 = -w_0\gamma \int_0^T [\alpha_c(T') + 2\alpha_a(T')] dT' \quad (3.5)$$

Where α_c and α_a are the thermal expansion coefficients along parallel and perpendicular directions of the lattice. Here γ is the Gruneisen parameter which is taken to be 2.02. This parameter relates the thermal expansion of the lattice to

its vibrational modes. The values of the thermal expansion coefficients and the Gruneisen parameter were taken from [53], and they were found to be increasing with temperature:

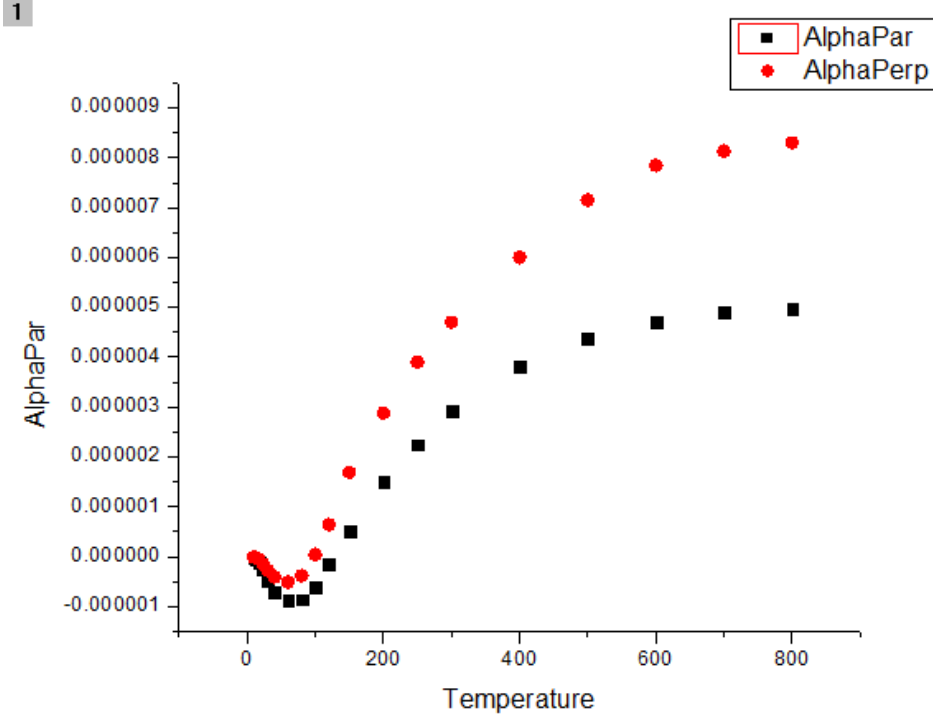


Figure 3.9: Thermal expansion coefficients along parallel (black squares) and perpendicular (red circles) directions of the lattice axis.

Finally the lineshape of the Raman peak is :

$$I(w) \propto \frac{\Gamma(w)}{[w_0 + \Delta_0 + \Delta(w) - w]^2 + \Gamma^2(w)} \quad (3.6)$$

The tendency of the peak to deviate from the Lorentzian shape is the frequency dependence of its phonon self energy components, where the real part that accounts for the frequency shift, is also frequency dependent. The two phonon sum DOS was calculated by us, and it was shifted by -10cm^{-1} to compensate for isotopic effects of the constituent materials. Whereas the two phonon difference DOS was taken to be equal $\rho^-(w) \approx 0.25\text{states/cm}^{-1}$, this is because its nearly flat around the frequency of the E_2^{high} . We can see that the E_2^{high} mode frequency lies on a ridge like shape of the two-phonon sum DOS from the following figure:

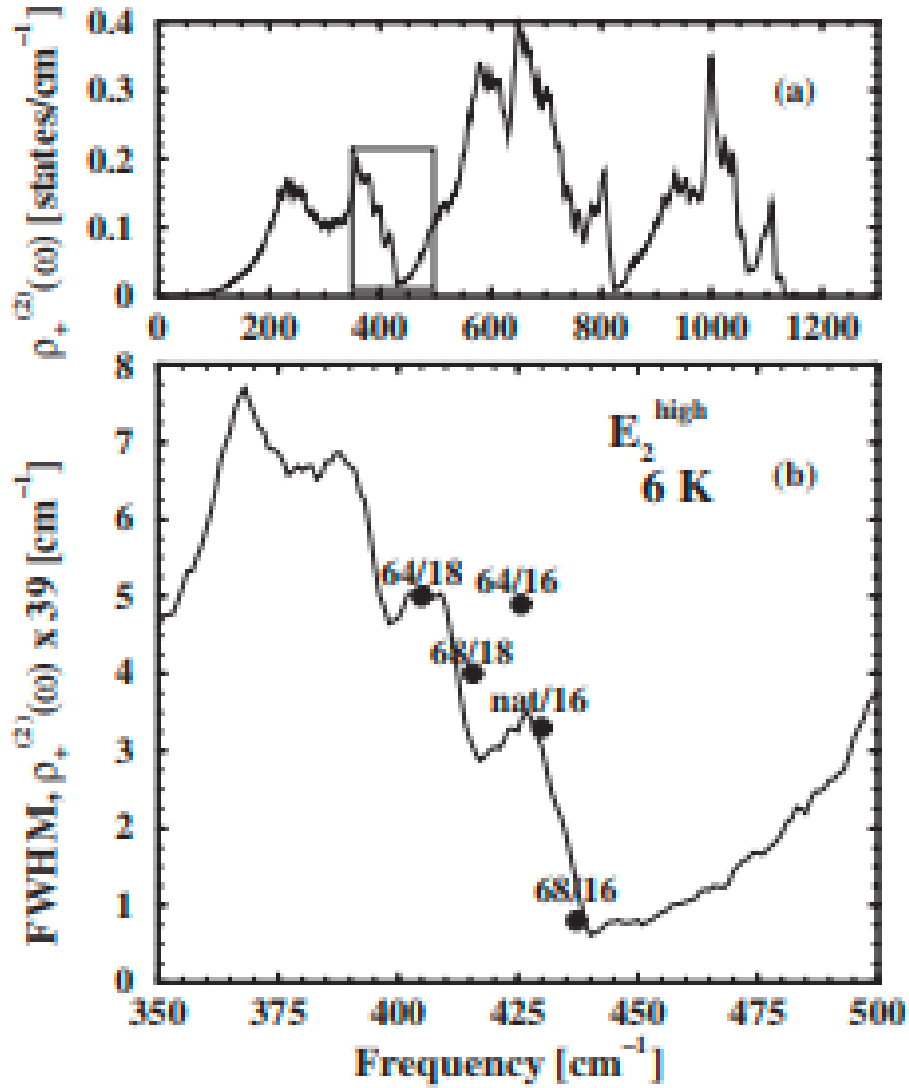


Figure 3.10: Two phonon sum DOS

The frequency term in the phonon occupation number in the imaginary and real part of phonon self energy, stands for the phonon decay channels. From the phonon dispersion relation of ZnO, we can suggest a decay channel into a sum of two acoustic phonons of frequencies 190cm^{-1} and 250cm^{-1} , and into a difference between 550cm^{-1} and 110cm^{-1} . Now we can calculate the lineshape of the $E_{2_{high}}$ mode, taking into account the two adjustable parameters $|V_3^+|^2$ and $|V_3^-|^2$. The fit between the theoretical and experimental work is shown in the following graph: Very good agreement is obtained between the developed model and the experimental results. The above figure shows the asymmetric shape of the E_2^{high} mode toward lower frequencies. The origin of this asymmetry is the

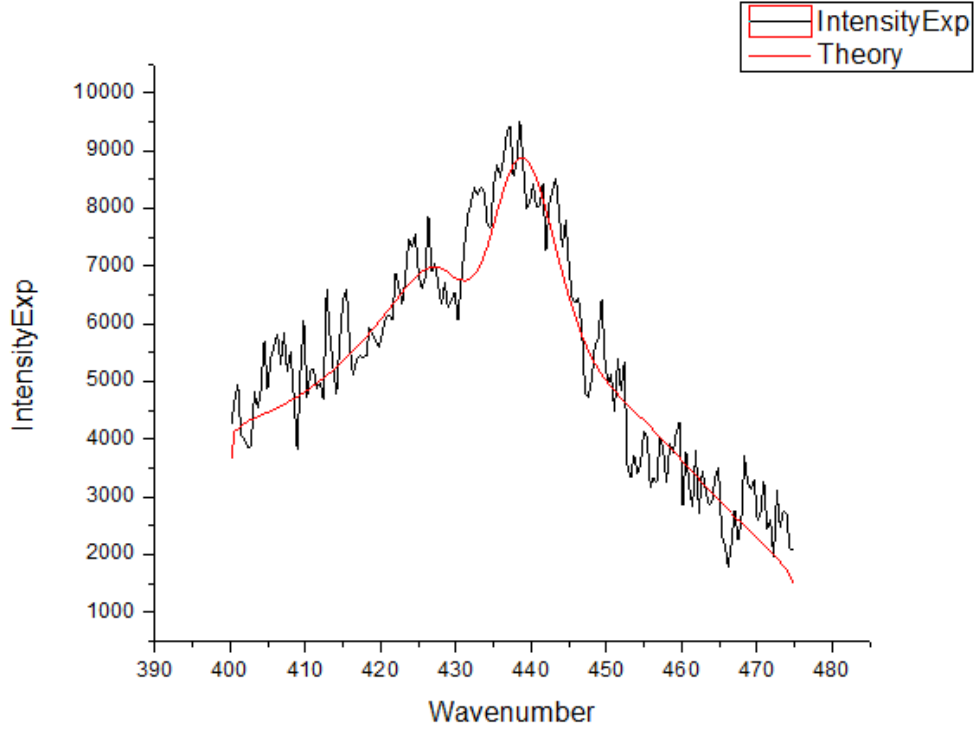


Figure 3.11: The spectrum of E_2^{high} mode of ZnO at room temperature. The noisy black line represents our experimental results, where the solid red line is calculated using equation 3.6.

strong frequency dependence of the imaginary part of the phonon self energy , which is plotted in Fig 3.10 (dashed-dotted line) against the left axis over the frequency region where the E_2^{high} mode occurs.

3.5 Temperature dependence of the E_2^{high} mode

After conducting the above results at room temperature. Now, we track phonon's mode response with respect to temperature , in order to collect more information about the mechanisms governing phonons interactions. For this purpose, a heater is connected to hold the sample, so that heat is transferred directly to the surface of our thin sample. Furthermore, a cooling process has been done, and the data of the Raman spectra were collected. The Raman spectra of the E_2^{high} mode in the temperature range 300-1000K in the heating and the cooling processes is as follows:

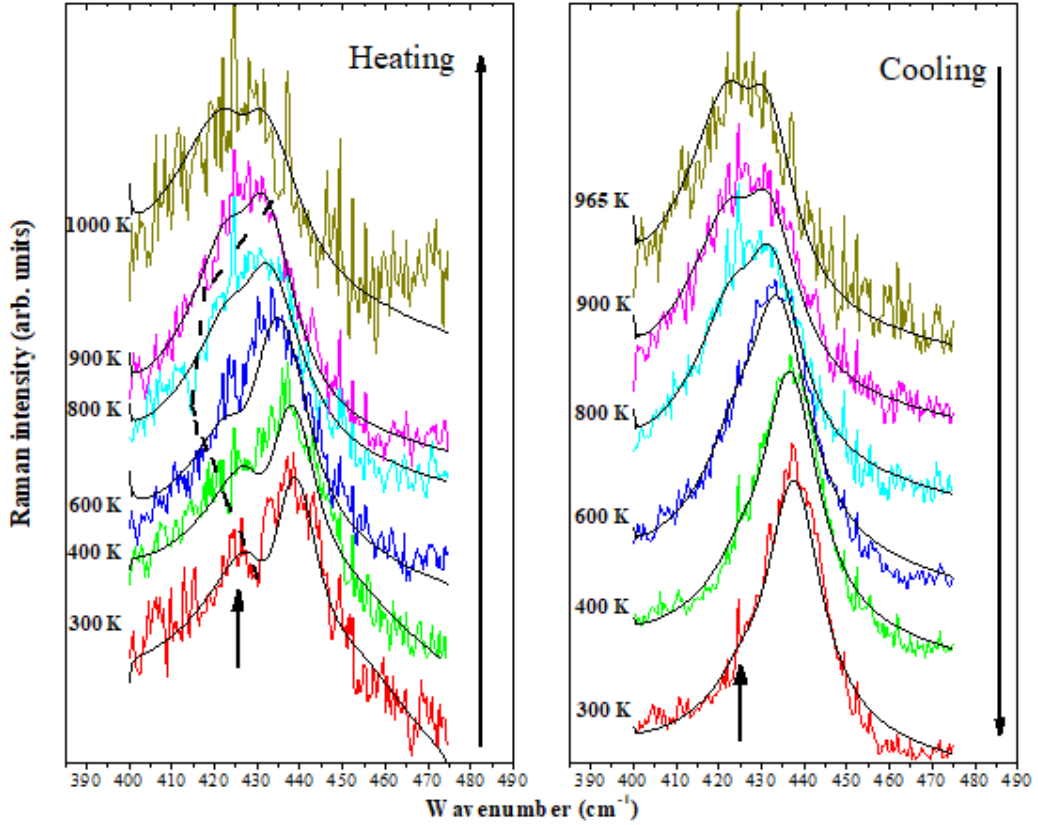


Figure 3.12: This figure shows the spectrum of E_2^{high} mode of ZnO at various temperatures. The left side shows the heating process, while the right side illustrates the cooling process. On both sides, the noisy lines with different colors represent our measurement of the Raman spectra of the E_2^{high} mode at different temperatures. The solid black lines are the fitted theoretical lines from the fitting intensity equation (3.6) concluded from the model mentioned above. The dashed line follows the position of the defect (dip-like shape) as temperature increases, also the arrow points at another doublet defect at the heating process, before its transformation to a singlet during the cooling process

The above figure is a rich medium of information concerning many phonon interaction mechanisms occurring at different temperatures. To kick off this discussion, we start by dividing the two figures to three stages. The first stage is in the heating process from temperature (300→800K). The second stage is combined between the heating and cooling processes, and it ranges in both of them from 800 to 1000K. The third stage is in the cooling process and it deals with the Raman lines below 800K. In a general overview of the above figure, we see in the heating process an increase in the intensity of the Raman lines of the E_2^{high} mode as temperature increases. Also, a change of the Raman-line position toward lower frequencies is observed and caused by the three phonon interaction processes done

by the sample in order to maintain thermal equilibrium (This was discussed in the literature review, with the equations governing the frequency change as a function of temperature). The asymmetry of this mode toward lower frequencies is also obvious at room temperature, and it decreases as temperature increases. The asymmetry was discussed in the previous section, when we insisted that anharmonic phonon interactions with the two phonon density of states, creates a distortion in the expected Lorentzian Raman line of the E_2^{high} mode, as shown from its shape. We can clearly see a dip-like shape in the Raman lines, where this dip is a defect found in the sample, and the cause of its existence in the Raman line is justified because it absorbs the incoming photons and it resonates with them. An arrow, points to a doublet, that illustrates another defect, and transforms into a singlet at the end of the cooling process.

Defects occur in the synthesis process and they interact with phonons, also they form their own states in the lattice. That's why a phonon lifetime is directly affected by the defect density. In this figure, its obvious that when temperature increases, the location of the defect changes (its location in terms of the wavenumber). In the first stage of the heating process (300-800K), the defect moves toward lower frequencies, this move in site, changes the interaction mechanism with phonons, therefore it manipulates the shape of the two phonon sum DOS. As we saw before, the line-shape of a Raman-line and its asymmetry is directly relevant to the position of the mode's frequency with respect to the two phonon sum DOS. The change of the two phonon sum DOS (caused by the change of the defect site), moves the E_2^{high} mode from the ridge like shape in the two sum phonon DOS, and therefore we see its shape changes as temperature increases, and becomes less asymmetric (The Raman line-width is directly proportional to the two phonon DOS).

In the second stage, which is combined between 800-1000K in the heating process, and from 965-800K in the cooling process, we observe that the defect site is not changing between a temperature in the heating and its value in the cooling. In other words, the defect is in the same position in 800K during heating and 800K during cooling. Furthermore, it is in the same position for 900K in both processes. Also, this is true for 1000K at heating and 965K in cooling. This is observed from the resemblance of the Raman lines of each temperature between the 2 processes. Where the Raman line at 800K in heating looks like the one at 800K in cooling, same thing applies for 900K and 1000K temperatures. From here we concluded that the process in this stage is reversible. Note here that the defect site is changing during heating from 800K-1000K, and among cooling from 965K-800K, which causes the change in the Raman line-shape under the same discussion of stage 1.

The turn point here is in the third stage (below 800K in the cooling process), when the defect site is not reversible as temperature decreases. In this stage, the defect disappears totally from the Raman-line. This disappearance may be caused

by the high temperatures attained by the sample. There exists a treatment process (known by physicists and chemists) known as annealing treatment that reduces the defect density in the sample. This disappearance changes the shape of the two phonon DOS more and more, and this is translated to the Raman line-shape of the E_2^{high} mode. It is observed that below 800K the line-shape becomes somehow symmetric with very little asymmetry toward lower frequencies. The E_2^{high} mode frequency is no longer on a ridge-like shape on the two phonon sum DOS, but it is now near a flat region of it.

To aid the discussion mentioned above, we follow the fitting parameters used to fit the FWHM (full width at half maximum) of each peak at different temperatures. The equation is mentioned above, but let me remind you of it :

$$\Gamma(w) = |V_3^+|^2(1 + n_1 + n_2)\rho^+(w) + |V_3^-|^2(n_2 - n_1)\rho^-(w) \quad (3.7)$$

Where $|V_3^+|^2$ and $|V_3^-|^2$ are the effective third order anharmonic constants of the phonon sums and differences, and ρ^+ and ρ^- are the two phonon DOS sums and differences respectively. For the fitting equations, we used frequencies $190cm^{-1}$ and $250cm^{-1}$ for n_1 and n_2 in the first term of the equation. For the difference scattering channel, frequencies of values $550cm^{-1}$ and $110cm^{-1}$ were applied to the phonon occupation number. Now, let us obtain the parameters $|V_3^+|^2$ and $|V_3^-|^2$:

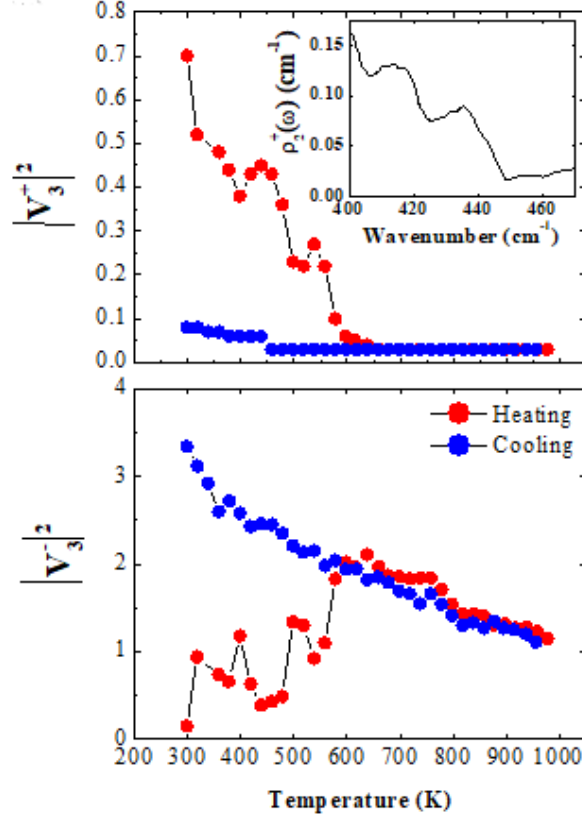


Figure 3.13: The first figure shows the strength of the third anharmonic coefficient of the phonon sum as a function of temperature during the heating and the cooling process. While in its inset, we see the graph of the two phonon sum DOS as function to the wavenumber. The second figure shows the $|V_3^-|^2$ as a function of temperature. In both figures, the red circles are associated to the heating process, while the blue circles demonstrates the cooling process.

Also we divide these graphs into 3 stages. In the first stage (Temperature range 300→600-700K) in the heating process, we see a wide value change of $|V_3^+|^2$ (red circles), which is concluded by the change of the shape of the two phonon sum DOS caused by the defect site change in this temperature range. Its obvious that its value starts to decrease here, so that the E_2^{high} mode frequency is moving from the ridge-like shape in the two phonon sum DOS and therefore its impact becomes less on it. On the other hand, the change of the $|V_3^-|^2$ on this range is averaged to constant (The E_2^{high} mode frequency is in a flat region in the two phonon difference DOS). The tremendous work here, is that we are

able to construct the shape of the two phonon sum DOS from the graph of the effective third-order anharmonic constants for decay into phonon sums versus temperature (See the first graph in figure (3.13) and its inset) . This is because the $|V_3^+|^2$ demonstrates the interactions with the two phonon sum DOS.

The second stage shows constant values of $|V_3^+|^2$ coefficient till the end of the heating process. That is, the E_2^{high} mode now is not influenced with the two phonon sum DOS, and temperature is affecting its Raman line-width position. Also this is observed in the cooling process till 600-700K, which indicates here that the process is reversible. This is a previous conclusion from the previous figure. Also, same justification and same behaviour applies to $|V_3^-|^2$ coefficient, where it shows a reversible process in this stage.

The turn point here is in the third stage of the cooling process (temperature below 600K). We saw before the disappearance of the defect from the Raman lines in this stage, so that the two phonon sum DOS has changed and the E_2^{high} frequency is no longer on a ridge-like shape on it. This can be concluded from the constant value of the $|V_3^+|^2$ in this region, and the rise of the $|V_3^-|^2$ values at the same time.

3.6 Temperature dependence of the A_1 mode at $333cm^{-1}$ and $E_1(LO)$ mode at $582cm^{-1}$

An interesting behaviour was found from the temperature dependence of the width for the two A_1 and $E_1(LO)$ polarized modes. The first mode is an axial mode, and the second mode is in-plane mode due to the motion in the unit cell. Where upon fitting our experimental data to the theory, we used the following model. which is a simpler model rather than the one used above:

$$\Gamma(T) = \Gamma_0 + A[1 + n(w_1, T) + n(w_2, T)] \quad (3.8)$$

Where Γ_0 is the intrinsic FWHM due to scattering by defects and it is temperature independent, and the second term is the three phonon interaction term and it is temperature dependent, where A is the parameter showing the strength of this interaction. From the dispersion relations, we find the decaying channels of the A_1 mode to be for w_1 between $92-152cm^{-1}$, and w_2 between $182-242cm^{-1}$. For E_1 mode, the decay channel for the phonons are $w_1 = 88 - 105cm^{-1}$, and $w_2 = 475 - 492cm^{-1}$. Their line-width with respect to temperature shows:

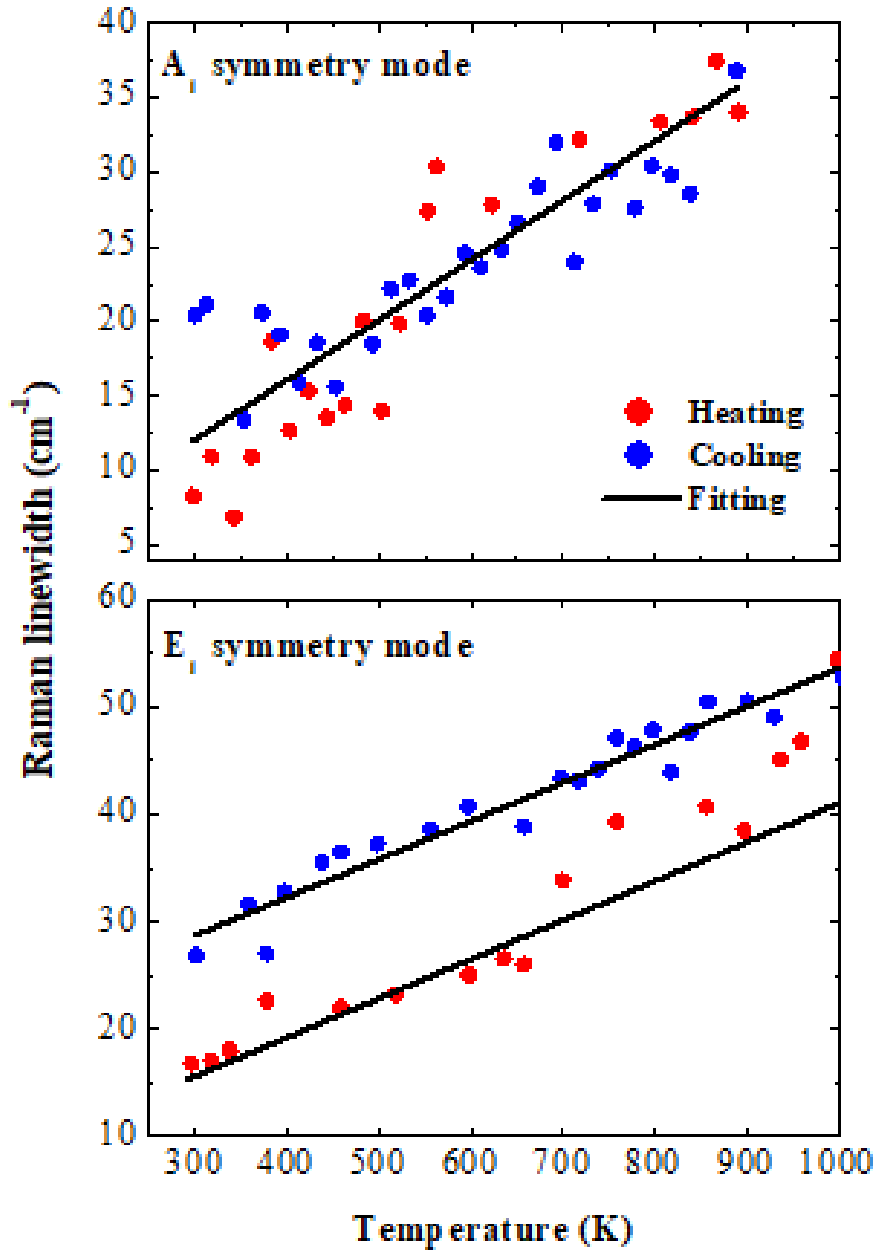


Figure 3.14: The first figure shows the temperature dependence of the line-width of the A_1 symmetry mode at 333cm^{-1} , while the second figure shows the temperature dependence of the $E_1(\text{LO})$ mode at 586cm^{-1} . For both graphs, the red circles are the values of the width during the heating process, while the blue circles are the values of the width during the cooling process. The black solid line represents the fitted line from the theoretical equation (3.8)

This figure shows the temperature dependence of the width of A_1 and E_1

modes in the heating process (red circles), and the cooling process (blue circles). The black solid straight line is the theoretical equation used to fit our results. We see that as a temperature increases, the Raman line width of both modes increases also, which is expected from decays through three phonon process interactions, and its strength is represented by the parameter A in the equation. Also it is observed that the width decreases in the cooling process. A deep look into the first part of this figure, we notice a reversible behaviour between the increase and decrease process of the width, which leaves us to conclude that the defect is not interacting with this mode.

While for E_1 mode, the increase of the width shows a change in behaviour at temperature 700K, when the red circles do not abide the theoretical fitting line. This is understood from the interaction of this phonon mode with defects that are changing their site here. At the same time, Γ_0 in the equation has changed from 0 to 18 (reminding you that this parameter accounts for width change upon interactions with defects only and it is temperature independent). At the beginning of the heating process from 300→700K, the scattering was due to cubic anharmonic phonon interactions, but after 700K, a change in the increasing behaviour occurred due to the change of the defect site. Also we observe that the cooling process maintains the same behaviour attained by the last points of the heating process, so that we conclude that now the defect is not changing its position upon temperature changes.

3.7 Conclusion

This work is dedicated to understand the role of anharmonic processes on the phonon interactions, and to study the effect of defects on the anharmonicity of optical phonons in wurtzite zinc oxide (ZnO) nanoparticles. Also we explained the source of the asymmetrical shape of Raman lines of the E_2^{high} mode, alongside the change of the phonon lifetimes with temperature change. We found that at constant temperature, when a phonon mode is near a ridge-like shape of the 2 phonon DOS, an expected asymmetrical peak is to be observed as in the intensity equation, the denominator is frequency dependent, resulting for the frequency dependence from components of the phonon self energy.

When temperature increases, it is crucial to track the defect's site because it is of major importance in terms of the interaction with phonons. Any change of the defect site means a change in the shape of the two phonon DOS, and this is translated to the Raman line-shape of the targeted mode. Also, we deduced the graph of the 2 phonon DOS to have the same shape of the effective third order harmonic constant decay of phonon sums with respect to temperature, because these interactions are manifest of phonon interactions with the two phonon sum DOS, therefore the graph of the strength of these interactions with respect to

temperature is the mirror of the two phonon density of state. This is the first time that one can expect the shape of the 2 phonon DOS from the temperature dependence of $|V_3^+|^2$. We saw a total irreversible process between the heating and the cooling process of the Line-shape of the E_2^{high} mode, except for the second stage of the two processes (800K to 1000K), where the defect is localized at these temperatures, therefore we observed a reversible process at these temperatures, and the behaviour of the $|V_3^+|^2$ and $|V_3^-|^2$ at these values of temperature aided this conclusion.

One major conclusion from this thesis is that the defect location didn't affect the Raman line-width of the A_1 symmetry mode which is an axial mode, unlike its effect on the E_1 mode that is an in-plane mode. For this mode, we observed a change in the behaviour of the increasing line-width values after 600k temperature, and the behaviour of the cooling process matched the last behaviour of the heating process, and this was justified by the change of the Γ_0 term in the fitting equation, which is the term responsible for the scattering due to defects.

Appendix A

Abbreviations

IR	Infrared
INS	Inelastic Neutron Scattering
PMT	Photomultiplier
CCD	Charged Coupled Device Detector
FWHM	Full Width at Half Maximum
DOS	Density of State

Bibliography

- [1] M. Monge, M. L. Kahn, A. Maisonnat, and B. Chaudret, “Room-temperature organometallic synthesis of soluble and crystalline zno nanoparticles of controlled size and shape,” *Angewandte Chemie International Edition*, vol. 42, no. 43, pp. 5321–5324, 2003.
- [2] T. Andelman, Y. Gong, M. Polking, M. Yin, I. Kuskovsky, G. Neumark, and S. O’Brien, “Morphological control and photoluminescence of zinc oxide nanocrystals,” *The Journal of Physical Chemistry B*, vol. 109, no. 30, pp. 14314–14318, 2005.
- [3] O. M. V. P. S.K.N. Ayudhya, P. Tonto and P. Prasertthdam *Crystal Growth and Design*, vol. 6, p. 2446, 2006.
- [4] J. Calleja and M. Cardona, “Resonant raman scattering in zno,” *Physical Review B*, vol. 16, no. 8, p. 3753, 1977.
- [5] M. K. Toth, *Magnetic propterties of Sr 2 YRu 1-x Ir x O 6 compounds*. PhD thesis, San Diego State University, 2013.
- [6] R. Cowley, “Anharmonic crystals,” *Reports on Progress in Physics*, vol. 31, no. 1, p. 123, 1968.
- [7] R. P. Feynman, “There’s plenty of room at the bottom,” *California Institute of Technology, Engineering and Science magazine*, 1960.
- [8] N. Taniguchi, “On the basic concept of nanotechnology,” *Proceeding of the ICPE*, 1974.
- [9] D. Reynolds, D. C. Look, B. Jogai, J. Hoelscher, R. Sherriff, M. Harris, and M. Callahan, “Time-resolved photoluminescence lifetime measurements of the γ 5 and γ 6 free excitons in zno,” *Journal of Applied Physics*, vol. 88, no. 4, pp. 2152–2153, 2000.
- [10] A. Lansdown and A. Taylor, “Zinc and titanium oxides: promising uv-absorbers but what influence do they have on the intact skin?,” *International journal of cosmetic science*, vol. 19, no. 4, pp. 167–172, 1997.

- [11] M. Vaseem, A. Umar, and Y.-B. Hahn, “Zno nanoparticles: growth, properties, and applications,” *Metal oxide nanostructures and their applications*, vol. 5, no. 1, 2010.
- [12] R.-Q. Song, A.-W. Xu, B. Deng, Q. Li, and G.-Y. Chen, “From layered basic zinc acetate nanobelts to hierarchical zinc oxide nanostructures and porous zinc oxide nanobelts,” *Advanced Functional Materials*, vol. 17, no. 2, pp. 296–306, 2007.
- [13] P. X. Gao, Y. Ding, W. Mai, W. L. Hughes, C. Lao, and Z. L. Wang, “Conversion of zinc oxide nanobelts into superlattice-structured nanohelices,” *Science*, vol. 309, no. 5741, pp. 1700–1704, 2005.
- [14] C. L. Carnes and K. J. Klabunde, “Synthesis, isolation, and chemical reactivity studies of nanocrystalline zinc oxide,” *Langmuir*, vol. 16, no. 8, pp. 3764–3772, 2000.
- [15] M. L. Kahn, M. Monge, V. Colliere, F. Senocq, A. Maisonnat, and B. Chaudret, “Size-and shape-control of crystalline zinc oxide nanoparticles: a new organometallic synthetic method,” *Advanced Functional Materials*, vol. 15, no. 3, pp. 458–468, 2005.
- [16] Y. Yang, H. Chen, B. Zhao, and X. Bao, “Size control of zno nanoparticles via thermal decomposition of zinc acetate coated on organic additives,” *Journal of crystal growth*, vol. 263, no. 1-4, pp. 447–453, 2004.
- [17] Y. Zhang, K. Yu, D. Jiang, Z. Zhu, H. Geng, and L. Luo, “Zinc oxide nanorod and nanowire for humidity sensor,” *Applied Surface Science*, vol. 242, no. 1-2, pp. 212–217, 2005.
- [18] T. Kawano and H. Imai, “Fabrication of zno nanoparticles with various aspect ratios through acidic and basic routes,” *Crystal growth & design*, vol. 6, no. 4, pp. 1054–1056, 2006.
- [19] E. Mocchegiani, J. Romeo, M. Malavolta, L. Costarelli, R. Giacconi, L.-E. Diaz, and A. Marcos, “Zinc: dietary intake and impact of supplementation on immune function in elderly,” *Age*, vol. 35, no. 3, pp. 839–860, 2013.
- [20] J. Jiang, J. Pi, and J. Cai, “The advancing of zinc oxide nanoparticles for biomedical applications,” *Bioinorganic chemistry and applications*, vol. 2018, 2018.
- [21] H.-M. Xiong, Y. Xu, Q.-G. Ren, and Y.-Y. Xia, “Stable aqueous zno@polymer core-shell nanoparticles with tunable photoluminescence and their application in cell imaging,” *Journal of the American Chemical Society*, vol. 130, no. 24, pp. 7522–7523, 2008.

- [22] P. Graves and D. Gardiner, “Practical raman spectroscopy,” *Springer*, 1989.
- [23] A. P. Mamede, D. Gonçalves, M. P. M. Marques, and L. A. Batista de Carvalho, “Burned bones tell their own stories: A review of methodological approaches to assess heat-induced diagenesis,” *Applied Spectroscopy Reviews*, vol. 53, no. 8, pp. 603–635, 2018.
- [24] E. Condon, “The franck-condon principle and related topics,” *American journal of physics*, vol. 15, no. 5, pp. 365–374, 1947.
- [25] D. W. Hahn, “Raman scattering theory,” *Department of Mechanical and Aerospace Engineering, University of Florida*, 2007.
- [26] G. Gouadec and P. Colomban, “Raman spectroscopy of nanomaterials: How spectra relate to disorder, particle size and mechanical properties,” *Progress in crystal growth and characterization of materials*, vol. 53, no. 1, pp. 1–56, 2007.
- [27] D. A. Long and D. Long, *Raman spectroscopy*, vol. 276. McGraw-Hill New York, 1977.
- [28] A. C. De Luca, K. Dholakia, and M. Mazilu, “Modulated raman spectroscopy for enhanced cancer diagnosis at the cellular level,” *Sensors*, vol. 15, no. 6, pp. 13680–13704, 2015.
- [29] H. Malekpour and A. A. Balandin, “Raman optothermal technique for measuring thermal conductivity of graphene and related materials,” *arXiv preprint arXiv:1710.09749*, 2017.
- [30] D. C. Look, “Recent advances in zno materials and devices,” *Materials Science and Engineering: B*, vol. 80, no. 1-3, pp. 383–387, 2001.
- [31] B. Lee, K. Kim, M. Stroschio, and M. Dutta, “Optical-phonon confinement and scattering in wurtzite heterostructures,” *Physical review B*, vol. 58, no. 8, p. 4860, 1998.
- [32] T. C. Damen, S. Porto, and B. Tell, “Raman effect in zinc oxide,” *Physical Review*, vol. 142, no. 2, p. 570, 1966.
- [33] C. Arguello, D. L. Rousseau, and S. d. S. Porto, “First-order raman effect in wurtzite-type crystals,” *Physical Review*, vol. 181, no. 3, p. 1351, 1969.
- [34] R. Cuscó, E. Alarcón-Lladó, J. Ibanez, L. Artús, J. Jiménez, B. Wang, and M. J. Callahan, “Temperature dependence of raman scattering in zno,” *Physical Review B*, vol. 75, no. 16, p. 165202, 2007.

- [35] H. Siegle, G. Kaczmarczyk, L. Filippidis, A. Litvinchuk, A. Hoffmann, and C. Thomsen, “Zone-boundary phonons in hexagonal and cubic gan,” *Physical Review B*, vol. 55, no. 11, p. 7000, 1997.
- [36] J. Serrano, A. Romero, F. Manjon, R. Lauck, M. Cardona, and A. Rubio, “Pressure dependence of the lattice dynamics of zno: An ab initio approach,” *Physical Review B*, vol. 69, no. 9, p. 094306, 2004.
- [37] G. P. Srivastava, *The physics of phonons*. Routledge, 2019.
- [38] R. Cowley, “Raman scattering from crystals of the diamond structure,” *Journal de Physique*, vol. 26, no. 11, pp. 659–667, 1965.
- [39] J. Menéndez and M. Cardona, “Temperature dependence of the first-order raman scattering by phonons in si, ge, and α -s n: Anharmonic effects,” *Physical Review B*, vol. 29, no. 4, p. 2051, 1984.
- [40] T. Feng and X. Ruan, “Quantum mechanical prediction of four-phonon scattering rates and reduced thermal conductivity of solids,” *Physical Review B*, vol. 93, no. 4, p. 045202, 2016.
- [41] N. W. Ashcroft, N. D. Mermin, *et al.*, “Solid state physics [by] neil w. ashcroft [and] n. david mermin.,” 1976.
- [42] P. Klemens, “Anharmonic decay of optical phonons,” *Physical Review*, vol. 148, no. 2, p. 845, 1966.
- [43] J. Parker Jr, D. Feldman, and M. Ashkin, “Raman scattering by silicon and germanium,” *Physical Review*, vol. 155, no. 3, p. 712, 1967.
- [44] H. Richter, Z. Wang, and L. Ley, “The one phonon raman spectrum in microcrystalline silicon,” *Solid State Communications*, vol. 39, no. 5, pp. 625–629, 1981.
- [45] G. K. Morhange, J.F and M. Balkanski *Solid State Communications*, vol. 31, p. 805, 1979.
- [46] M. I. S. O. F. P. TSU, R. *Solid State Communications*, vol. 36, p. 817, 1980.
- [47] Z. Iqbal, A. Webb, and S. Vepřek, “Polycrystalline silicon films deposited in a glow discharge at temperatures below 250 c,” *Applied Physics Letters*, vol. 36, no. 2, pp. 163–165, 1980.
- [48] I. Campbell and P. M. Fauchet, “The effects of microcrystal size and shape on the one phonon raman spectra of crystalline semiconductors,” *Solid State Communications*, vol. 58, no. 10, pp. 739–741, 1986.

- [49] Z. Iqbal and S. Veprek, “Raman scattering from hydrogenated microcrystalline and amorphous silicon,” *Journal of Physics C: Solid State Physics*, vol. 15, no. 2, p. 377, 1982.
- [50] F. P. K.K. Tiong, P.M. Amirharaj and D. Aspens *Applied Physics Letters*, vol. 44, p. 122, 1984.
- [51] D. Murphy and S. Brueck *Mat. Res. Soc. Symp. Proc.*, vol. 17, p. 81, 1983.
- [52] K. Roodenko, I. Goldthorpe, P. McIntyre, and Y. Chabal, “Modified phonon confinement model for raman spectroscopy of nanostructured materials,” *Physical Review B*, vol. 82, no. 11, p. 115210, 2010.
- [53] H. Ibach, “Thermal expansion of silicon and zinc oxide (i),” *physica status solidi (b)*, vol. 31, no. 2, pp. 625–634, 1969.

